INVESTIGATION OF THE IRON-OXIDE MINERALIZATION AT THE IRON RANGE, SOUTHEASTERN BC

by

Michael Galicki
B.Sc. (Geology), Laurentian University, 2008

THESIS SUBMITTED IN PARTIAL FULFILLMENT OF
THE REQUIREMENTS FOR THE DEGREE OF

MASTER OF SCIENCE

In the
Department of Earth Sciences
Faculty of Science

© Michael Galicki 2011

Simon Fraser University

Fall 2011

APPROVAL

Name: **Michael Galicki**

Degree: **Master of Science**

Title of Thesis: **INVESTIGATION OF THE IRON-OXIDE MINERALIZATION AT THE IRON RANGE, SOUTHEASTERN BC**

Examining Committee:

         Chair: **Dr. Dirk Kirste**
                        Assistant Professor, Department of Earth Sciences

_____

Dr. Dan Marshall
Senior Supervisor
Professor, Department of Earth Sciences

_____

Dr. Derek Thorkelson
Supervisor
Professor, Department of Earth Sciences

_____

Dr. Ken Hickey
External Examiner
Assistant Professor, UBC

Date Defended/Approved: <u>August 26, 2011</u>
.

Declaration of
Partial Copyright Licence

The author, whose copyright is declared on the title page of this work, has granted to Simon Fraser University the right to lend this thesis, project or extended essay to users of the Simon Fraser University Library, and to make partial or single copies only for such users or in response to a request from the library of any other university, or other educational institution, on its own behalf or for one of its users.

The author has further granted permission to Simon Fraser University to keep or make a digital copy for use in its circulating collection (currently available to the public at the "Institutional Repository" link of the SFU Library website <www.lib.sfu.ca> at: <http://ir.lib.sfu.ca/handle/1892/112>) and, without changing the content, to translate the thesis/project or extended essays, if technically possible, to any medium or format for the purpose of preservation of the digital work.

The author has further agreed that permission for multiple copying of this work for scholarly purposes may be granted by either the author or the Dean of Graduate Studies.

It is understood that copying or publication of this work for financial gain shall not be allowed without the author's written permission.

Permission for public performance, or limited permission for private scholarly use, of any multimedia materials forming part of this work, may have been granted by the author. This information may be found on the separately catalogued multimedia material and in the signed Partial Copyright Licence.

While licensing SFU to permit the above uses, the author retains copyright in the thesis, project or extended essays, including the right to change the work for subsequent purposes, including editing and publishing the work in whole or in part, and licensing other parties, as the author may desire.

The original Partial Copyright Licence attesting to these terms, and signed by this author, may be found in the original bound copy of this work, retained in the Simon Fraser University Archive.

Simon Fraser University Library
Burnaby, BC, Canada

ABSTRACT

The Iron Range iron oxide occurrence in south eastern British Columbia consists of massive lenses and veins of hematite and martite with lesser magnetite that pinch and swell along the Iron Range fault zone. It is hosted within the Proterozoic Aldridge Formation and Moyie Sills and forms a central massive iron-oxide corridor flanked by albite-quartz iron-oxide breccia. The most common alteration assemblage is albite-chlorite-hematite-magnetite +/- silica, which is locally overprinted by later iron-oxide, silica, sericite or carbonate alteration.

Oxygen isotope analyses in conjunction with fluid inclusions indicate precipitation temperatures for the mineralized zones in the range 340 to 400 °C and 1750 to 4500 bars. The Iron Range iron oxide mineralized rock shares many characteristics of major IOCG deposits and alkali porphyry systems, however the exposed rocks lack economic Cu (+-Au)-concentration. Magnetite trace element chemistry is consistent with IOCG and porphyry mineralization worldwide and recent drilling intersected minor sulphide (chalcopyrite and pyrite) and gold mineralization at 200 m and 20 m depths, respectively. Paleomagnetic studies in conjunction with Ar-Ar dating of regional (magnetite-rich) intrusions support a Cretaceous hydrothermal event responsible for the alteration and mineralization at the Iron Range.

Keywords: Iron Range; hematite, magnetite, breccia; Bayonne Magmatic Suite; fluid inclusion, oxygen isotope; IOCG; Cretaceous

ACKNOWLEDGEMENTS

TABLE OF CONTENTS

LIST OF FIGURES

LIST OF TABLES

1: INTRODUCTION

1.1 Goals of this thesis

The Iron Range iron-oxide occurrence genesis is poorly understood and hasn't been adequately studied or described in the scientific literature. The goal of this thesis is to establish the age of the iron-oxide occurrence, relate this age to new and existing literature ages of possible heat and fluid sources, and to provide a model for the genesis of these iron-oxide occurrences.

In addition, this thesis will attempt to relate the various alterations to the oxide, sulphide and gold mineralized rocks. Furthermore, the Iron Range iron-oxide occurrence will be compared to iron-oxide rich deposit types and the question whether the Iron Range can be classified as a prospect for a deposit will be addressed at the end of this thesis.

1.2 Location, access and exposure

The Iron Range study area is located in southeastern British Columbia approximately 15 km north-east of Creston, BC (Figure 1). It is a mountainous ridge paralleling the Goat River and it can be accessed on Forestry Service Roads starting in Kitchener, BC at Highway 3. The centre of the study area can be found at UTM 6832001N / 633500E (NAD 83, Zone 11) and straddles B.C. Map sheets 82F018 and 82F019.

The outcrop exposure in the study area is very poor and the majority of the iron-oxide occurrences are located 50-100 year old trenches. The trenches are mostly filled with float and overgrown and there is limited outcrop exposure within the trenches. Drill-core from approximately 30 drill-holes has been used to augment the limited outcrop.
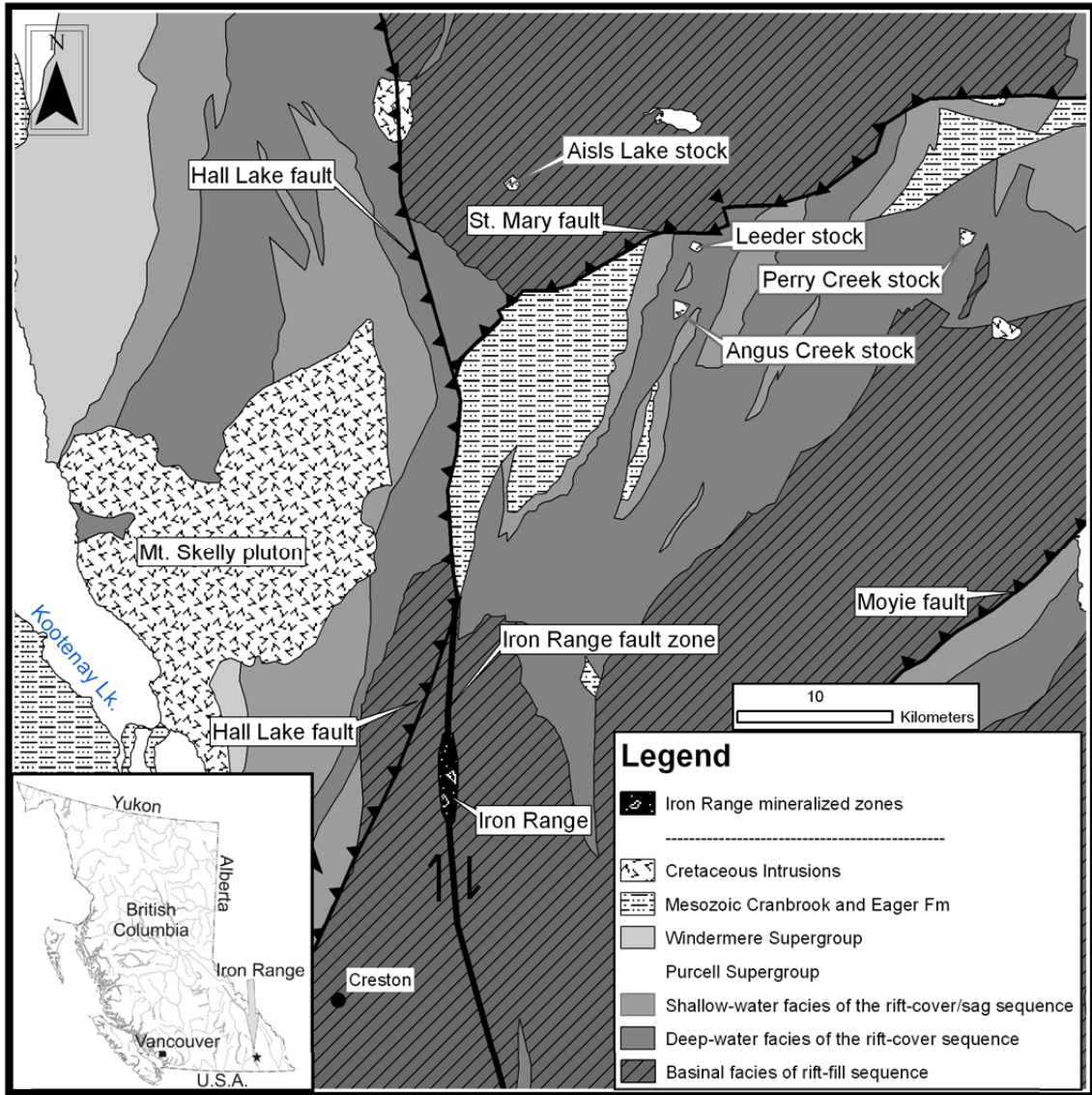
Figure 1: Location and regional geology map (compiled from Massey et al. (2005))

1.3 Historic Information

The Iron Range iron-oxide mineralization was discovered at the end of the 19th century and the first claims were staked in 1897. Several small abandoned shafts and adits date back to the beginning of the last century and are evidence of the first work conducted at the Iron Range. The Consolidated Mining and Smelting Company of Canada Ltd. and Canadian Pacific Railroad (CPR) acquired the claims for the northern part of the Iron Range in 1939. An iron-resources evaluation was carried out by CM&S (later Cominco Ltd., then Teck Cominco Ltd, and subsequently Teck Ltd.). Their evaluation efforts led to a major trenching program in 1957, which exposed most of the Iron Range structure and mineralization that can be seen today (Ryley, 2009).

Previous work in the Belt-Purcell basin led to the discovery of marker-horizons within Belt-Purcell strata, which can be used to correlate units of similar age across the whole basin (Legun, 1996). The Iron Range is stratigraphically near the Sullivan horizon, which is the stratigraphic level that hosted most of the mineralization at the Sullivan Mine in Kimberley, BC. Comino Ltd. included the Iron Range into their Sullivan search program in the 1980's. Cominco-CPR held the claims for the northern Iron Range claims until they reverted in 1999. Eagle Plains Resources Ltd. re-staked most of the historic claims together with adjacent claims in 1999. In 2000, Eagle Plains Resources began investigation of the Iron Range for SEDEX- and IOCG-potential. Their exploration program led to a major drilling program in 2008 consisting of 20 holes totalling 1684 meters.

1.4 Regional Geology

The Iron Range lies within the Belt-Purcell basin, which is a Proterozoic sedimentary basin. The sedimentary stratigraphy of the Belt-Purcell in Canada is the Purcell Supergroup and it represents the infilling of a (failed) intracontinental Mesoproterozoic rift system (Sears and Price, 1978; and McMechan, 1981; Chandler, 2000). The Belt-Purcell succession in the Canadian Cordillera (Purcell Supergroup) can be divided into 3 main groups (Lydon, 2007), which in ascending chronology are (1) basinal facies of rift-fill sequence (e.g., Aldridge Formation); (2) shallow-water platformal and fan-delta facies (e.g., Fort Steele Formation); and (3) shallow- and deep-water, mud flat, fluvial, lagoonal, alluvial, and playa facies of rift-cover or rift-sag sequence (Creston Formation, Kitchener Formation, Van Creek Formation, Nicol Creek Formation, Sheppard Formation, Gateway Formation, Phillips Formation and Roosville Formation).

The Iron Range consists of rocks of the basinal facies of rift-fill sequence, which is comprised of the Moyie sills and the Aldridge Formation. The Aldridge Formation is a sequence of quartzofeldspathic wacke. In the Purcell Mountains the Aldridge Formation is divided into the Lower, Middle and Upper Aldridge Formation. The Lower Aldridge Formation is at least 500 m thick with laminated fine-grained quartzites to argillites interlayered with turbiditesequences consisting of silt- to sandstone, arenite and wacke that have been intruded by the gabbroic Moyie sills. The thickest part of the Aldridge Formation is the 2000 - 3000 m thick Middle Aldridge Formation, which is composed of medium- to coarse-grained quartz-rich turbidites. The Upper Aldridge Formation is characterized by the

absence of turbidites and is composed of 400 - 700 m of siltstone, argillite and minor fine-grained quartzite. The Moyie sills range in composition from dominantly gabbro to diorite and consist of hornblende and plagioclase with minor quartz, chlorite and epidote. U-Pb zircon dates range from 1433±10 Ma to 1445±11 Ma (Lydon, 2000) and 1467±3 Ma (Anderson and Goodfellow, 1995). The Moyie sills and the Aldridge Formation together form a basal sediment-sill complex for the Belt-Purcell basin rift (Höy, 1993).

Within the Belt-Purcell basin, the Iron Range lies on the west flank of the Purcell Anticlinorium, which is a north-plunging antiform deformed by two folding events positioned between the Kootenay arc to the west and the Rocky Mountain thrust and fold belt to the east (Pope, 1990). The Purcell Anticlinorium is cored by the Aldridge Formation and is made up of a series of north-plunging anticlines, divided by major NE-trending thrust-folds, including the Moyie, Saint Mary, Hall Lake and Mount Forster-Purcell faults.

1.5 Magmatic and Metamorphic History of the Belt-Purcell Basin

1.5.1 Magmatic History

Magmatic activity in the Purcell basin is mainly constrained to the Mesoproterozoic, Early Paleozoic and Cretaceous. Mesoproterozoic magmatic activity is represented by the Moyie sills and Nicol Creek volcanics. The Hell Roaring Creek stock, a pegmatite body west of Kimberley along the St. Mary's Fault, has two unpublished U-Pb zircon ages of 1340 and 1360 Ma and is

associated with regional metamorphism during the East Kootenay Orogeny (Lydon, 2000).

Early Paleozoic magmatism is characterized by alkaline diatremes and carbonatites, which are relatively rare in the Belt-Purcell basin. Most diatremes and carbonatites are confined to the Rocky Mountain Alkaline Belt and are Permian in age (Walker, 1998). However, there are carbonatite intrusions in the Goat River area proximal to the Iron Range, which are interpreted to be Pennsylvanian in age (Walker, 1998). Outcropping carbonatite intrusions at the Iron Range that are similar to the carbonatite intrusions in the Goat River area yield Pennsylvanian phlogopite Ar-Ar ages (this thesis, Chapter 6.1). The Rocky Mountain Alkaline Belt is located approximately 200 km northeast of the Iron Range, west of Invermere, BC. The slightly older carbonatite in the Goat River area and at the Iron Range might suggest a smaller second alkaline belt in the Belt-Purcell basin.

Whereas the magmatic activity in the Mesoproterozoic was characterized by tholeiitic and andesitic basaltic flows and gabbros, magmatic activity in the Cretaceous involved predominantly felsic intrusions. Cretaceous plutons are very widespread in the Purcell basin and were generally emplaced along normal faults, which helped to date displacement along the major faults. However, not all plutons in the Purcell basin have been dated because of their small size. The Sanca Stock and the Mount Skelly Pluton represent Cretaceous magmatism proximal to the Iron Range. Both plutons are part of Cretaceous Bayonne Magmatic Suite and represent multiple intrusive phases. The Sanca Stock is a

biotite granodiorite and yielded an 80 Ma biotite K-Ar age, and the Mount Skelly

Pluton is a granodiorite and biotite monzogranite and yielded a 90 Ma biotite K-Ar

age (Logan, 2000).

One sample collected from the Mt. Skelly Pluton was dated by Ar-Ar

(biotite) at 89.7 +/- 0.9 Ma age (this thesis Chapter 6.1).

Of note are several (unnamed and not studied) iron-oxide occurrences to

the north-east of the Iron Range and south of the St. Mary Fault which commonly

occur in breccias and are proximal to Cretaceous Bayonne Magmatic Suite

intrusions. One intrusion, the Leeder Stock (Figure 1) hosts a magnetite-bearing

porphyry and displays at least two events of magnetite precipitation with

magnetite veins cross-cutting cumulate layers of euhedral magnetite. Iron-oxide

occurrences (breccias and veins) have been identified in the region of the Leeder

Stock during field work in 2008. As part of this thesis, this intrusion was dated at

104.8 +/- 1.1 Ma (Chapter 6.1).

1.5.2 Metamorphic History

Metamorphism in the Belt Purcell can be divided into 3 events: (1) the

East Kootenay Orogeny, (2) the Goat River Orogeny and (3) Mesozoic-Cenozoic

metamorphism.

The Mesoproterozoic East Kootenay Orogeny was a compressional event

which produced characteristic folds and cleavage and was accompanied by

granitic magmatism (Höy, 1993). It is believed that the East Kootenay Orogeny

marks the end of Purcell Supergroup sedimentation (~1300 Ma) and reflects

maximal burial depths (Lydon, 2000). Maximum metamorphic pressures recognized in the Purcell Supergroup have been calculated for silicate mineral assemblages at the Sullivan Mine (Kimberley) at 380 MPa (Lydon, 2000), which is equivalent to 14 km depth and consistent with Mesoproterozoic Purcell Supergroup thickness (Höy, 2000). Other evidence for the East Kootenay Orogeny is metamorphic titanite from a Moyie sill, which yielded at Pb-Pb date of 1329 ± 29 Ma (Schandl and Davis, 2000).

The second recognized metamorphic event in the Belt-Purcell is the Goat River Orogeny (800-900 Ma), which was an extensional tectonic event marking the onset of the Windermere Supergroup and was characterized by uplift and block-faulting (Höy, 1993). Evidence for low grade regional metamorphism is documented by reset K-Ar ages and paleomagnetic signatures (McMechan, 1982). Block-faulting in the Purcell basin is evident from conglomerate and breccia of the Windermere Supergroup along major faults in the north-west part of the basin and derived from the Purcell Supergroup. During this extensional event, blocks of Purcell strata were tilted or uplifted, shedding clastic sediments into adjacent basins. Locally the Windermere Supergroup ranges up to 9 km in thickness and occurs along a narrow north-east trend, suggesting that it was deposited in a deep, elongated block-faulted basin north of a high-standing source area (Höy, 1993).

The third metamorphic event was a Late Jurassic-Early Cretaceous episode of left-lateral transpression, followed by right-lateral transpression, during the Late Cretaceous-Paleocene, resulted in deformation and

metamorphism in the Mesozoic and Cenozoic. This episode of deformation and metamorphism was the result of oblique collision and accretion of the Quesnel terrane with the North American continental margin (Price, 2000). Most studies on metamorphism and deformation in the Belt-Purcell basin were concentrated around the Sullivan Deposit in Kimberley. Estimates for metamorphic conditions for Jurassic-Paleocene metamorphism in the central part of the Belt-Purcell basin (near the Sullivan Area) are 350±25°C and 450±50 MPa, indicating that most of the Aldridge Formation (which hosts the Sullivan Deposit) was buried to depths of 15-18km in Jurassic time due to tectonic loading (Lydon, 2000).

1.6 Local Geology and Structure

The Iron Range iron-oxide-mineralization is hosted in the Middle Aldridge Formation and is confined to the Iron Range Fault Zone (IRFZ) at the Iron Range Mountain (Marshall and Downie, 2002) (Figure 1). At the Iron Range the Middle Aldridge consists of predominantly weak to moderate rusty weathering, interbedded turbidites and dominantly medium bedded quartz wacke with intervals of thin bedded to laminated wacke. The deformed rock of the Middle Aldridge along the IRFZ is dominated by cataclasite. The IRFZ is a steeply west dipping (70-85 ˚) structure located 20 km west of the Goat River anticline, which is a gently NNW plunging fold related to regional foliation (strike 195 ˚, dip 60 ˚) (Brown and Stinson, 1995). Within the fault zone, shear fabric orientations in the Aldridge Formation range from strike 170-185 ˚ and dip 70-85 ˚, and are aligned with the Iron Range fault. The IRFZ is Proterozoic in age and was created with basin development as one of the rift-parallel (NNW-striking) faults at

approximately 1.4 – 1.5 Ga (Lydon, 2000). The fault can be traced over a distance of 90 km, from the Mt. Thompson area south of the Iron Range to the intersection with the Hall Lake Thrust Fault north of the Iron Range. Due to the lack of outcrop the width of the IRFZ is inferred and varies between 10 to 150 m. To the north of the Goat River anticline, the Iron Range fault divides Proterozoic units from Mesozoic units, indicating reactivation of the northern Iron Range fault in the Mesozoic. Locally, folds and thrust faults at the Iron Range overprint the Proterozoic deformation and are associated with collision of allochthonous terranes from the west (Price and Sears, 2000) which resulted in the most recent basin-wide recognized metamorphic event.

Gently NNW dipping Proterozoic mafic sills (Moyie sills) that are exposed on both sides of the IRFZ are offset by 0 – 75 m (Brown and Stinson, 1995; Stinson and Brown, 1995) and is shown on Figure 2, indicating minor strike-slip movement along the structure. Most sills display pervasive chlorite alteration in proximity to the IRFZ and iron-oxide alteration to magnetite. The sill-sediment contacts show soft-sediment deformation, indicating emplacement of the sills into wet sediments, which is consistent with similar observations throughout the whole Belt-Purcell basin (Lydon, 2000). As some pods of gabbro can be found at stratigraphic levels with no soft-sediment deformation near the fault and there are no sills present at these stratigraphic levels, Stinson and Brown (1995) concluded that the IRFZ was a growth fault during Belt-Purcell basin development and was used by the Moyie sills as a conduit.In the IRFZ the sills are usually sheared and contain euhedral octahedral magnetite and specular

hematite along shear planes. Drag folds observed in the Aldridge Formation and Moyie sills proximal to the IRFZ (Stinson and Brown, 1995) suggest normal displacement of the IRFZ in addition to dextral strike-slip movement indicated by the offset of a Moyie sill.

It is not possible based on the exposed fault and rocks in the study area to conclude whether the IRFZ was active during the Goat River Orogeny, however Mesozoic and Cenozoic transpressional deformation in the southern part of the Belt-Purcell basin appears to have been accommodated along the St.Marys, Hall Creek and Moyie thrust faults (Höy, 1993).

At several locations at the Iron Range, carbonatites occur in outcrop. Due to the lack of significant rock exposure the timing relationships at most localities are difficult to interpret as there are not many cross-cutting relationships except for two localities where carbonatites discordantly cut across Aldridge strata. Dike width varies from 25-50 cm and dyke orientations are west-southwest (220 ˚) with steep dips (80 ˚) to the north. All carbonatites at the Iron Range are weathered and chlorite altered, giving them a greenish appearance in outcrop. They contain predominantly primary calcite along with phlogopite, apatite and various xenoliths derived from felsic intrusions (e.g.,, biotite-granite), that range in size up to several cm. Figure 2 displays the local geology along the Iron Range fault where most of the trenches, drill-pads and showings occur.

Figure 3 shows the residual magnetic field of the Mount Skelly and Iron Range area. The iron-oxide occurrences at the Iron Range coincide with the location of the Iron Range fault, supporting the suggestion that the Iron Range

occurrences are structurally controlled (Staples et al. 2008). At its eastern edge, the Mount Skelly pluton has a very sharp, almost linear boundary that might represent a north-trending structure (i.e., fault); this structure is along the trend of the north-trending IRFZ. On a regional scale and based on the residual magnetic field data, the IRFZ and the Mount Skelly pluton both lie on and along a major regional north-trending feature as seen in Figure 3 . This feature north of the Iron Range and at the eastern boundary of the magnetic expression of the Mount Skelly pluton might be part of the Iron Range fault itself, however this observation is not consistent with the regional geological mapping (Massey et al., 2005) used to derive the faults depicted in Figure 2. The location of the magnetic high at the Iron Range and mapped Iron Range fault matches perfectly, whereas a series of faults delineating a deformational zone to the north of the Iron Range does not match with the eastern boundary of the magnetic expression of the Mount Skelly Pluton. On the residual magnetic field map, north-east trending features (magnetic highs) at and around the Iron Range are interpreted to be the Moyie Sills.
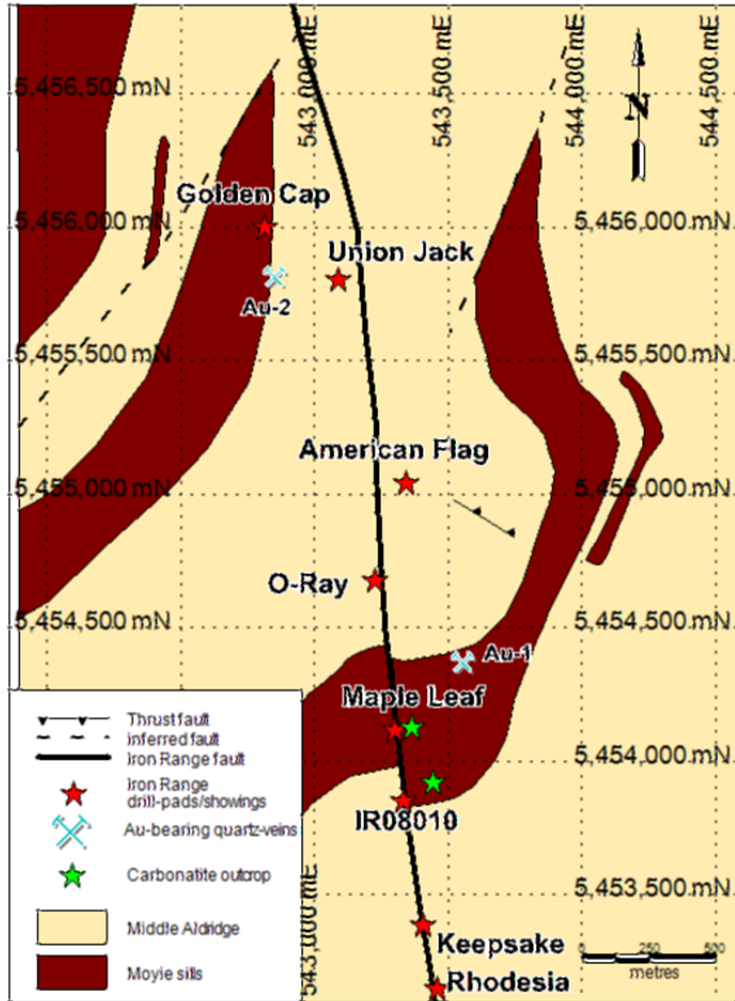
Figure 2: Local geology of the Iron Range including showings, trenches, drill-pads and location of anomalous gold in collected samples (modified from Ryley (2010))
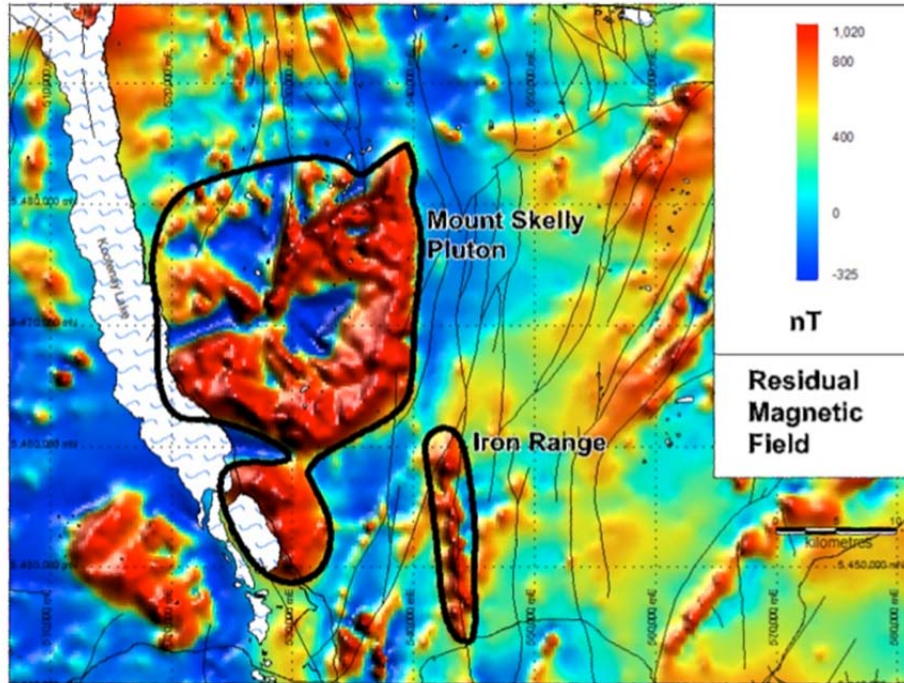
Figure 3: Total residual field of the Mount Skelly pluton and Iron Range (structural features have been taken from Massey et al. (2005); geophysical data acquired from NRCAN (2003))

2: PETROGRAPHY

2.1 Iron-oxide Occurrences

The Iron Range iron-oxide occurrence consists of predominantly hematite and magnetite hosted in the Aldridge Formation and Moyie Sills. As evident from regional aeromagnetic data from the Iron Range (Figure 2), the mineralization is confined to the IRFZ. The iron-oxide mineralized zones vary in width between 20-40 m in the southern part and up to 150m in the northern part of the Iron Range. It is best exposed in five trenches that lie in the zone between the Union Jack and Rhodesia showings (Figure 3). The two main textural styles are massive iron-oxides and brecciated iron-oxides. The massive iron-oxide zone parallels the central-zone of the IRFZ and is flanked by the brecciated iron-oxide zone that is adjacent to zones of strongly altered and iron-oxide veined rocks of the Aldridge Formation and Moyie Sills. As evident from drill-hole data, mineralization can extend locally to 200 m below surface (Ryley, 2009).

2.1.1 Massive Iron-oxides

Massive lenses and veins of iron-oxide are up to several meters wide and pinch and swell along strike (Staples et al., 2008), striking and dipping approximately with the orientation of the Iron Range fault (~ 170-190 / 70-80 ° W). The main iron-bearing minerals are predominantly hematite (~85%) with lesser magnetite (~15%) and trace pyrite and ilmenite. Locally, veins and lenses

of massive iron-oxide are locally composed of only hematite (Figure 4) or somewhat equal amounts of magnetite and hematite.

Hematite is predominantly euhedral and occurs in various grain-sizes and textures and often appears to form pseudo-layers defined by grain-size. Grain size ranges from fine-grained hematite (< 1 mm) up to medium- and coarse-grained hematite (1-2 mm) displaying characteristic blades and martite texture (Figure 4). There are multiple hematite generations, e.g., some hematite has overgrown older hematite (often bladed) (Figure 4), and martite (hematite after magnetite). Mushketovite (magnetite after hematite) is rare but where present is inferred from martite overgrowths on older hematite (Figure 5).

Magnetite occurs mostly as disseminated fine to medium grained (up to 1 mm) subhedral grains or thin veinlets and shows alteration to hematite at grain boundaries. Commonly disseminated magnetite forms pseudo clusters of euhedral magnetite and magnetite replacements of hematite. As with hematite, several magnetite generations with multiple magnetite precipitation/mineralization events resulted in magnetite overgrowths on older magnetite and less commonly hematite (Figure 5).

Ilmenite is very rare and occurs as disseminated euhedral grains coinciding with slightly increased Ti-content in whole rock chemical analysis (Table 10). Fine-grained disseminated pyrite (Figure 4) is rare and may be partly altered to iron-oxides.
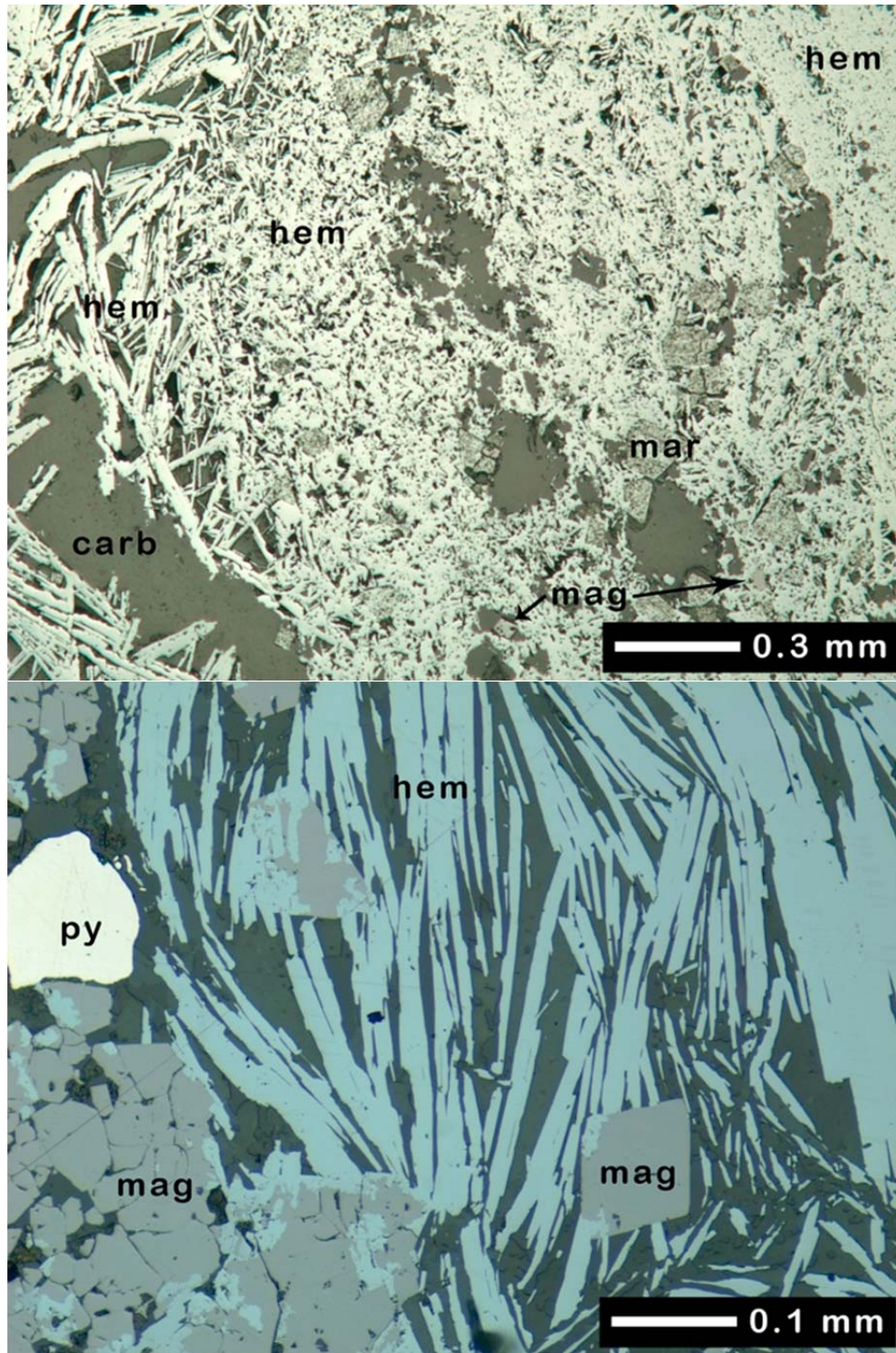
Figure 4: The upper photomicrograph shows variably sized grains of hematite together with magnetite and martite with minor carbonate. The lower photomicrograph, (reflected light image) displays magnetite partly replaced by / altered to hematite (-blades), and hematite (-blades) that grew over / altered to magnetite which in turn is altered to hematite. Both photomicrographs taken in plane polarized reflected light.
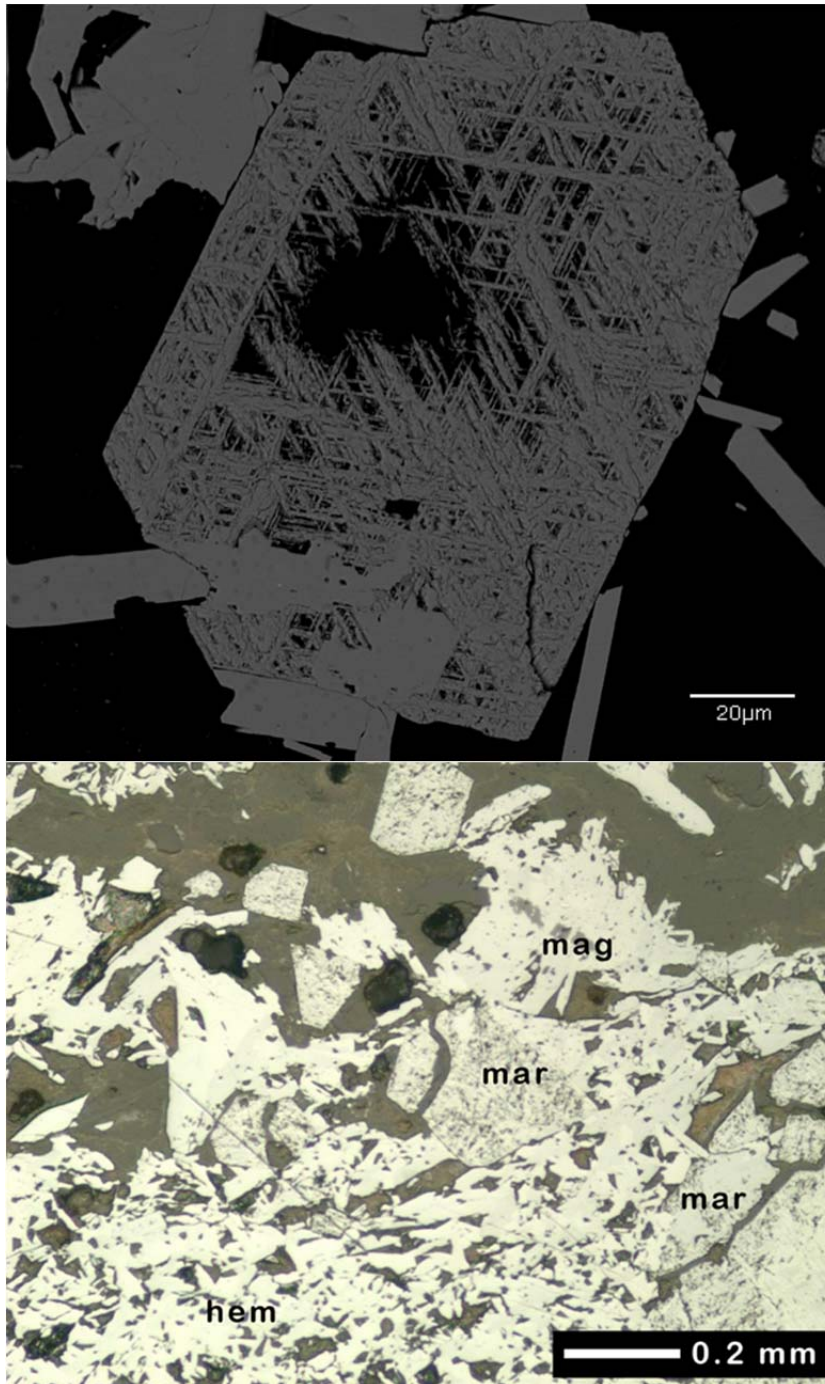
Figure 5: The upper photomicrograph is a BSE SEM-image showing a magnetite crystal entirely replaced by hematite (martite). The lower photomicrograph shows whitish hematite (hem) replaced by magnetite (mag) that is replaced by hematite to form martite (mar). Photomicrograph taken in plane polarized reflected light.

2.1.2 Brecciated Iron-oxides

The massive parts of the iron-oxide mineralization are flanked by an iron-oxide breccia (Figure 6). This clast-supported breccia has anhedral grains of albite and quartz set in an iron-oxide matrix. The breccia is mostly classified as a crackle-breccia with >75% fragments several mm to cm in size, showing little displacement. Veining with quartz and/or iron-oxides is a common feature of this mineralization style with vein widths ranging from mm to several cm. The iron-oxides species in the breccias are identical to the massive iron-oxide species with hematite and lesser magnetite. The iron-oxides are euhedral to subhedral in shape. They exhibit several episodes of iron-oxide precipitation as hematite and magnetite repeatedly replace each other as noted in the massive iron-oxides. Rare fine-grained pyrite is disseminated and party altered to iron-oxides, and hairline thin pyrite veinlets have been noted at some showings.

Although there is a gradational transition from the massive iron-oxides to the brecciated iron-oxides (Figure 7), it is suspected that the brecciated iron-oxides themselves transition into the iron-oxide veined and intensely altered host rock (i.e., Aldridge Formation and Moyie Sills). Locally the host rock shows subtle crackle-brecciation associated with iron-oxides.
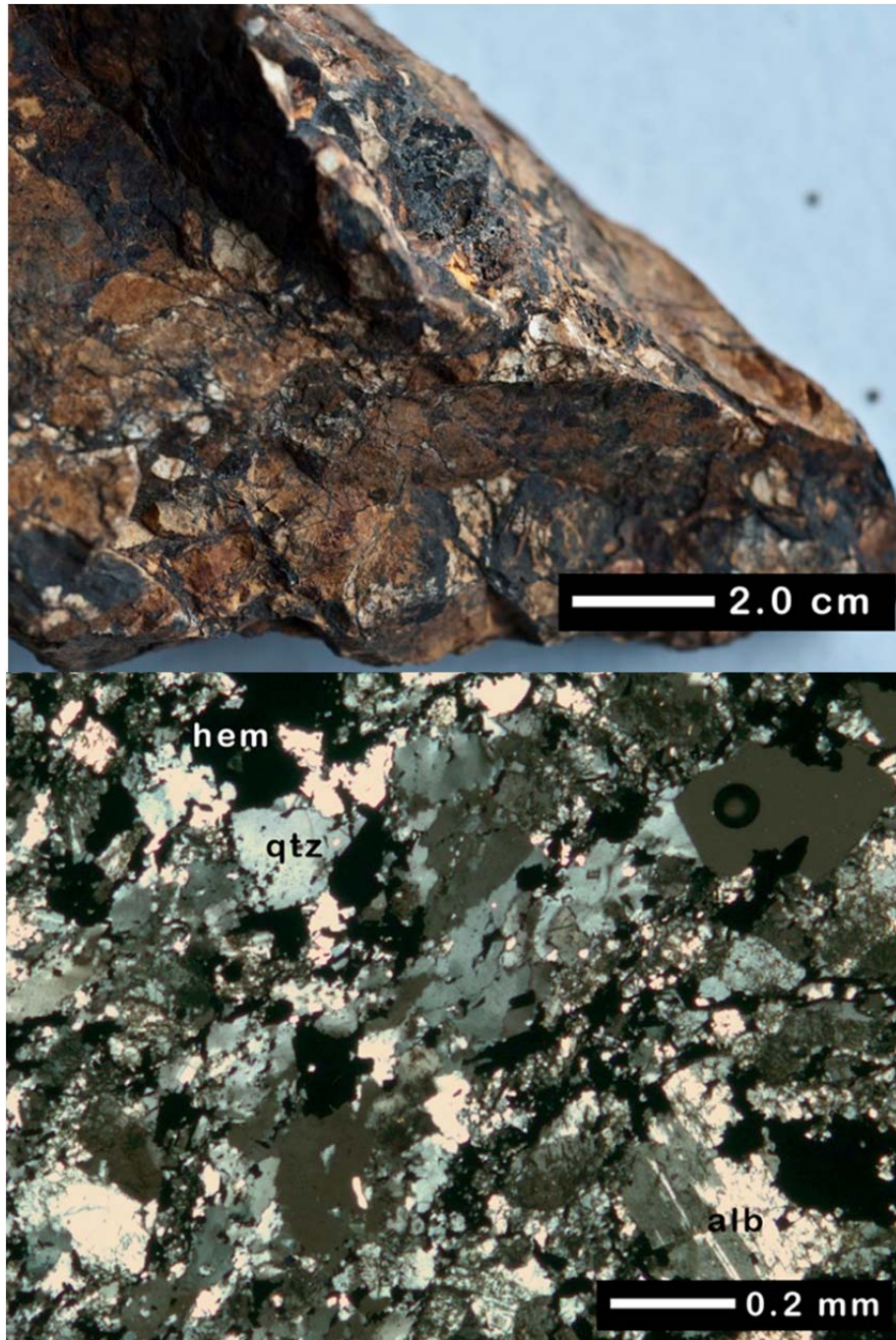
Figure 6: The upper photograph shows an iron-oxide breccia with fragments of Middle Aldridge host rock veined by iron-oxides. The lower photomicrograph taken in plane polarized light under crossed polars shows iron-oxide breccia with anhedral quartz (qtz) and albite (alb) with interstitial hematite (hem).

Figure 7: Hand-specimen showing the transition from the more massive iron-oxide rich layer (top left) to iron-oxide breccia (central and lower-right) , veined by (black) iron-oxide and (greyish) quartz veinlets.

3: ALTERATION

Several alteration assemblages of the lithologies that host the iron-oxide occurrences have been noted, some of which are directly associated with the iron-oxide mineralization. The usage of the terms 'distal' and 'proximal' corresponds to distances from the IRFZ and the iron-oxide occurrences of more than 25 m and less than 25 m, respectively. The host-lithologies are the Aldridge strata and Moyie sills. Figure 8 at the end of this chapter illustrates the timing relationships as they have been observed in this study.

3.1 (Regional) Chlorite +/- Epidote Alteration

Regional metamorphic chlorite with minor epidote alteration is well displayed in the Moyie Sills, which contain 50% 2-10 mm chlorite-epidote altered hornblende (after augite) and 35% 5 mm plagioclase that is often cloudy due to included fine grained epidote (Höy, 1989). The fine grained matrix (~ 15%) is commonly altered to chlorite. Overall, this alteration gives the sills a slight brown to greenish appearance, with more intense chlorite-epidote alteration resulting in more greenish coloration.

3.2 Albite-Chlorite-Hematite-Magnetite +/- Silica Alteration

The main alteration stage responsible for most of the iron-oxide occurrences and alteration of the host lithologies is albite-chlorite-hematite-magnetite +/- silica (Figure 9). This alteration type is the most common and

abundant at the Iron Range. The intensity of this alteration varies and decreases away from the IRFZ. Furthermore, albite and iron-oxide abundances seem to increase towards the IRFZ (ranging from 5-30% and 5-90% respectively), and chlorite becomes less significant (20-10%). However, there are some intensely chlorite-silica-magnetite-hematite (15%, 25%, 10% and 40%, respectively) altered rock masses proximal to the IRFZ, with albite alteration ranging from minor (5-10%) to absent. The colour of this alteration assemblage can be a distinct dark green but is usually dark reddish green and dark bluish green to black depending on the iron-oxide content.

Alteration in the Moyie Sills distal to the IRFZ is expressed as 'bleaching' (albitization) of gabbro resulting in a dirty white and green coloured gabbro (Figure 9) with locally 5% of 2-5 mm euhedral magnetite grains. Magnetite occurs in Moyie Sills as a primary (accessory) mineral (~1%) as individual crystals or as cumulates. However, it occurs more commonly as an alteration mineral, either as euhedral disseminations (up to 5%) or as veins or veinlets and patches of fine grained <1 mm magnetite (up to 15%). Some Moyie Sills are deformed in IRFZ parallel shear zones, and show moderate chloritic (25%) with weak albitic (10%) alteration and up to 5% euhedral magnetite crystals along shear planes. Albitization in the Middle Aldridge Formation distal to the IRFZ is mostly characterized by white, light brown and rose discoloration.

Although the IRFZ distal alteration preserves most of the primary host lithology textures, the IRFZ proximal alteration is mostly texture destructive. Middle Aldridge Formation rocks that are usually (dark) grey have become a

white to brown, coherent mass forming a crackle-breccia with iron-oxides laminated by hematite with lesser magnetite, and Moyie Sills have become intensely albite (20-40 %) altered and iron-oxide veined (30-40 %) with minor chlorite and silica alteration (15% and 1-5%, respectively). In addition, some strongly albitized (>40 %) gabbroic sills and Middle Aldridge sediments locally have 1 % fine-grained hematite or magnetite crystals (<1 mm) giving the rock a pseudo 'felsic intrusive' appearance. Overall the hematite to magnetite abundance is 5:1.

3.3 Silica-Hematite-Magnetite Alteration

Postdating the albite-chlorite-hematite-magnetite +/- silica alteration is silica-magnetite-hematite (15%, 15% and 70% respectively) alteration characterized by 1-15 mm wide quartz veinlets and/or hematite-magnetite veinlets (Figures 9,10), as well as altering hematite to magnetite and vice versa which indicates changes in oxidation state of the hydrothermal fluid. The hallmark feature of this change in oxidation state at the Iron Range is the presence of martite, which is a hematite pseudomorph after magnetite, where magnetite is completely altered to hematite while preserving the crystal outline of the relict magnetite grain (Figures 4, 5). The relative abundance of the iron-oxide phases is 60% hematite, 25% magnetite, 15% martite and <1 % mushketovite (magnetite after hematite).

Quartz-veinlets (1-15 mm wide with microcrystalline quartz) commonly have mm-thick layers of fine-grained (<1 mm) hematite and/or magnetite at the

contact to the altered wall rock or earlier iron-oxide generations. Locally, veinlets appear as parallel layers of 1-2 mm thin iron-oxide and to a lesser extent silica.

As this alteration is dominated by silica and iron-oxide, the resulting colour and texture of the affected rock is grey to dark grey with veining. With respect to other alteration types, this alteration is much less pervasive and abundant than the albite-chlorite-hematite-magnetite +/- silica alteration.

3.4 Silica Alteration

Silica alteration is characterized by quartz-veining (1-4 mm wide with microcrystalline quartz), commonly as sheeted vein-sets locally forming a weak stockwork and in places as pervasive silicification (silica replacement of the host rock). In many cases, this alteration post-dates the iron-oxide occurrences as sheeted quartz-veins cut massive and brecciated iron-oxides. It is best observed in buff-brown (slightly oxidized) strongly albitized Aldridge sedimentary rock where the degree of alteration can be up to 5-10% of the whole rock, increasing up to 25% in rock units displaying pervasive secondary silica flooding.

Locally, 2-5 % fine grained (<1 mm) masses of goethite with minimal amounts (<0.5 %) of <1 mm glassy limonite or copper wad are present. All gold-occurrences are found in zones with strong quartz-veining and/or weak quartz stockwork within albitized host-rock or albite-chlorite-hematite-magnetite +/- silica altered Moyie sills. In addition, very fine grained (micron-sized) hematite, magnetite and pyrite are locally present in these quartz-veins associated with gold-mineralization (as described in Chapter 4.2). Oxidation of primary sulphides,

i.e., pyrite or chalcopyrite is evident by box-work textures in the goethite and glassy limonite and only present in and near zones with this silica alteration.

3.5 Sericite Alteration

Sericite alteration has been noted in one drill-hole at 200 m depth along and surrounding minor shears. Sericite may represent hydrothermally altered sodic feldspar, which is abundant within the alteration halo around the IRFZ (Figure 10). It occurs as very fine-grained (sub-mm) muscovite flakes locally postdating other alteration assemblages and directly associated with chalcopyrite and pyrite. It occurs as elongated masses in shear zones and as fine disseminations farther away from the shear zones. It is notable that to date, Cu-mineralization has been noted only with sericite alteration. Due to limited samples with sericite alteration, the relationship with other alteration assemblages is speculative. The sericite alteration generally comprises less than 5% of the rock and is noted as whitish-yellow micaceous zones where observed.

3.6 Carbonate Alteration

Carbonate alteration is characterized by 1-5 mm wide bone-white calcite veinlets, reddish ankerite and interstitial filling of void space in massive iron-oxides (Figure 4). In most cases it cuts and post-dates all other alteration assemblages. Carbonate veinlets contain microcrystalline Fe-carbonate (i.e., ankerite) or calcite and carbonate in-fill of void-space in massive iron-oxides can range up to 1 mm. This alteration occurs mostly in trace amounts and can be found in most lithologies proximal to the IRFZ.

The carbonatite dykes at and around the Iron Range however are moderately to strongly carbonate altered (10-25%), where much of the matrix consists of sub-mm to 2 mm calcite grains.
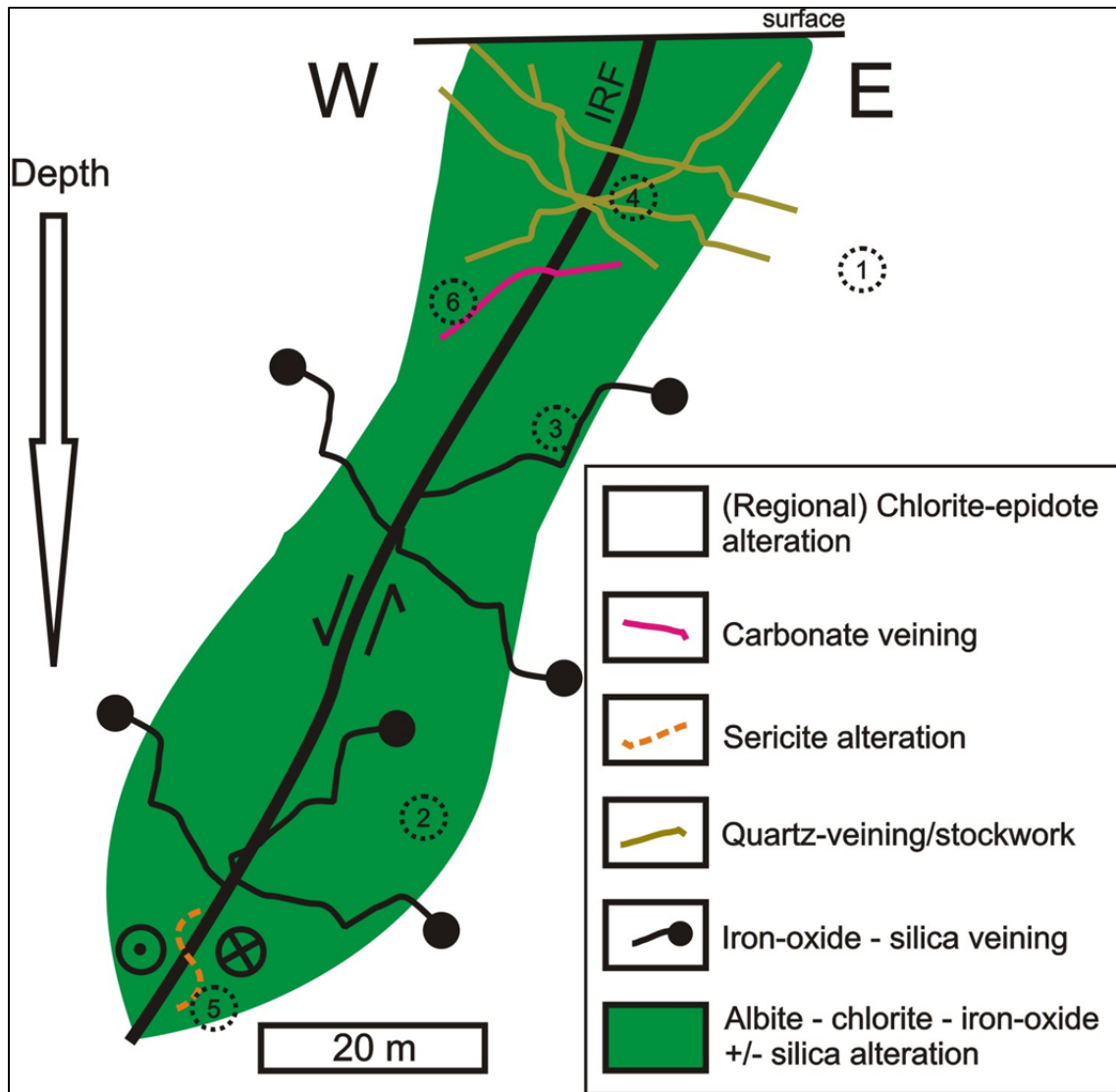
Figure 8: Observed timing relationships of the alteration assemblages at the Iron Range which are numbered sequentially in the (ascending) order they occurred along the west dipping Iron Range fault (IRF). (1) represents the regional chlorite-epidote alteration; (2) represents the albite-chlorite-hematite-magnetite +/- silica alteration; (3) represents the silica-hematite-magnetite alteration; (4) represents the silica alteration; (5) represents the sericite alteration and (6) represents the carbonate alteration. Timing relationship between (4), (5) and (6) is uncertain. Vertical scale exaggerated.
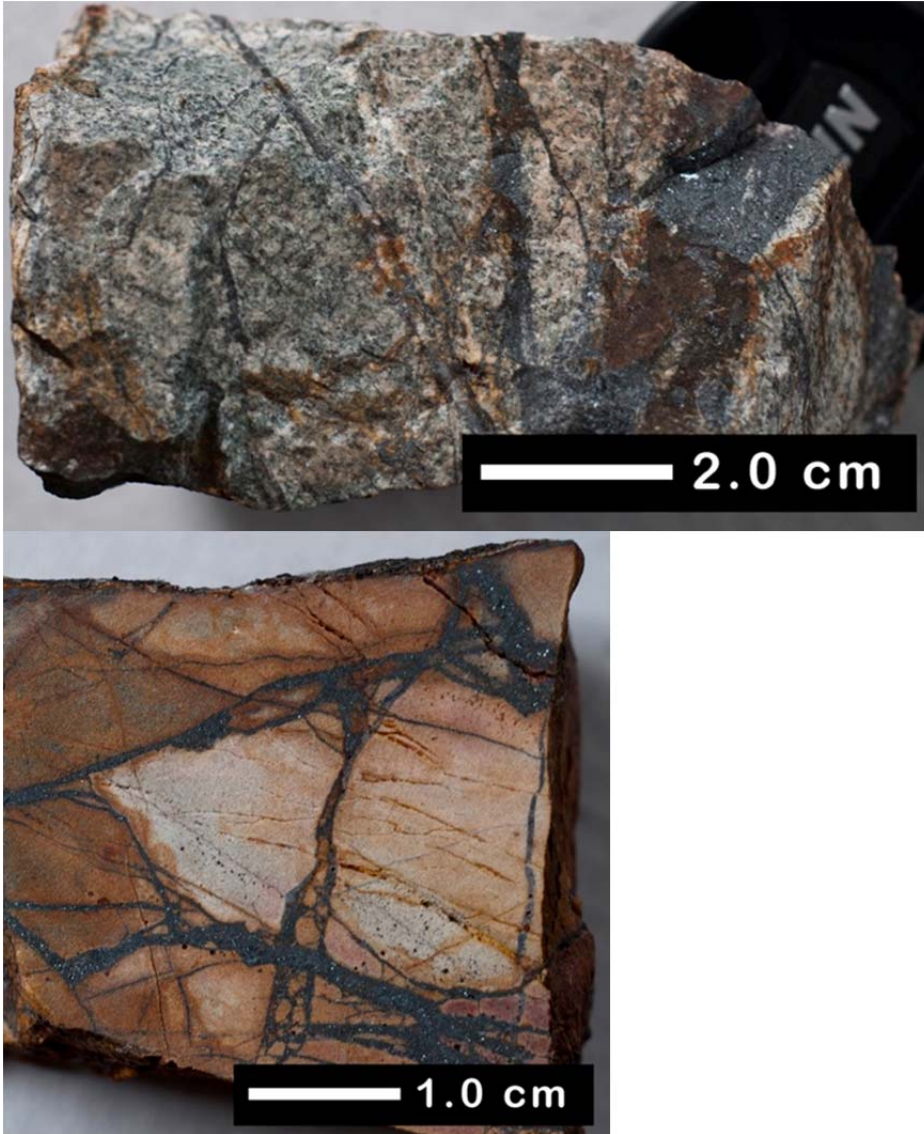
Figure 9: Moyie sill hand specimen (upper photograph) showing iron-oxide +/- quartz veined chlorite-albite altered rock. The lower photograph displays hydrothermally brecciated intensely albite altered Middle Aldridge strata veined by iron-oxides with greenish patches of chlorite alteration.
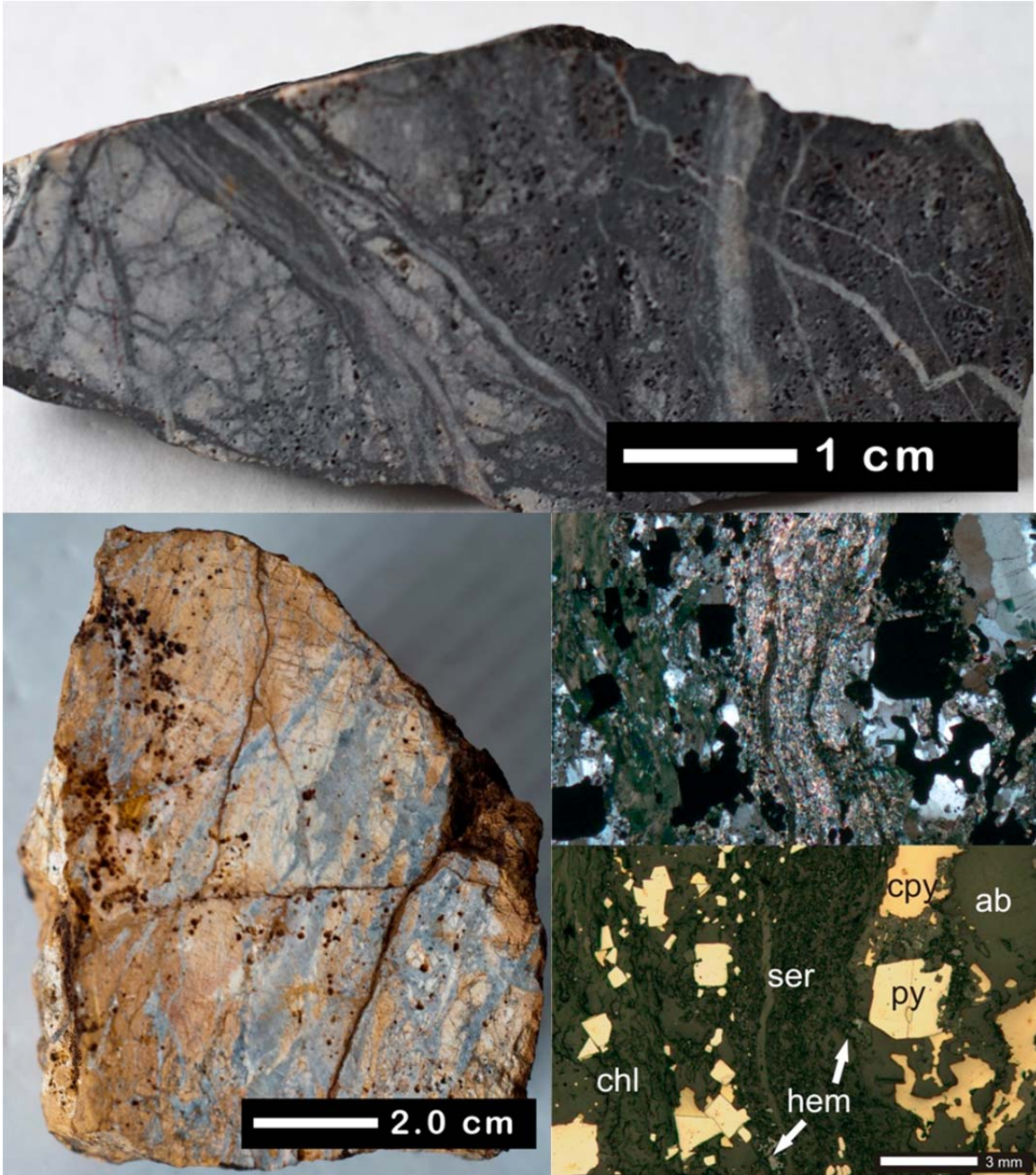
Figure 10: Strong quartz alteration and veining of brecciated to massive iron-oxides (upper photo). Strong quartz veining of albite altered Middle Aldridge strata with oxidized primary sulphides leaving behind cubic pits (lower lefthand photograph). Corresponding crossed-polar transmitted and plane-polarized reflected light photomicrographs (lower right) show the sericite (ser) chlorite (chl) altered breccia with chalcopyrite (cpy) and pyrite (py) and minor hematite (hem).

4: BASE AND PRECIOUS METAL MINERALIZATION

4.1 Copper Mineralization

The 2008 drilling program at the Iron Range identified Cu-mineralization where it was logged in the two meters of a drill hole (IR08018) at about 200 m depth below surface. The Cu-mineral has been identified as chalcopyrite, which occurs together with pyrite. The mineralization style is finely disseminated with the Cu-bearing intervals averaging 0.14% Cu (Eagle Plains Resources, personal communication, 2009).

The mineralization occurs in a zone that is very similar to albite-chlorite-hematite-magnetite +/- silica altered iron-oxide breccias with local sericite (Figure 10, Chapter 3.). All chalcopyrite occurs exclusively with quartz and locally contains pyrite inclusions. Chalcopyrite grain size ranges from a few hundred microns to aggregates of up to 1 cm.

Magnetite is commonly spatially associated with chalcopyrite, which it locally overgrows (Figure 11). Also, the presence of minor shears and sericite associated with the copper-mineralization, suggests it was introduced into the system in the later stage(s) as shears or sericite postdate albite-chlorite-hematite-magnetite +/- silica altered Aldridge strata.
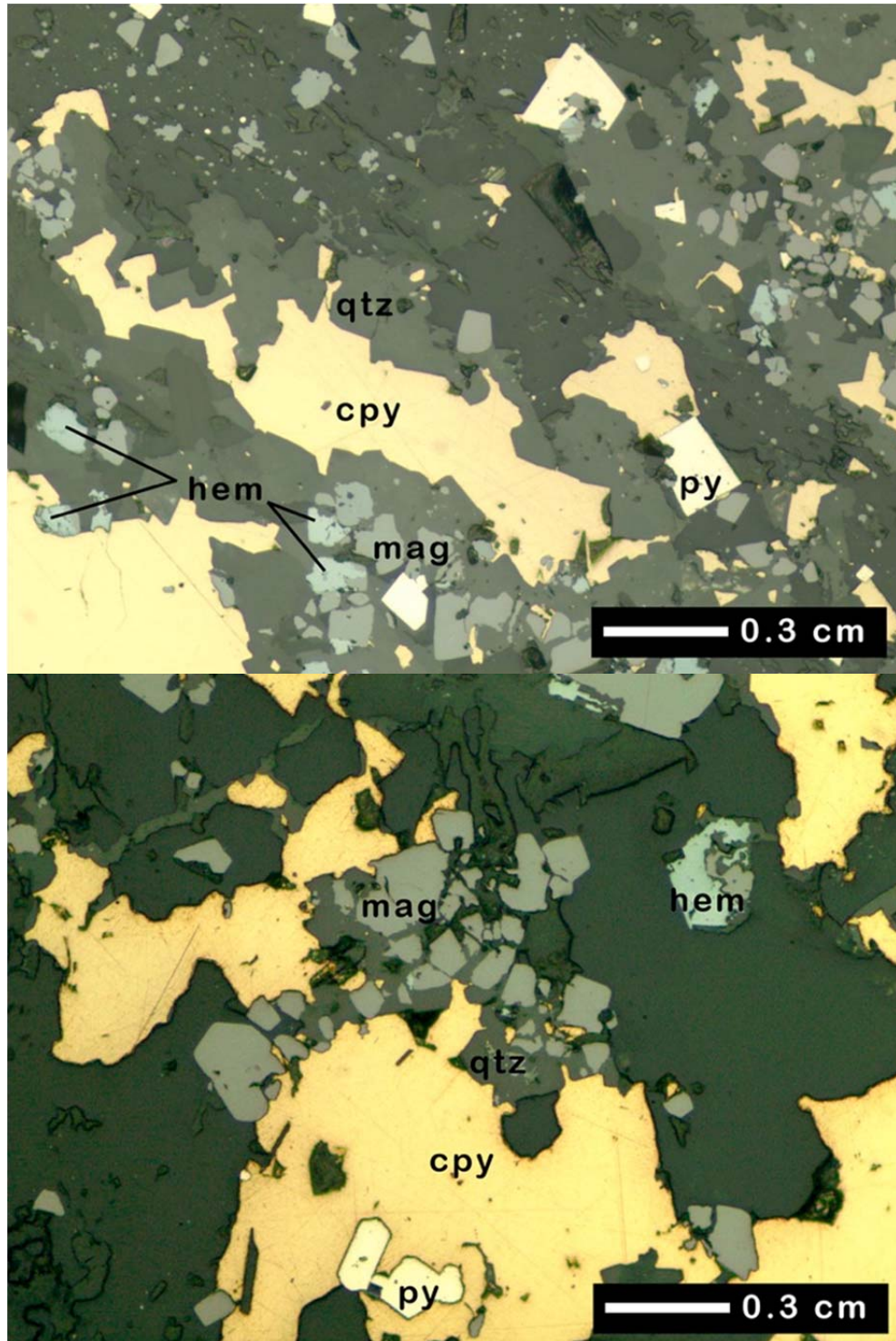
Figure 11: Plane polarized reflected light photomicrographs showing strongly altered Middle Aldridge strata with pyrite (py) and chalcopyrite (cpy) with hematite (hem) and magnetite (mag) in a (grey) quartz +/- chlorite +/- carbonate matrix.

4.2 Gold Mineralization

The 2008 drilling program identified high-grade gold mineralization (Eagle Plains Resources, personal communication, 2009) at relatively shallow depths near the massive and brecciated iron-oxide occurrence at surface (Hole IR08006, Oray showing (Figure 2, Chapter 1). Approximately 10-20 m below surface, high-grade gold can be traced over a length of 7 m, averaging 51.62 g/t gold (with gold grades locally averaging between 90 and 115 g/t). The gold-rich zone is located in a weakly developed quartz-stockwork situated within a strong clay-albite (+ silica-chlorite-hematite-magnetite) altered meta-sediments in the hanging wall of the IRFZ. Strong clay alteration (i.e., limonite), as well as quartz-stockwork are rarely observed at the Iron Range. The massive and brecciated iron-oxides in the vicinity of the gold bearing quartz-veins are very silica-rich compared to all other altered lithologies at the Iron Range and are characterized by quartz-veining and pervasive secondary silica (i.e. quartz) alteration resulting in a very hard and slight cloudy or milky coloured rock. The strong quartz veining and therefore the gold mineralization likely postdate massive and brecciated iron-oxide mineralization.

Due to its relative rarity in the study area, only one gold-bearing sample from the high-grade zone containing free gold was studied. The gold is hosted in a matrix of predominantly subhedral quartz (Figure 12). The gold occurs as <40um grains and <10um thin crack-infill with inclusions of fine-grained euhedral magnetite, hematite and pyrite. Energy dispersive gold-analysis performed at

SFU indicates that the gold at the Iron Range is predominantly native gold with approximately 5 weight percent silver.
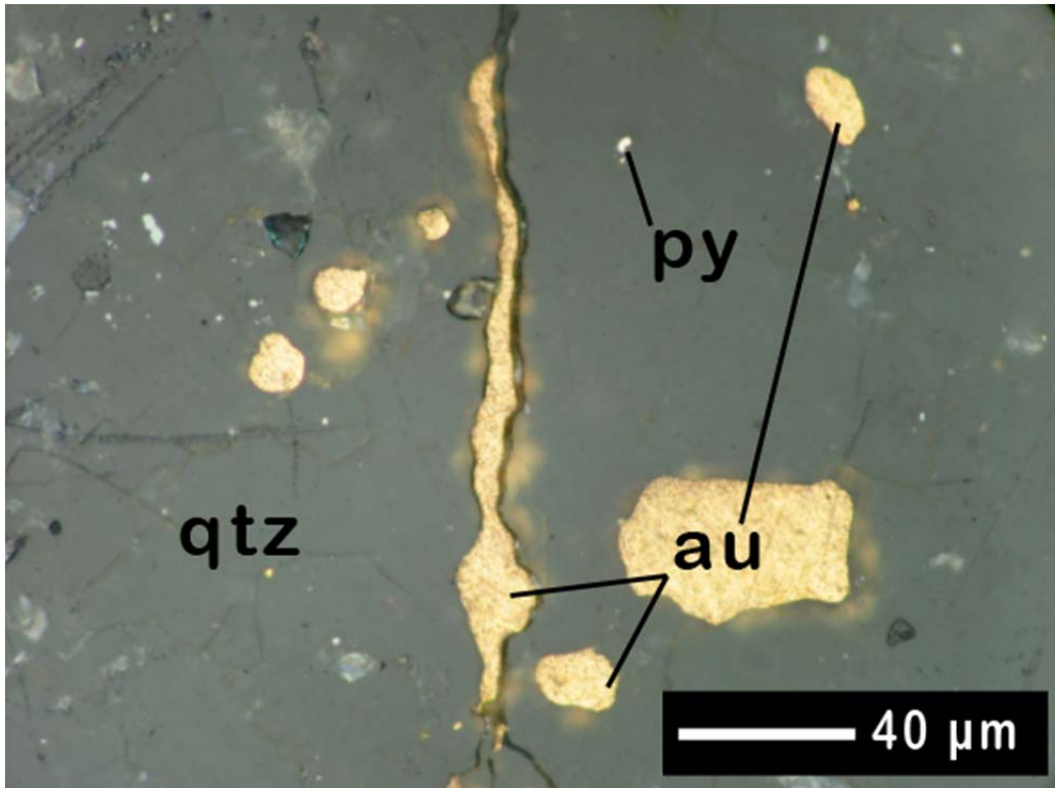
Figure 12: Photomicrograph of gold (au) within quartz (qtz)matrix with minor pyrite (py) inclusions. Photograph taken in plane polarized reflected light.

In 2009 the area surrounding the Oray-showing was trenched extensively, but the 2008 Au-grades were not reproducible. A similarly altered and quartz-veined stratigraphy (as at the Oray) is present near the Maple Leaf showing ("Au-1" on Figure 2). Itthat contains 27 ppb Au and 121 ppm Cu (sample "MG08-20E" in Table 10). Oxidation of primary sulphides is evident from the presence of goethite and boxwork texture (cubic iron-oxide stained pits).

Within propylitic altered (chlorite-epidote) gabbroic Moyie sills at point "Au-2" on Figure 2, north trending quartz veins contain chalcopyrite and goethite. Gold has not been visually identified, but geochemical analysis revealed 1.81 g/t Au.

4.3 Rare Earth Phases

Although the mineral assemblage of the iron-oxide mineralization is rather simple, investigations of some of the Iron Range samples indicated rare earth and precious element bearing phases. These mineral phases are too small to be seen in hand-specimen or under the microscope, however due to their ability to incorporate relatively heavy elements, they can be easily located and identified utilizing the SEM.

Associated with chalcopyrite and pyrite mineralization or found as inclusion is chalcopyrite in hole IR08018 at depth of 305 m (inclined drill-hole) are Niobium-Yttrium-Titanium (Nb-Y-Ti) bearing oxides (Figure 13), possibly a euxenite variety with the general formula $(Y,Ca,Ce)(Nb,Ta,Ti)_2O_6$. The relatively small iron-peak in the spectra is attributed to the overall iron-rich nature of the host material and relatively small size of the REE-phases.

Massive iron-oxides from the Rhodesia showing at surface contain small grains (5-15 um) of a Niobium-Tungston-Scandium-Iron (Nb-W-Sc-Fe) oxide (Figure 14). Known REE-phases with these elements are wolframo-ixiolite (general formula: $(Nb, W, Ta, Fe, Fe, Mn, Nb)_2O_4$), which is a Ixiolite variety with the general formula: $(Nb, Ta, Sn, Fe, Mn)_4O_8$. Some Wolframo-Ixiolite might be

enriched in scandium, which is a minor constituent for Nb in REE minerals from REE granitic pegmatites (Wise et al., 1998).

Surface samples of massive iron-oxide samples from the Golden Cap adit contain Niobium +/- Titanium +/- Iron (Nb +/- Ti +/- Fe) bearing oxide phases (Figure 15). Major Nb-bearing phases in combination with Ti and Fe are columbite with the general formula: $((Fe, Mn, Mg)(Nb, Ta)_2O_6)$ and Ixiolite varieties with the general formula: $(Nb, Ta, Sn, Fe, Mn)_4O_8$.

The minor REE-mineralization is contemporaneous with the copper and iron-oxide mineralization as they are often spatially associated, attached to or included in another. However, there is no clear timing relationship between the gold mineralization and the REE-phases. However, gold mineralization occurs in a vastly different environment at the Iron Range (weak quartz stockwork) and based this observation gold mineralization postdates both copper- and REE-mineralization (as is the quartz-stockwork that hosts the gold).
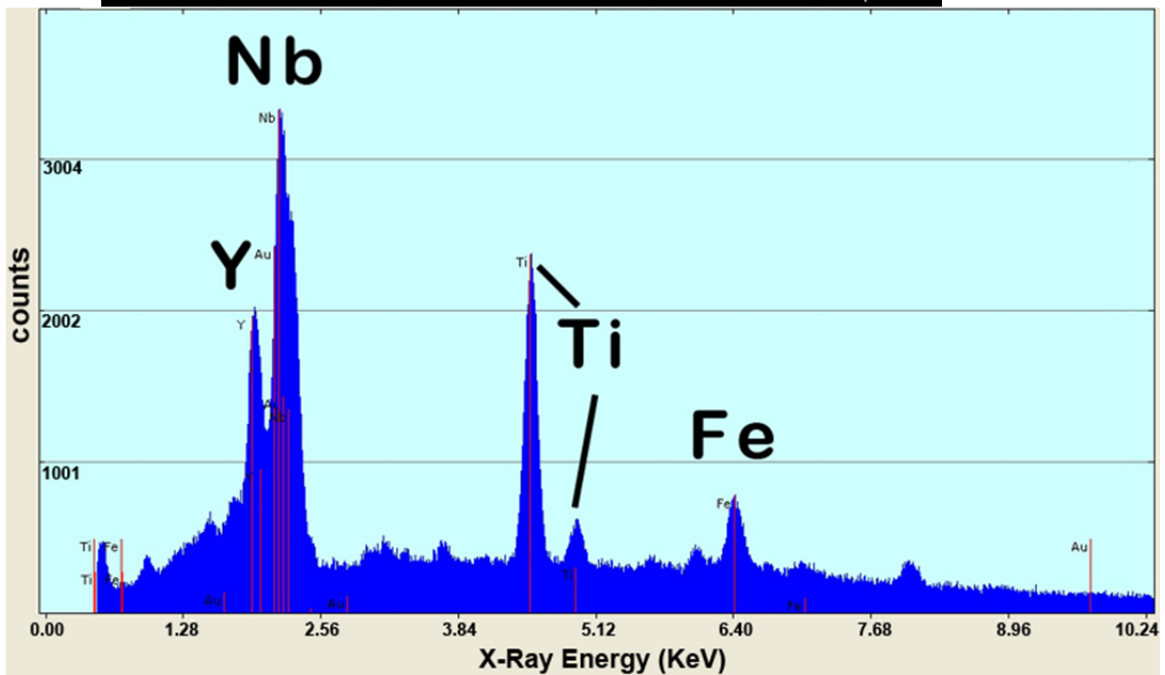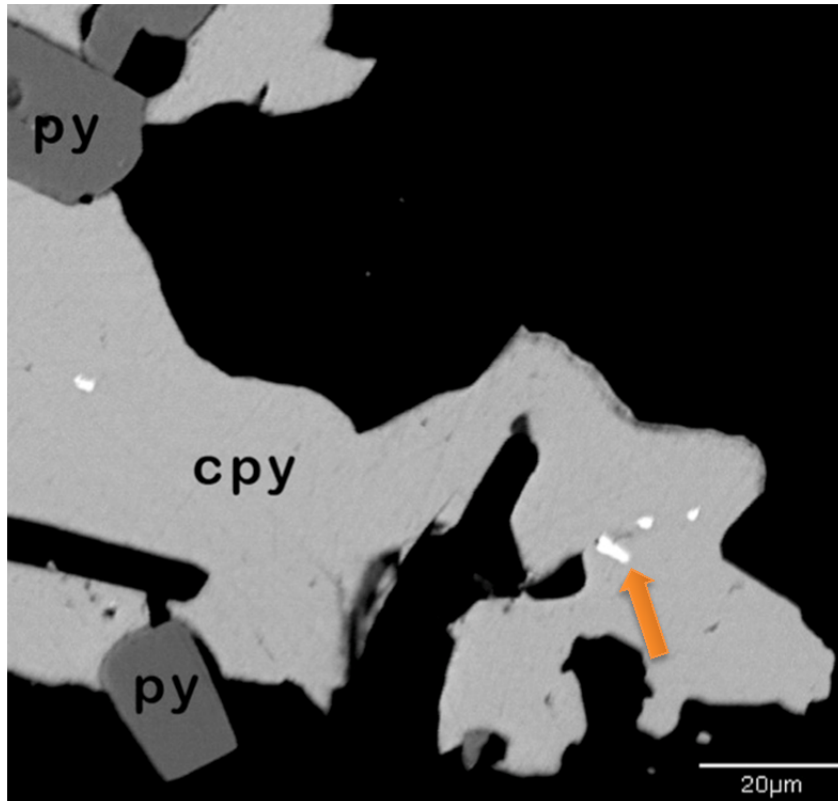
Figure 13: BSE image and energy dispersive spectrum of a (white) euxenite-variety found as inclusions in chalcopyrite (cpy) and pyrite (py). The orange arrow indicates analysis point.
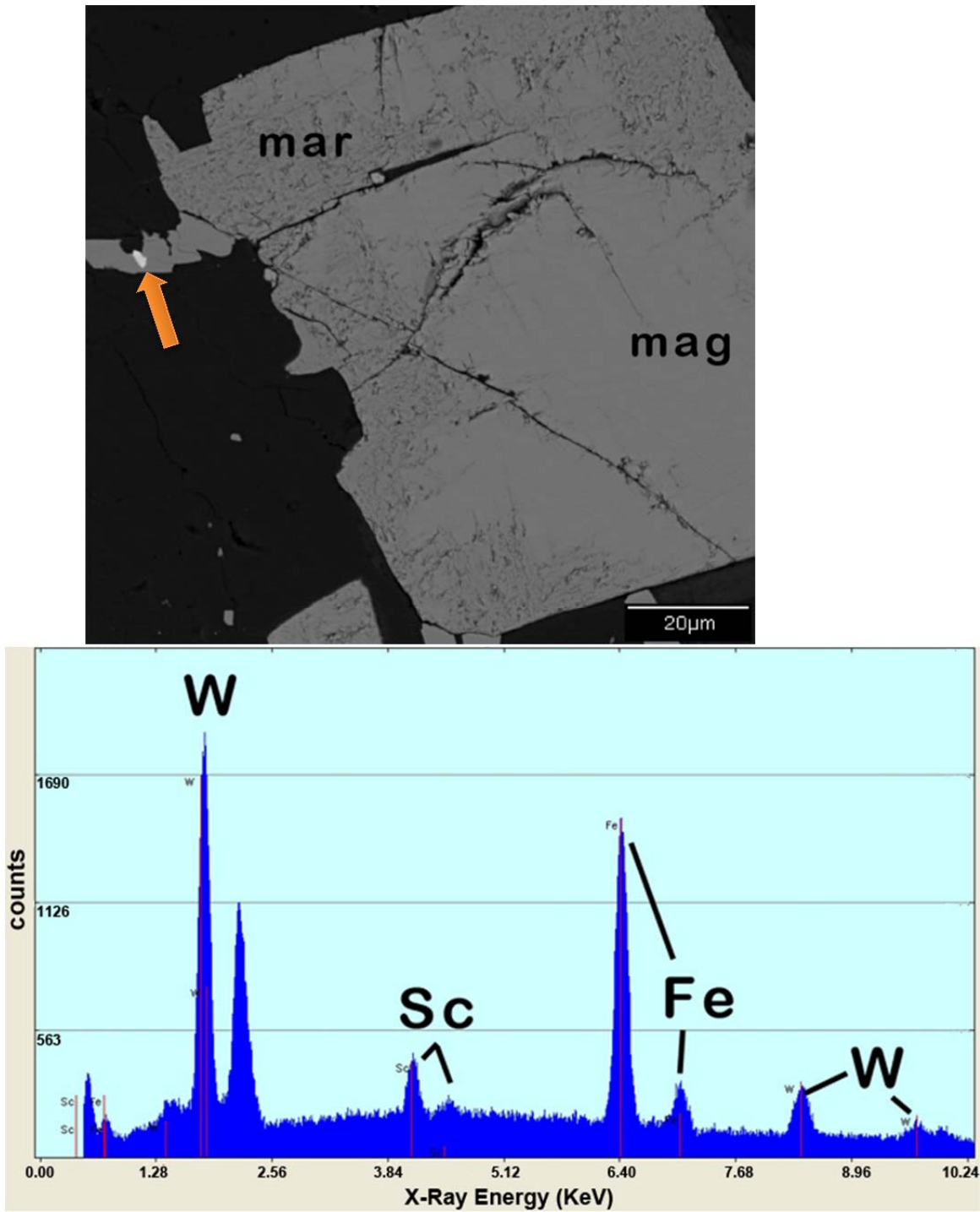
Figure 14: BSE image and energy dispersive spectrum of scandium enriched (white) wolframo-ixiolite found as inclusions in magnetite (mag) and martite (mar). The orange arrow indicates analysis point.
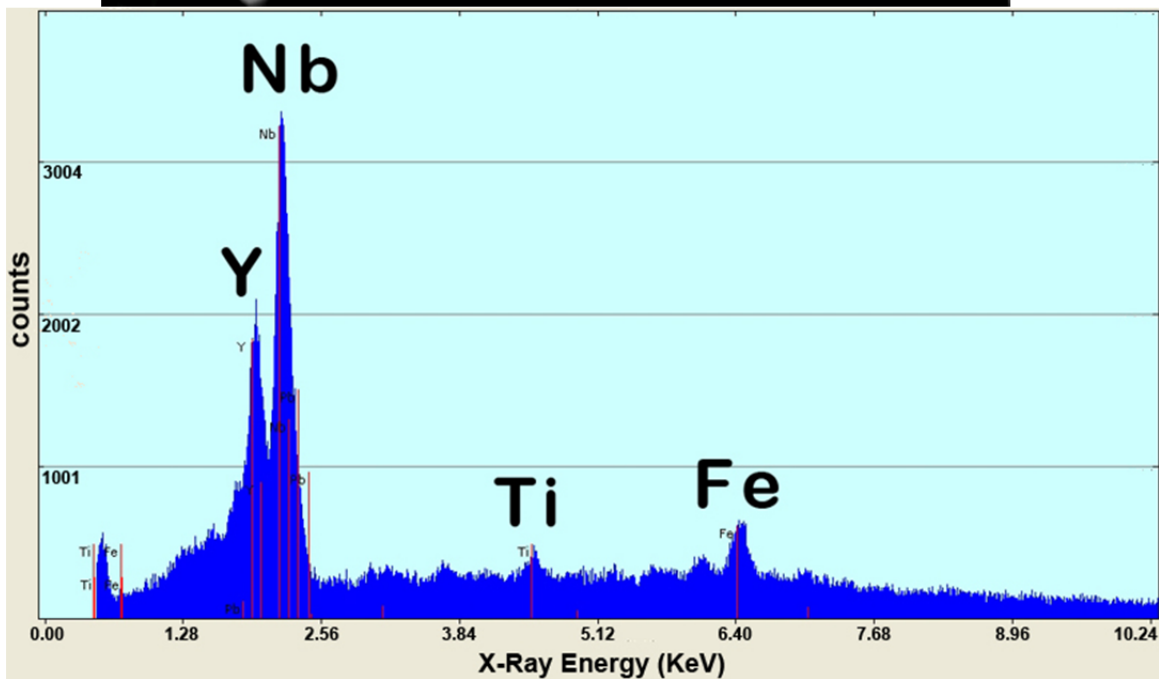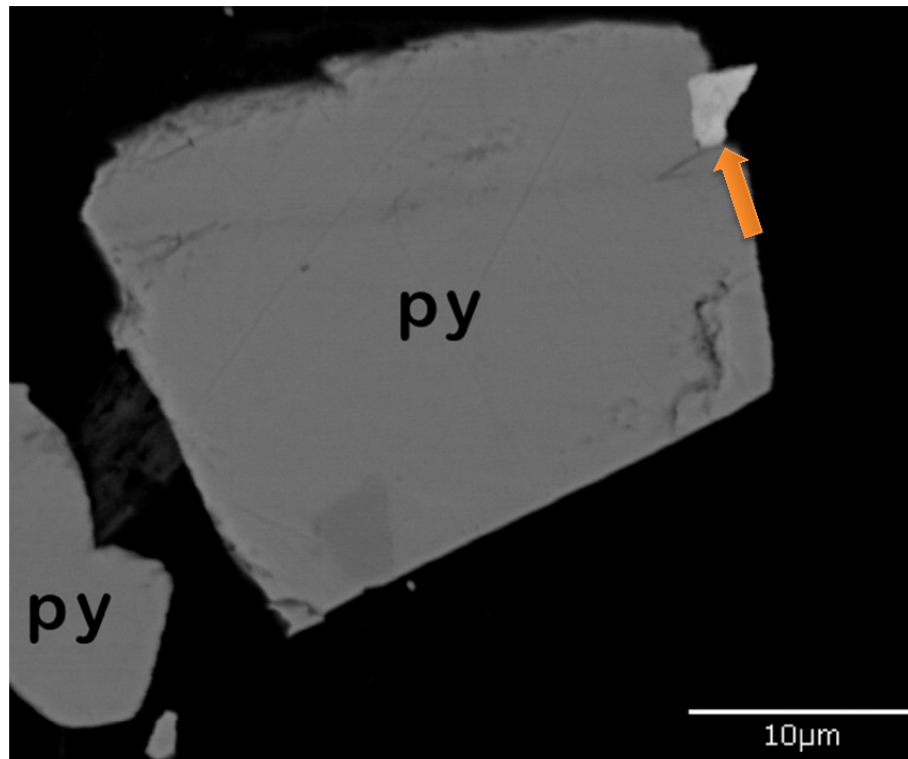
Figure 15: BSE image and energy dispersive spectrum of either columbite- or ixiolite-variety (light grey) found as inclusions in pyrite (py). The orange arrow indicates analysis point.

5: PT CONDITIONS

5.1 Fluid Inclusion Study

The following fluid inclusion section is partially from a previous study reported in Staples et al. (2008) and reinterpreted here. The fluid inclusions from the IRFZ are very saline and can be divided into two major types: Carbonic Absent (CA) fluids and Carbonic Present (CP) fluids. The CA fluids were described in Staples et al. (2008). Both fluid inclusion types appear similar, are often only distinguished microthermometrically, and consist of two-phase (brine + vapour) inclusions at room temperature with the vapour portions for the CA and CP inclusions occupying approximately 9 and 14 volume percent respectively (Figure 16).

No growth zones were observed within any of the quartz or albite hosting fluid inclusions. Although both inclusion types occur in both minerals, in general quartz is a better host and all inclusion measurements were made on fluid inclusions hosted in quartz. Furthermore, in rocks from the Iron Range fluid inclusions in quartz are larger and more abundant than in albite (fluid inclusions in quartz are up to 10 microns along their longest axis and usually ellipsoidal shaped). The lack of growth zones precludes identifying any inclusions as primary or pseudosecondary, thus all inclusions are secondary, but have been petrographically grouped into fluid inclusion assemblages, generally related to each other along the same fracture. Although being classified as secondary, the

CA and CP fluid inclusions are the only ones found within quartz and thus have to represent at least one fluid involved in the iron-oxide precipitation at the Iron Range. All fluid inclusions measured were contained within doubly polished plates. The measurements were made with a Linkam THMS-G 600 heating freezing stage attached to an Olympus BX50 microscope equipped with 40 and 100 X long working distance Olympus objectives. The stage is capable of measurements in the -190 to +500 ºC range. The stage was calibrated with two synthetic fluid inclusions having four readily observable phase transitions at 56.6, 0.0, 10.0 and 374.1 ºC. The stage was periodically checked against the standards and results were always within ±0.1 ºC of the two low temperature standards and within 1.0 ºC of the higher temperature phase transition. From these measurements I conclude that the (2σ) error is less than ±0.2 ºC for temperatures below 50 ºC and 2.0 ºC for higher temperatures. Because the inclusions were generally much less than 10 microns in their maximum dimension, it was difficult to make measurements of some phase transitions.

The microthermometric behaviour of the CA inclusions upon cooling from room temperature commenced with the nucleation of ice ranging from temperatures of -58 to -77 °C. Further cooling to -180 °C did not result in the nucleation of any additional phases. Upon heating the inclusions displayed very low first melt (eutectic) temperatures of approximately -50 °C. Such low eutectic temperatures are common in very saline inclusions and are generally indicative of $CaCl_2$ within the inclusions (Vanko et al., 1988). Upon further heating the ice within the inclusions continued to melt with final melting temperatures occurring

over the range of -25 to -21 °C, well below the NaCl-H_2O system eutectic at -20.8 °C again indicating the presence of other salt components such as KCl or $CaCl_2$ (Vanko et al., 1988). Additional heating resulted in the continuous shrinking of the vapour bubble until total homogenization to the liquid generally occurred over the temperature range from approximately 150 to 200 °C with a few outliers around 250 °C.

Cooling the CP inclusions results in the nucleation of clathrate and ice over the approximate temperature ranges of -55 to -67 and -68 to -75 °C, respectively. Further cooling to below -180 °C did not nucleate any additional phases. Heating the CP inclusions resulted in first melt temperatures again ranging around -50 °C. Continued heating caused the melting of ice and clathrate over the ranges -25 to -21 and -18 to -10 °C, respectively. Total homogenization into the liquid phase generally took place in the temperature range 210 to 250 °C.

The microthermometric fluid inclusion data has been used to calculate approximate compositions and ischores for the two fluid inclusions types (CA (=brine + H_2O) and CP (=brine + CO_2)). The isochores are shown in Figure 18 within Chapter 5.3, which also contains data from the staple isotope studies discussed in Chapter 5.3. The two fluid inclusion types (i.e. CA and CP) cannot represent the liquid and vapour portions of a boling system, as the compositions are not consistent with the liquid and vapour portions of a boiling system and both fluid inclusion types homogenize to the liquid phase and homogenize at different temperatures. If the two fluid inclusion types represented the liquid and vapour portions of a boiling system, one type would homogenize to the vapour

and the other to liquid upon heating, and the homogenization temperatures would be the same for both fluid inclusion types. Trapping conditions for the CA fluid inclusions occur at lower pressure and temperatures than the CP isochores. This is consistent with fluid inclusion petrography, which indicates that the CP fluid inclusions trails crosscut the CA fluid inclusion trails. This is also consistent with petrographic observations of carbonate being a relatively late phase in the petrogenesis of these vein systems.

The source of the fluids trapped within the fluid cannot be determined with the current data.
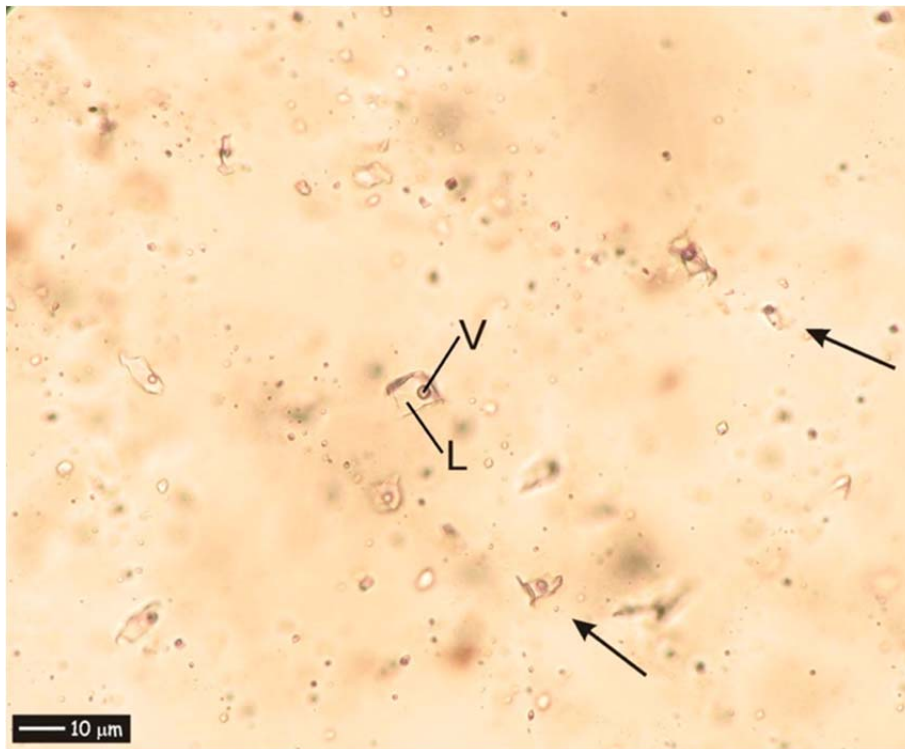
Figure 16: Photomicrograph showing numerous two-phase (liquid + vapour) brine fluid inclusions hosted within quartz from the Union Jack occurrence of the Iron Range IOCG mineralization. Arrows indicate a fluid inclusion assemblage, displaying consistent phase ratios trapped along healed fractures (after Staples et al., 2008). L: Liquid, V: Vapour.

5.2 Chlorite Thermometry

Partitioning of various elements between chlorite and iron-magnesian host rocks is the basis for the chlorite thermometry that may not be well constrained thermodynamically. Nonetheless, Cathelineau et al. (1985) and various other authors however have empirically calibrated chlorite thermometers.

In 2008, Staples et al. analyzed ankerite and chlorite in textural equilibrium with blades of hematite , which were used for chlorite thermometry and yielded temperatures in the range 275-325 °C based on the tetrahedral Al site occupancies

5.3 Stable Isotope Study

Samples of coexisting quartz-magnetite or albite-magnetite were chosen for stable isotope analyses to estimate precipitation temperatures. In the field as well as in a number of thin sections, these minerals were observed to be in textural equilibrium (Figure 17). The selected vein samples containing the minerals of interest were crushed and sieved to separate mineral grains ranging from 125 to 200 microns. The samples were then rinsed with distilled water and acetone. The samples were washed in a 10 percent HCl to remove any carbonates. The purity of all samples was confirmed using a scanning electron microscope equipped with an energy dispersive X-ray detector. The oxygen was extracted from quartz, albite and magnetite separates using the BrF_5 technique

of Clayton and Mayeda (1963). The isotopic data were measured using a Finnigan MAT 252 mass spectrometer at Queen's University and are reported (Table 1) in per mil relative to Vienna standard mean ocean water (‰V-SMOW).

Albite-magnetite pair equilibrium temperatures were calculated using the calibrations of Cole et al. (2004) and O'Neil and Taylor (1967) whereas quartz-magnetite equilibrium temperatures were calculated using the equations in Zheng and Simon (1991). The three samples are somewhat concordant and yield temperatures in the range 340 to 400 °C.

Although the petrography relating the fluids and the vein mineral assemblages is not unambiguous, the fluid inclusion data have been combined with the stable isotope temperatures to place some approximate constraints on the pressure and temperatures of formation for the veins. Petrographically the veins are the result of multi-episodic fault dilation, alteration and fluid influx. By combining both fluid constraints with the both the albite-magnetite and quartz-magnetite isotope thermometry provides temperature estimates of 340 to 400 ° and corresponding pressures ranging from 1750 to 4500 bars (Figure 18.). The temperatures derived from stable isotopes and fluid inclusions are higher than the ones reported in Chapter 5.2 derived from chlorite thermometry. However, the temperatures derived from stable isotopes and fluid inclusions are the much better calibrated and thermodynamically constrained and thus the preferred ones.

Sample	Mineral	$\delta^{18}O_{VSMOW}$ (‰)	$\Delta qtz_{silicate\text{-}magnetite}$ (‰)	Temperature (°C)
IR07-02L1	albite	10.6		
IR07-02L1	magnetite	-2.1	12.7	346
IR07-13	quartz	11.1		
IR07-13	magnetite	0.5	10.6	398
IR07-17B	albite	5.7		
IR07-17B	magnetite	-6.5	12.2	364

Table 1: Oxygen stable isotope equilibrium temperatures for albite-magnetite and quartz-magnetite pairs.
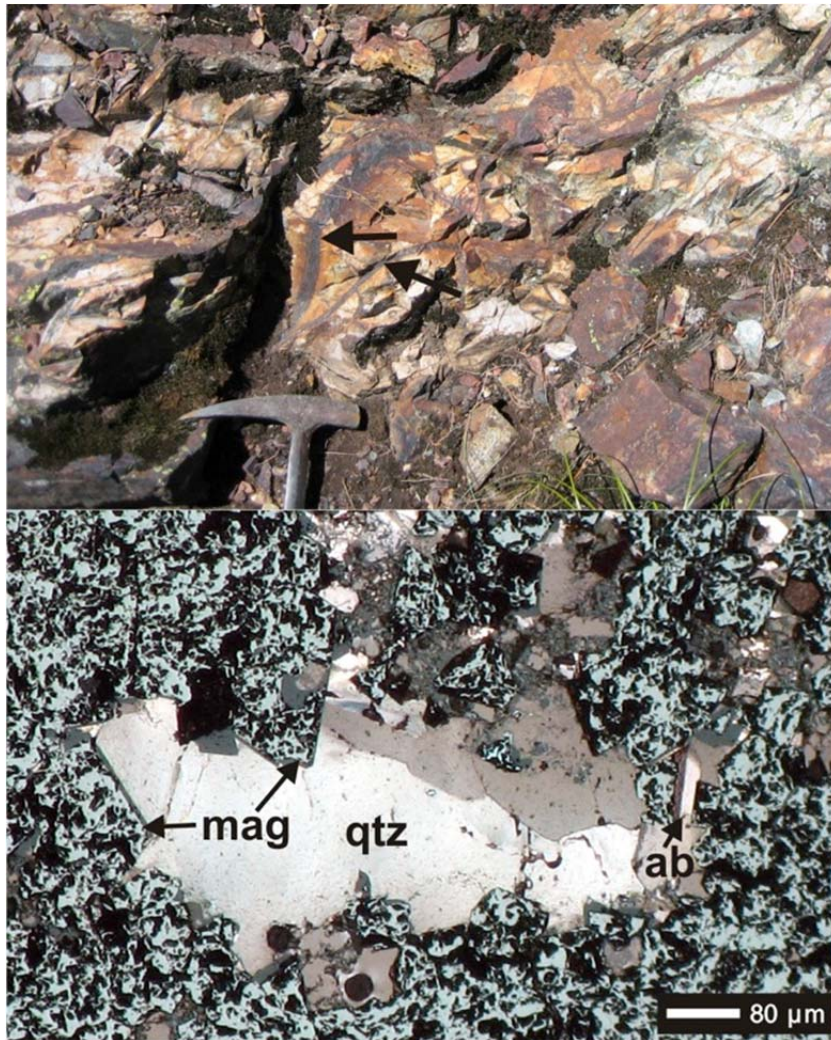
Figure 17: Iron-oxide veined and albite altered outcrop (upper photo). The lower photomicrograph shows coexisting quartz (qtz)-magnetite (mag) and albite (ab)-magnetite sampled from outcrop veins. Photomicrograph taken in simultaneous transmitted and reflected light.
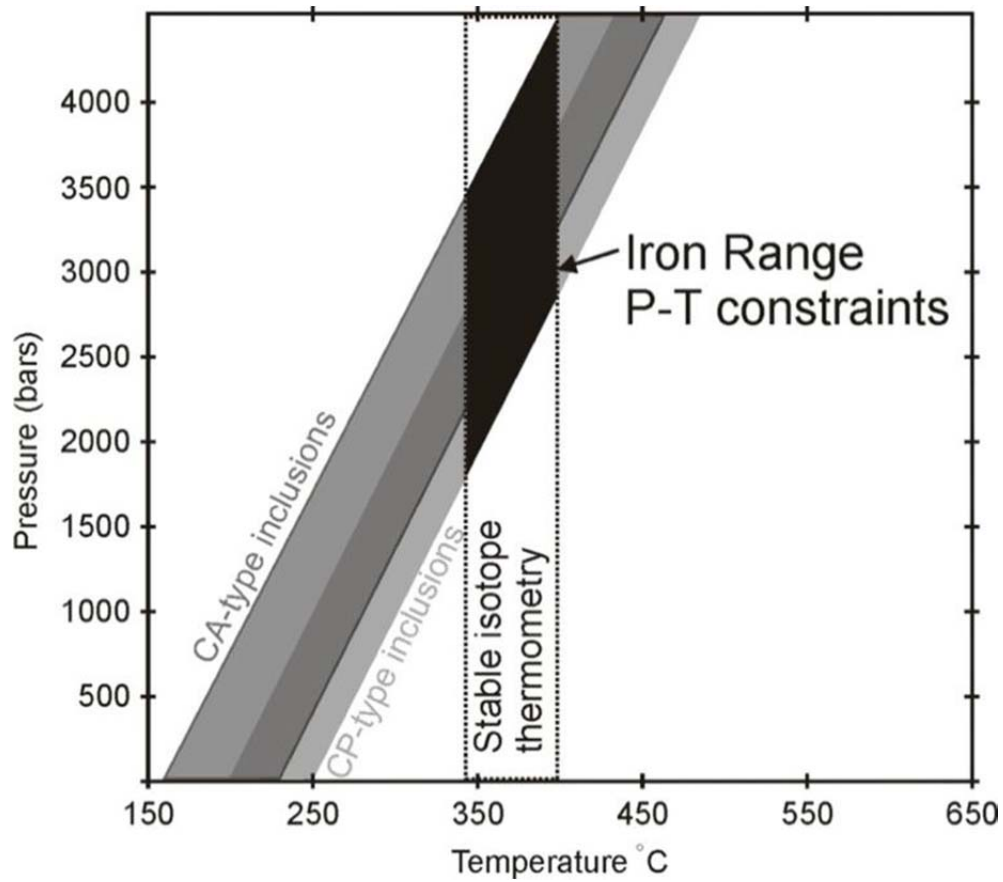
Figure 18: Iron Range P-T conditions for iron-oxide precipitation (black trapezoid) based on fluid inclusion isochores for the CA-type fluid inclusions (dark grey) and CP-type fluid inclusions (light grey) and stable isotope thermometry

6: GEOCHRONOLOGY

The simple mineralogy of the iron-oxide mineralization lacks appropriate minerals for most geological dating techniques (i.e., Ar-Ar or U/Pb), however it is a perfect candidate for paleomagnetic dating due to abundant minerals (magnetite and hematite) that can record the magnetic field during (re-) crystallization. Paleomagnetic dating is a controversial dating technique as the structural and tectonic history is often not completely understood or known. Nonetheless, it has been used successfully to date Proterozoic banded iron formations in Australia (Schmidt and Clark, 1994). It is best to use paleomagnetic data in conjunction with other geological data to enhance its validity. Although Ar-Ar dating was not applicable to the vein assemblages it has been conducted on intrusions at and near the Iron Range. These intrusions include carbonatites which occur on top of the Iron Range Mountain, the nearby Mount Skelly pluton, and Sanca stock (Logan, 2002) and a suite of regional plutons spatially associated with iron-oxide breccia and magnetite phenocrysts. All collected samples of felsic intrusive rocks are believed to belong to the Cretaceous Bayonne Magmatic Suite.

6.1 Ar-Ar Dating

Table 2 lists the sample locations and descriptions, as well as the Ar-Ar age for collected samples during fieldwork in 2008. The $^{40}Ar/^{39}Ar$ laser technique

Analyses were performed at the Geological Survey of Canada laboratories in
Ottawa.

Sample	Location notes	Rock	Mineral	Ar-Ar age (Ma)
MG08-01	Hellroaring Creek	Leeder Stock granite	biotite	104.8 +/- 1.1
MG08-9b	Iron Range	Carbonatite	phlogopite	311 +/- 12
MG08-10a	Angus Creek	Unnamed granite	biotite	106.7 +/- 1.1
MG08-10b	Angus Creek	Unnamed granite	muscovite	108.0 +/- 1.2
MG08-12	Ailsa Lake	Aisla Lake granite	biotite	78.5 +/- 0.8
MG08-22	Iron Range	Carbonatite	phlogopite	291 +/- 16
MG08-28	Mount Skelly	Mt. Skelly granodiorite	biotite	89.7 +/- 0.9

Table 2: Ar-Ar ages of various rocks from the Belt-Purcell (see Appendix 2 for the analytical data).

Archibald et al. (1984) reported a 97.1-98.7 Ma K-Ar age for the Mount
Skelly Pluton (Figure 1), and a 78.9-80.9 Ma K-Ar date for the Sanca Stock which
intrudes the Mount Skelly Pluton; both intrusive phases belong to the Bayonne
Magmatic Suite (Logan 2000, 2002). Sample MG08-28 taken from the Mount
Skelly Pluton is a granodiorite containing up to 10% unaltered biotite. The biotite
defines a plateau and yields an apparent age of 89.7+/-0.9 Ma (Figure 19), which
is not consistent with the K-Ar ages reported by Archibald et al. (1984) or Logan
(2002). This Ar-Ar age might indicate an unknown third intrusive phase of the
Bayonne Magmatic Suite in that area, but probably represents the best estimate
of age because the Ar-Ar dating method is more robust than the more easily
reset K-Ar method.
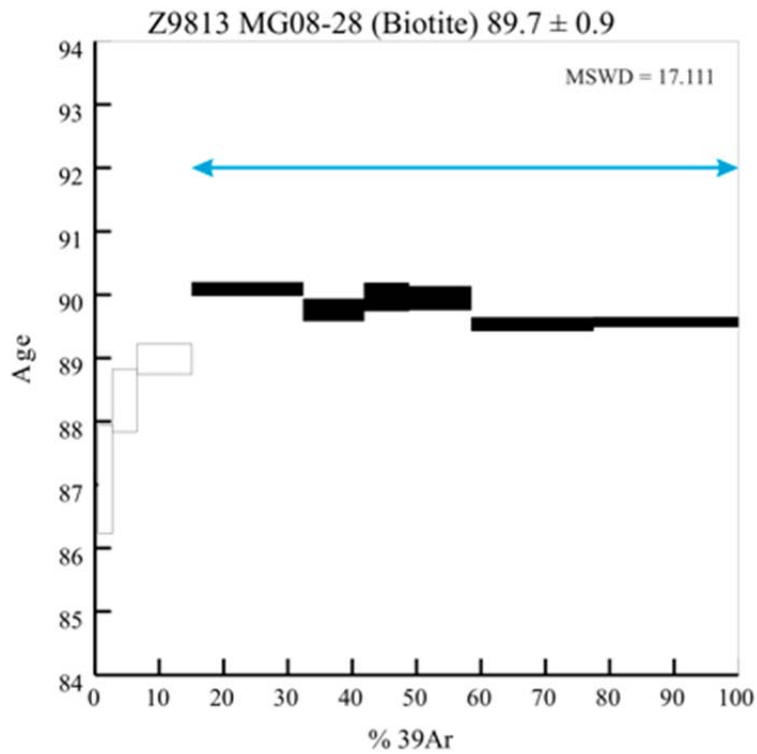
Figure 19: Plateau age of biotite from the Mount Skelly granodiorite; Arrows show the range of steps used in the weighted mean age calculation.

The previously undated Leeder Stock (Figure 1) is also part of the Cretaceous Bayonne Magmatic Suite. It is a biotite-granite locally containing up 10% percent euhedral magnetite crystals in cumulate layers as well as magnetite veinlets. Sample MG08-01 contained 5% unaltered biotite, which defines a plateau and yields an apparent age of 104.8 +/- 1.1 Ma (Figure 20).
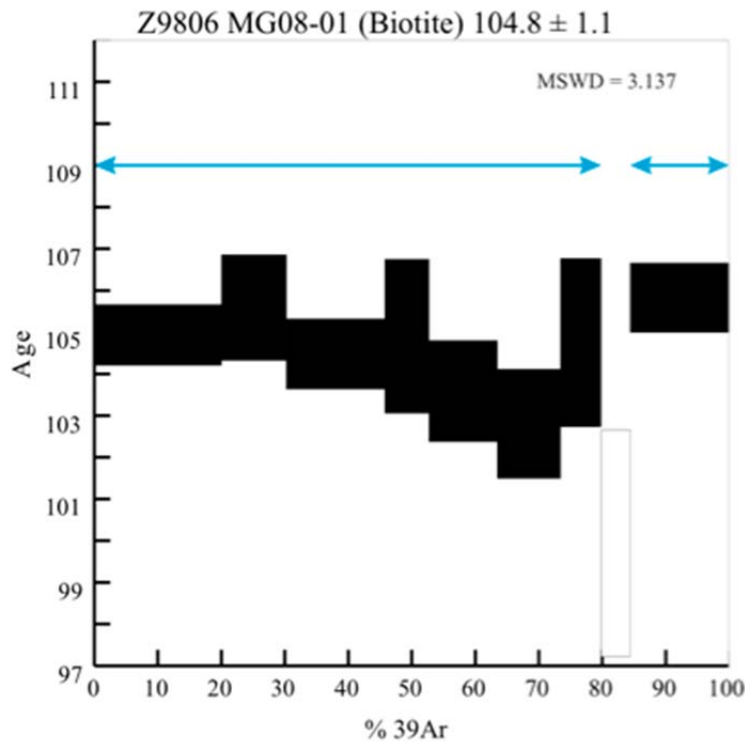
Figure 20: Plateau age of biotite from the Leeder Stock; Arrows show the range of steps used in the weighted mean age calculation.

A series of previously undated and partly unnamed intrusions with locally associated iron-oxide breccias and veins have been collected and included in the analysis. Biotite and muscovite (sample MG08-10a and 10b, respectively) from a granitic pluton 20 km east of the City of Kimberly, BC near Angus Creek form plateaus and yield apparent ages of 106.7 +/- 1.1Ma and 108.0 +/- 1.2 Ma, respectively (Figure 21). Biotite from a granitic pluton (sample MG08-12) 15 km south of the Leeder Stock near Ailsa Lake defines a plateau and has an apparent age of 78.5 +/- 0.8 Ma (Figure 22), similar in age to the Sanca Stock (Archibald, 1984).
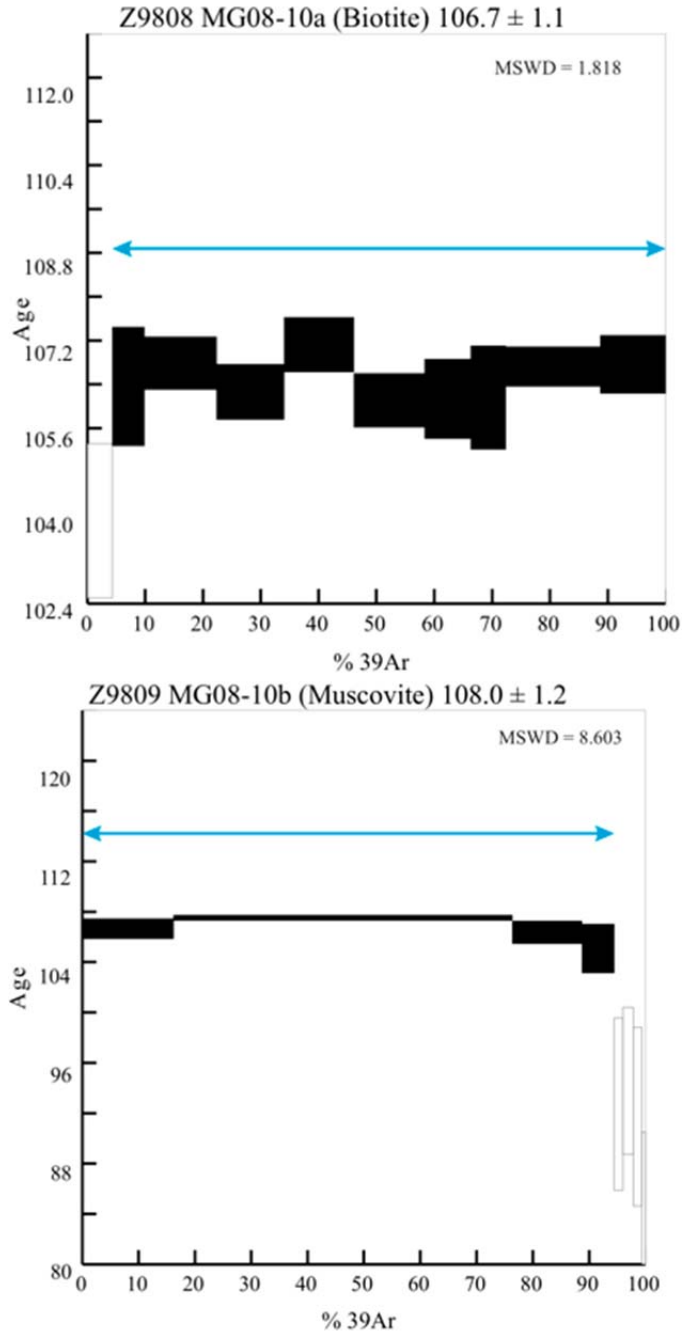
Figure 21: Plateau ages of biotite (left) and muscovite (right) from the Angus Creek granite; Arrows show the range of steps used in the weighted mean age calculation.
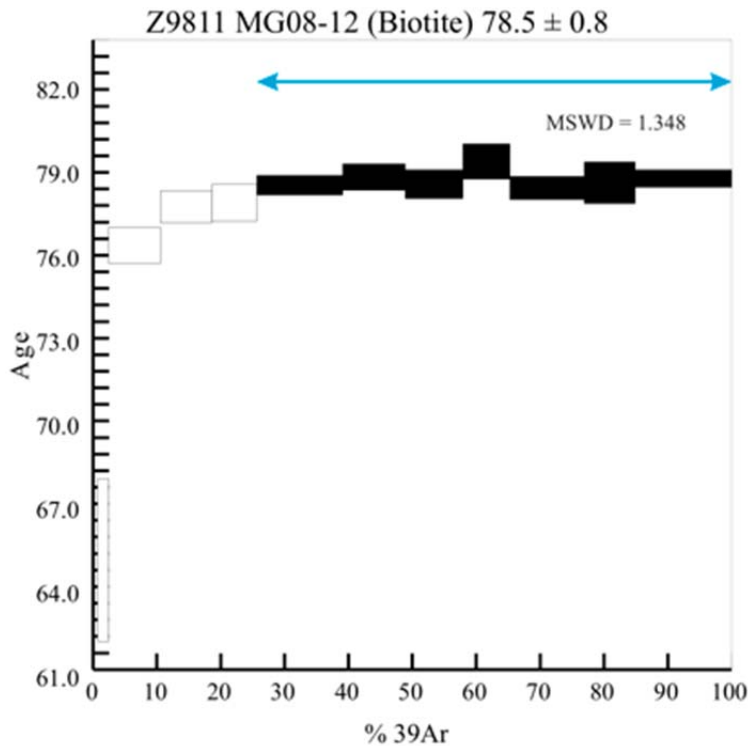
Figure 22: Plateau age of biotite from the Ailsa Lake granite; Arrows show the range of steps used in the weighted mean age calculation.

Outcropping carbonatites at the Iron Range contain characteristic dark purple phlogopite. The carbonates are texturally and petrographically similar to the Goat River carbonatites described in Walker (1998). Phlogopite from two Iron Range carbonatites (MG08-22 and MG08-9b) failed to define a plateau and have high apparent spectral ages from the analysis. Inverse isochron plots can provide a better estimate for these phlogopite samples as plots make no assumption about the trapped argon component and yield ages of 291+/-16 Ma and 311+/-12 Ma respectively (Figure 23). These Ar-Ar ages are somewhat consistent with a

Pennsylvanian age (301+/-10 Ma) reported for a carbonatite in the Goat River

area (Walker, 1998).
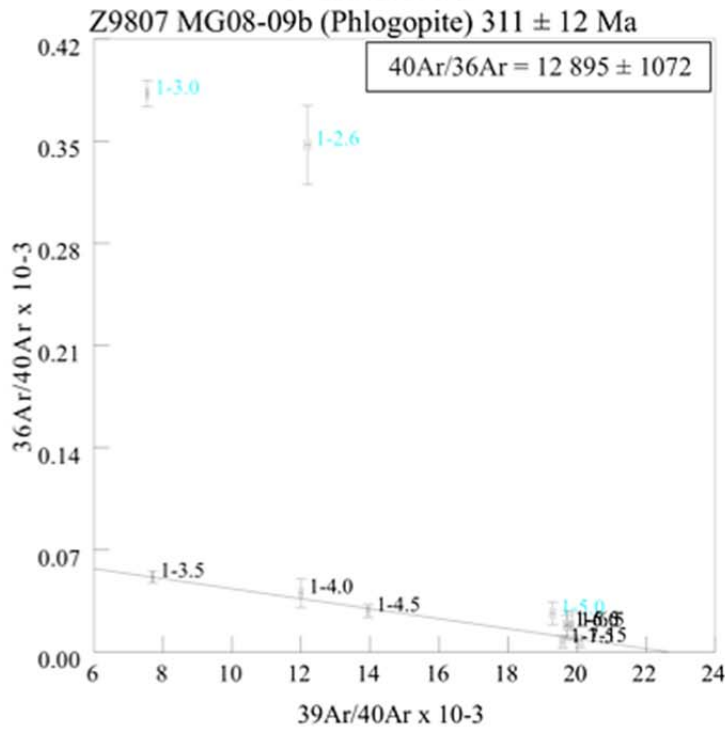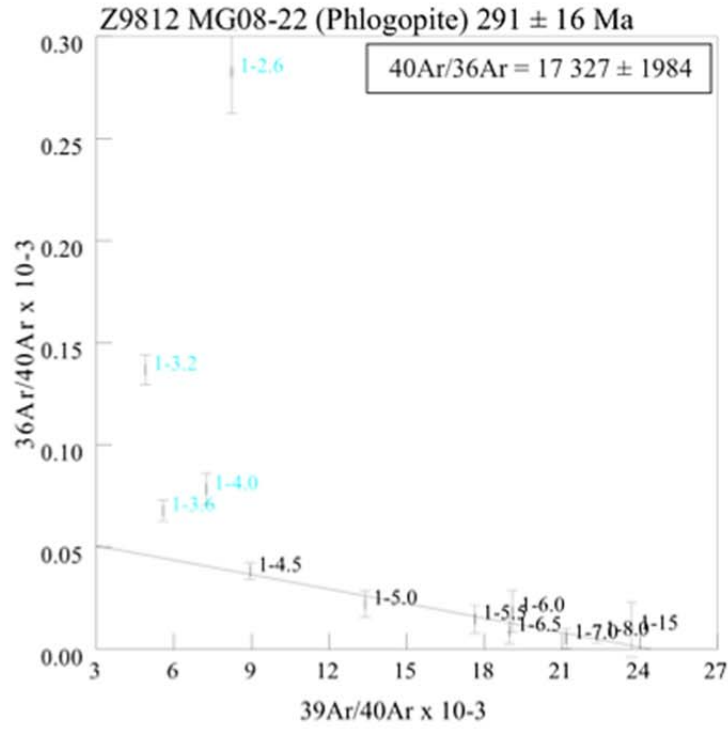
Figure 23: Inverse Ar-Ar isochron plots from two phlogopite samples from Iron Range carbonatites.

55

6.2 Paleomagnetic Dating

Approximately 100 samples from 14 locations along the Iron Range fault have been used for this paleomagnetic investigation including 8 massive and brecciated iron-oxides, Middle Aldridge strata, Moyie Sills and carbonatite. The samples are drill-core samples that were orientated at each site using both a magnetic and when possible a solar compass; bearings from magnetic and solar measurements agreed on average within 3%. The main goal was to isolate the primary characteristic natural remanent magnetization (NRM) by selective removal of secondary NRM. The two methods used for destruction of low stability, secondary NRM weere alternating field (AF) and thermal (T) demagnetization. The analyses were performed at the GSC Pacific Centre in Saanich, BC under supervision of Dr. Randy Enkin. Samples for AF demagnetization were subjected to an alternating field ranging from 5 - 99 mT using a Schonstedt GSD-5 alternating field demagnetizer with tumbler; samples chosen for T demagnetizing were heated from 150 - 675 °C in a Schonstedt TSD-1 thermal demagnetizer. Prior to each demagnetizing step, the samples were measured using a Geofyzika JR5A spinner magnetometer to record conductivity and magnetic susceptibility. In many cases, where 2 samples were obtained from 1 core sample, thermal and alternating field demagnetization was conducted on the same core.

Paleomagnetic data obtained from the Middle Aldridge, Moyie Sills and carbonatite did not yield any conclusive results. The quality of the resulting data for the iron-oxides is very good as almost all samples demagnetized properly,

however the high stability component of many of the sites differ and some sites show great scatter. Principal component analysis was used to determine an average vector for each site for which a 95% confidence interval was calculated. Figure 24 illustrates the average polar direction for latitude and longitude similar to the one of the Iron Range in green over the last 1500 million years; note the break between 950 and 510 Ma due to a well-known lack of consistent data. Black squares indicate the average vectors for sites with a 95% ≤ 15 confidence interval which is represented by the black circles (corresponding to the central black squares; better constrained vectors have smaller circle radii).

The paleomagnetic data are consistent with magnetization acquired during the Cretaceous before stratigraphic tilting (regional 30° tilt). One of the sample sites also recorded a true magnetic reversal with 2 samples from the same core having reversed directions. The average age of a reversal is 10,000 years. However, they can occur within a few thousand years as well (Clement, 2004). Thus 2 generations of paramagnetic grains precipitated most likely within a few thousand years. This is consistent with petrographic observations where multiple generations of iron-oxides minerals have been observed.

Using paleomagnetism as a dating technique on iron-deposits is very challenging. Massive iron-deposits where multiple precipitation events are recorded will behave different from weakly magnetized sandstones or basalts, which are the most common lithologies for paleomagnetic dating. The 1st generation of paramagnetic grains will align itself in the orientation of the ambient field, whereas the 2nd generation will align itself in an orientation that is a

combination of the ambient field and the magnetic field created by the first generation. This accounts for the great scatter of samples in some of the sites, and accounts for scatter of most sites with respect to each other. Despite the scatter, there is some coherence in the sites as evidenced by a migration of all data ((high-stability components) towards a major Cretaceous magnetization event with increasing removal of the secondary NRM.
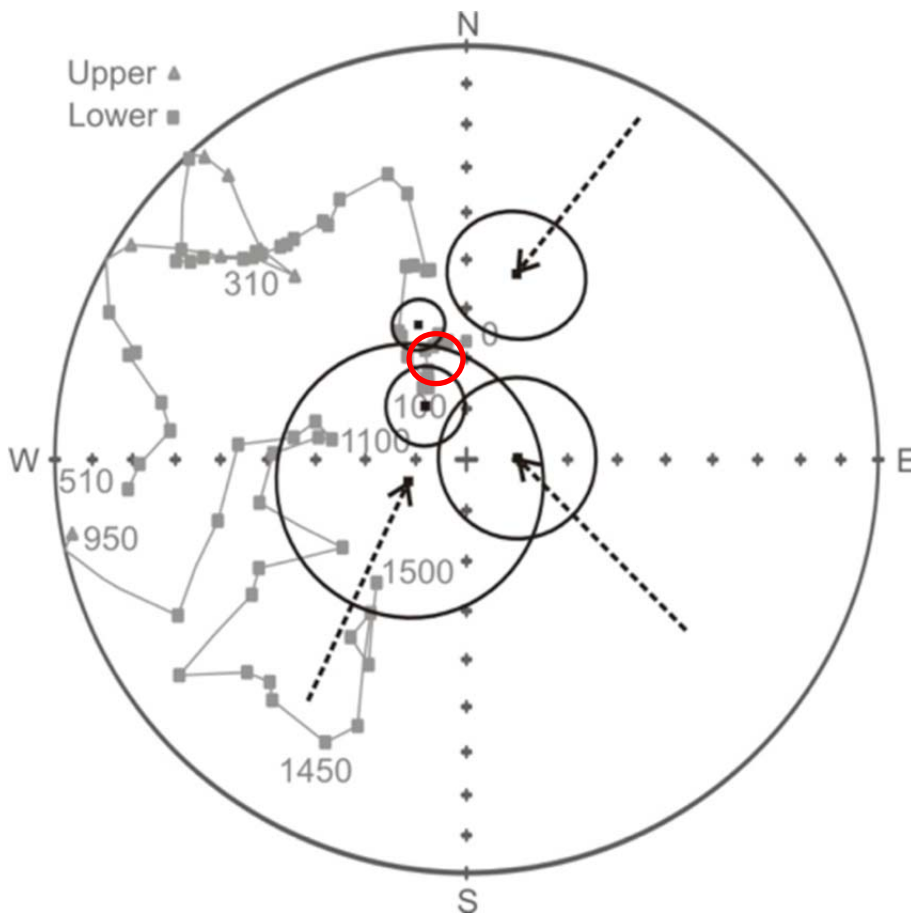
Figure 24: Apparent polar wander path (grey) with magnetic poles for individual Iron Range iron-oxide occurrences shown as black circles (the bigger the radius the larger is the 95% confidence interval (max 15); dashed arrows indicate direction to which individual iron-oxide occurrences weere trending with continued demagnetization); in red is the paleomagnetic data for the Mount Skelly (Irving and Archibald, 1998).

6.3 Summary

In summary, Ar-Ar dating confirmed that all sampled felsic intrusions in the regional district spatially associated with iron-oxide breccia or containing magnetite phenocrysts yield ages consistent with the Cretaceous Bayonne Magmatic Suite. Granodiorite found at Mount Skelly belongs to the same plutonic suite, however Ar-Ar dating revealed a third, unknown intrusive phase of this pluton dated at 89.7 +/- 0.9 Ma (with respect to 97.1-98.7 Ma and 78.9-80.9 Ma reported by Archibald et al. (1984).

Paleomagnetic data from the Iron Range indicates a hydrothermal event in Cretaceous time that led to most of the iron-oxide (re-) crystallization. This mineralization age is consistent with a possible Cretaceous heat and metal-source, as indicated by the regional Ar-Ar dated felsic intrusions associated with iron-oxide breccia or containing magnetite phenocrysts. Irving and Archibald (1990) conducted a paleomagnetic study on the Mount Skelly Pluton and their Cretaceous paleomagentic age for the intrusion is consistent with a Cretaceous paleomagnetic age for the Iron Range (paleomagnetic data for the Mount Skelly from Irving and Archibald (1990) is plotted as a red circle on Figure 24).

7: MAGNETITE MINERALOGY

Magnetite is a common (accessory) mineral found in many ore deposits, not only in iron-bearing deposits like IOCGs or BIFs. It can incorporate many cations other than iron into its crystal-structure. Magnetite belongs to the spinel group that crystallizes in the isometric crystal system. The general formula for the spinel group is XY_2O_4 and its structure is based on cubic close-packed oxygen with 8 X and 16 Y cations in tetrahedral and octahedral coordination, respectively. The X cations are all divalent, whereas the Y cations can be either all trivalent or half quadrivalent and half divalent.

There are two types of spinel structures based on particular cations in specific sites. The more common spinel structure is displayed by the spinel (Al^{3+}) and the chromite (Cr^{3+}) series where the divalent cation is in tetrahedral coordination and the trivalent cation (Al^{3+}, Cr^{3+}) in octahedral coordination. The magnetite series has an inverse spinel structure, which is an alternative arrangement where half of the trivalent cations are switched with the divalent cations, i.e., 8 Fe^{2+} (X cations) in octrahedral coordination and 16 Fe^{3+} (Y cations) are equally distributed between tetrahedral and octahedral coordinations. All spinel group series show a wide range of chemical compositions due to solid-substitutions of divalent and trivalent cations (Deer et al. 1997).

7.1 Electron Microprobe Analyses of Magnetite

7.1.1 Samples and Analytical Method

The magnetite for this study comes from: (I) (barren) iron-oxide massive veins and breccias, (II) iron-oxide massive veins spatially associated with gold, (III) brecciated massive iron-oxides associated with chalcopyrite, (IV) gabbroic sills with postgenetic magnetite within the IRFZ, and (V) Leeder stock near Hellroaring Creek.

Analysis of magnetite was carried out at the UBC Dept. of Earth and Ocean Science laboratory, utilizing a fully-automated Cameca SX-50 Scanning Electron Microprobe with 4 vertical wavelength-dispersion X-ray spectrometers and a fully-integrated SAMx energy-dispersion X-ray spectrometer. Compared to other analytical methods (i.e., ICPMS), the electron microprobe is a relatively fast and inexpensive way to acquire chemical compositions of minerals. The analyses were done with the following operating conditions: excitation voltage, 20 kV; beam current, 40 nA; peak count time, 80 s (20 s for Fe); background count-time, 40 s (10 s for Fe); spot diameter, 1 μm. Data reduction was done using the 'PAP' $\varphi(\rho Z)$ method (Pouchou and Pichoir, 1985). For the elements considered, the following standards, X-ray lines and crystals were used: gahnite, AlK $_\alpha$, TAP; synthetic magnesiochromite, MgK $_\alpha$, TAP; synthetic rhodonite, SiK $_\alpha$, TAP; diopside, CaK $_\alpha$, PET; rutile, TiK $_\alpha$, PET; V element, VK $_\alpha$, PET (corrected for TiK $_\beta$); synthetic magnesiochromite, CrK $_\alpha$, LIF; synthetic rhodonite, MnK $_\alpha$, LIF; synthetic hematite, FeK $_\alpha$, LIF; Co element, CoK $_\alpha$, LIF; synthetic Ni_2SiO_4, NiK $_\alpha$, LIF; Cu element, CuK $_\alpha$, LIF; gahnite, ZnK $_\alpha$, LIF.

Chemical analysis was then further processed statistically following the procedures by Helsel (2005) for computing descriptive statistics, hypothesis tests, correlation and regression for left-censored (nondetect) data. This step was necessary to address analyses that resulted in element concentrations below detection limit of the electron microprobe.

7.1.2 Results and Discussion

Statistically processed results of the electron microprobe analysis are shown in table 3. Although some elements like Mn, Ca, Cu, Cr, Ni and Ti have concentrations below detection limit, it is usable data as it constrains those element concentrations to a hypothetical maximum. The electron microprobe analysis yielded many values below the detection limit of the instrument. Using only data above detection limit introduces bias into the dataset because values below the sensitivity of the instrument are not considered. Samples below detection limit have a concentration of the element of interest, which is simply not measurable with the instrument. Considering only values above detection limit, the average will be higher than the mean composition of the material. In order to estimate the mean of a set of samples, it is optimal to consider all measurements whether above of below detection limit as described in Helsel (2005).

sample	Si	Ti	Al	Cr	Fe	Mn	Mg	V	Ni	Cu	Ca	V
MG08-53-1a	0.0327	0.0177	0.0119	0.0268	93.0626	<DL	0.0083	0.0801	<DL	0.0362	<DL	0.0801
MG08-53-1b	0.0548	<DL	0.0111	<DL	92.7525	<DL	0.0095	0.0747	<DL	0.1208	<DL	0.0747
MG09-01-1a	0.1323	<DL	0.0174	<DL	92.1200	<DL	<DL	0.1662	<DL	<DL	<DL	0.1662
MG09-01-2a	0.0821	<DL	0.0178	<DL	92.4964	<DL	<DL	0.1426	<DL	<DL	<DL	0.1426
MG09-01-2b	0.0880	<DL	0.0166	<DL	92.5874	<DL	0.0067	0.1374	<DL	<DL	<DL	0.1374
MG09-01-2c	0.1082	<DL	0.0217	<DL	92.5918	<DL	0.0118	0.1317	<DL	<DL	<DL	0.1317
MG08-01-1b	0.0247	0.0164	0.1317	<DL	92.0187	0.5095	0.0118	0.4948	<DL	<DL	<DL	0.4948
MG08-21-1a	0.0625	<DL	0.0106	<DL	92.3611	<DL	0.0106	0.0841	<DL	<DL	<DL	0.0841
MG08-21-1b	0.0724	<DL	0.0097	<DL	92.5494	<DL	0.0073	0.0997	<DL	<DL	0.0076	0.0997
MG08-21-1c	0.1597	<DL	<DL	<DL	92.3736	<DL	0.0079	0.0843	<DL	<DL	0.0066	0.0843
MG08-42-1a	0.0271	0.0413	0.0249	<DL	92.3137	<DL	0.0115	0.1832	0.0235	<DL	0.0107	0.1832
MG08-42-1b	0.0262	0.0165	0.0103	<DL	92.3130	<DL	0.0108	0.2020	<DL	<DL	<DL	0.2020
MG08-42-1c	0.0485	0.0234	0.0202	<DL	92.7711	<DL	0.0109	0.2180	<DL	<DL	<DL	0.2180

Table 3: Electron microprobe analyses of magnetite from the Iron Range and Hellroaring Creek. Each sample represents the mean of individual magnetite grains, standard deviations for all measurements and detection limits are provided in Appendix 4. Element concentrations are given in weight percent (%). '<DL' indicates concentrations below detection limit. Magnetite in sample MG08-53-1a,b is from the copper-bearing brecciated iron-oxide zone. Magnetite in sample MG09-01-1a and 2a,b,c is from the gold-bearing massive iron-oxide zone. Magnetite in sampe, MG08-01-1b is from the Leeder stock (Hellroaring Creek). Magnetite in sample MG08-21-1a,b,c is from the (barren) massive and brecciated iron-oxide zone. Magnetite in sample MG08-42-1a and b are from the gabbroic Moyie Sill.

Beaudoin and Dupuis (2009) have analyzed minor and trace elements in magnetite and hematite from a range of mineral deposit types (IOCG, Kiruna, BIF, Cu-Mo-Au porphyry, Fe-Cu skarn, Fe-Ti, V, Cr, Ni-Cu-PGE, Cu-Zn-Pb VMS and Opemiska-type veins) and their study shows compositional differences in the iron-oxides that fingerprint specific mineral deposit types. Elemental compositional differences were used to construct discriminant diagrams that separate different mineral deposit types (e.g., Ni/(Cr+Mn) vs. Ti+V). Fields separating different mineral deposit types in these diagrams are based on a limited amount of data-points, however all data points form somewhat definite clusters (Figure 25).

In figure 24 the Iron Range magnetite is plotted on the Ni/(Cr+Mn) vs. Ti+V diagram and shows that magnetite from the Iron Range is consistent with Ti+V ratios in IOCG and porphyry deposits. Ni, Cr and Mn concentration were below detection limit for most samples. In that case half the detection limit was chosen for the element concentration. Choosing element concentration of 0 or the detection limit itself for these values did not change the position significantly (e.g., samples shifted down into the skarn field or shifted further up into the IOCG field. It is evident that magnetite from the Iron Range is very similar in composition (i.e., Ti+V) to magnetite from a range of IOCG occurences. On a similar note, IOCG deposits have low-Ti contents in magnetite, which is generally below 0.5 wt.% Ti and rarely above 2 wt.% Ti (Hitzman et al. 1992). Magnetite from the Iron Range has very low Ti-concentrations with a maximum of 0.04 wt.%, which is another characteristic that the Iron Range shares with various IOCG deposits (Hitzman 2000, Williams et al. 2005, and Barton and Johnson 2004). Magnetite samples from massive iron-oxides associated with gold mineralization can be distinguished from all other magnetite samples based on their higher Ti+V content, which plots these samples close to or inside the porphyry field. The original (Beaudoin et al., 2010) data used to base the different mineral deposit type fields on shows that the boundary between IOCG and porphyry is not well defined (e.g., very few data points, Figure 25). Most Iron Range samples fall within an area that is between data points that have been used to construct these diagrams (Figure 25). Therefore the magnetite from the

Iron Range shows a characteristic trace element signature that ranges between

IOCG and porphyry deposits.
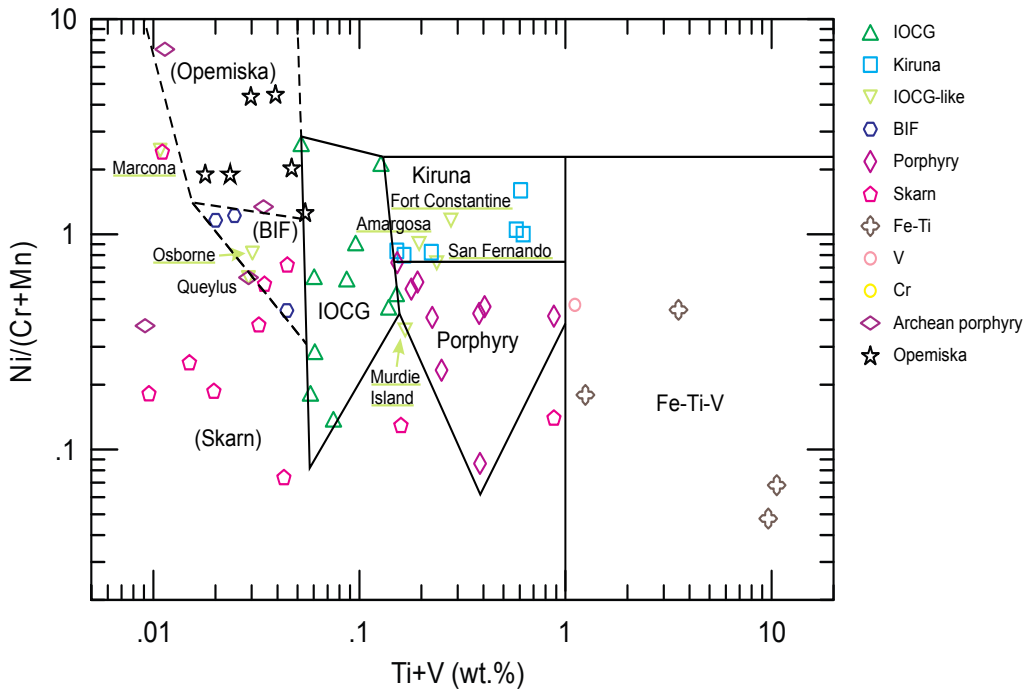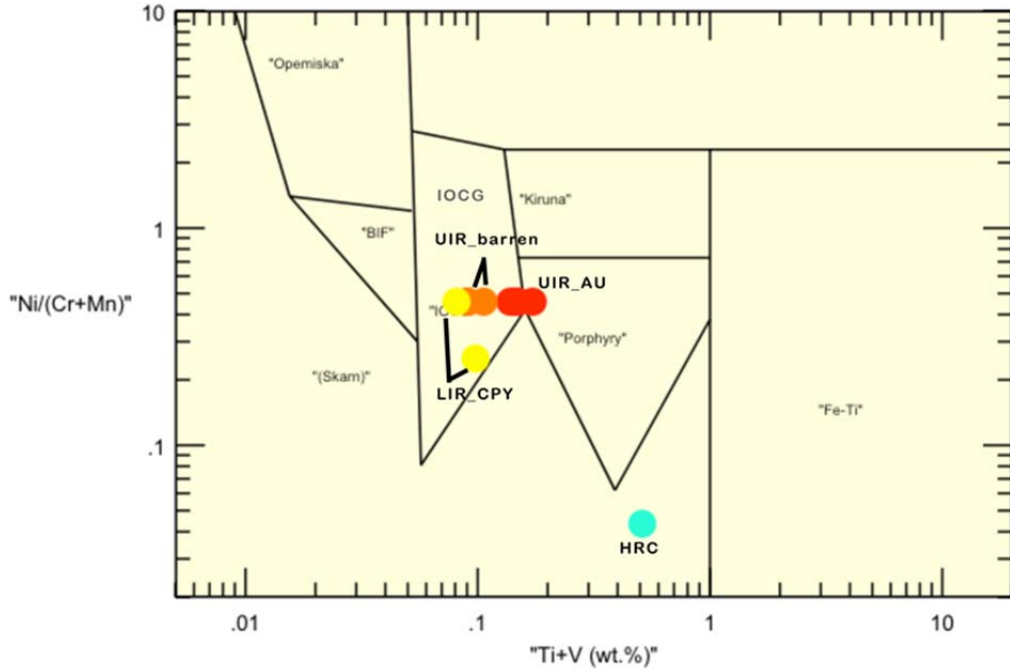
Figure 25: Magnetite trace element ratios from the Iron Range and Leeder stock (upper diagram) with respect to deposit type (UIR_AU = magnetite found Au-enriched zones, UIR_barrren= magnetite from iron-oxide only zones, LIR_CPY= magnetite from Cu-enriched zones, HRC= Leeder stock). The lower diagram shows the magnetite trace element ratios from various deposits used byBeaudoin and Dupuis (2009).

Magnetite trace element concentrations were also compared with respect to the gold-bearing iron-oxide zone, the copper-bearing iron-oxide zone, barren iron-oxides and the Moyie Sills (Figure 26). It is interesting to note how the iron-oxide zone and Moyie Sills can be depicted by their V, Fe, Si and Al concentrations. Magnetite associated with the gold-bearing iron-oxide zone is enriched in Si and Al, which is not surprising considering gold in that zone is hosted within weakly developed quartz-stockwork). Si^{4+} can substitute Fe^{3+} in tetrahedral coordination in the magnetite crystal structure only if additional Fe^{3+} is reduced to Fe^{2+} or vacancies in the crystal lattice are created in order to maintain charge balance (Westendorp et al. 1991). Petrographic evidence of changing f-O_2 (e.g., hematite replacing magnetite to form martite and magnetite overgrowing hematite) could enhance Si^{4+} substitution for Fe^{3+} in tetrahedral coordination as additional Fe^{3+} is reduced to Fe^{2+}. Vanadium is most enriched in the Moyie Sills relative to the barren iron-oxide zone and the copper-bearing iron-oxide zone; the gold-bearing iron-oxide zone shows slight enrichment in vanadium as well. This enrichment is difficult to explain as vanadium is a very immobile element and in its most mobile state V^{5+} its incorporation into the magnetite crystal structure is complicated because it would require coupled substitution with a more weakly charged cation to maintain charge balance.
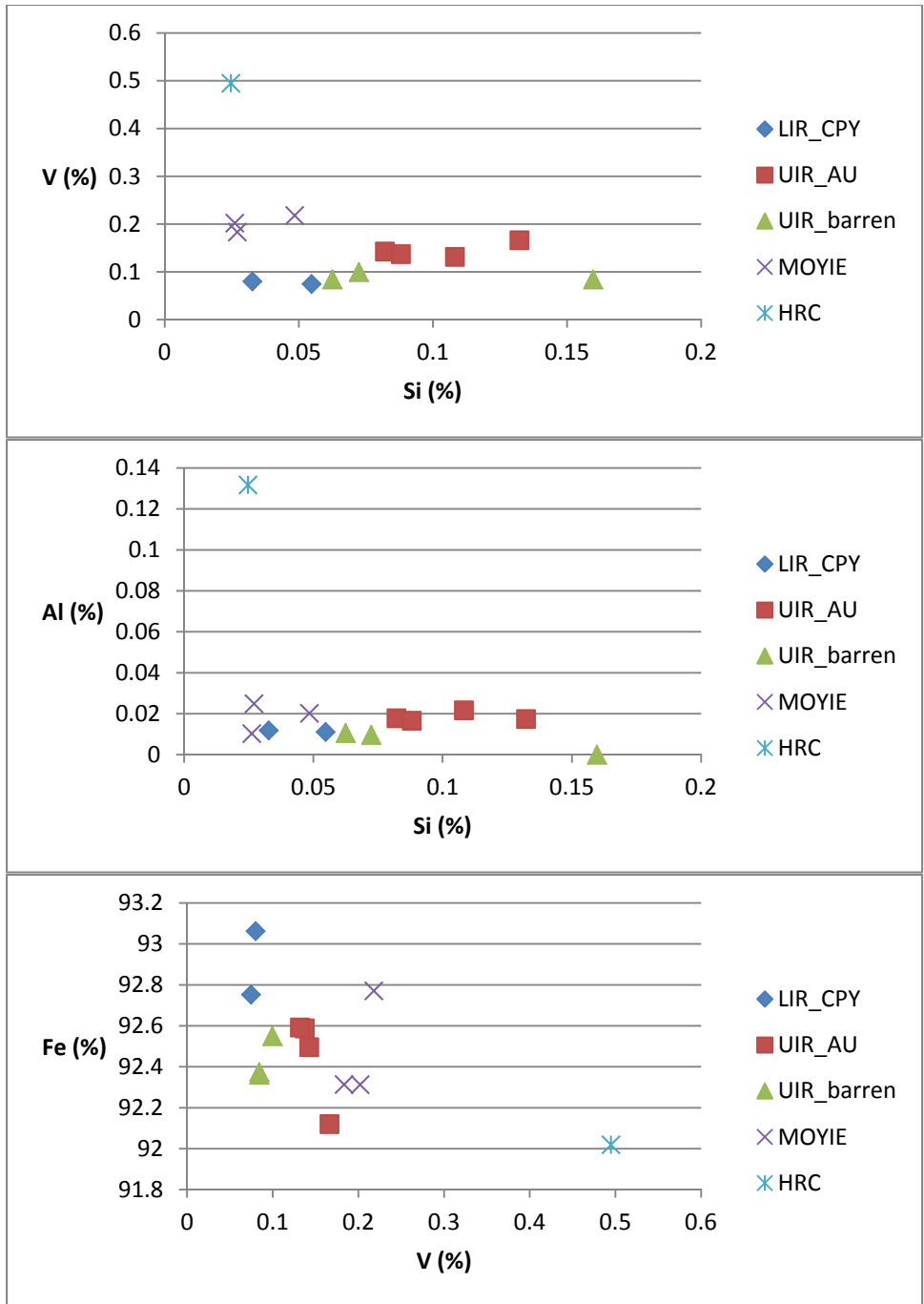
Figure 26: Magnetite trace element concentrations of UIR_AU = magnetite found Au-enriched zones, UIR_barrren= magnetite from iron-oxide only zones, LIR_CPY= magnetite from Cu-enriched zones, MOYIE= Moyie sills, and HRC= Leeder Stock

8: PARAGENESIS, REGIONAL CONTEXT AND EVOLUTION OF THE IRON RANGE MINERALIZATION

8.1 Paragenesis

Petrographic observations of thin sections and hand specimen (Chapter 2.1) were used to derive timing relationships between the iron-oxide occurrences, base metal mineralization, alteration and brecciation, and are shown in Table 3.

Early stage albite and quartz precipitate along the IRFZ along with albite alteration of the surrounding country rock (stage I.) followed by brecciation and multiple episodes of iron oxide precipitation (stage II.). This conclusion is derived from the observation of anhedral and/or broken grains of albite and quartz, which are rimmed or cut by iron-oxides and occur as fragments within the iron-oxide dominated matrix of the iron-oxide breccia. Stage II likely represents more than just one cycle of brecciation and iron oxide precipitation. This conclusion is supported by petrographic observations of hematite replacing magnetite and vice versa, indicating that this stage (II) was repeated multiple times. The previously discussed paleomagnetic study (Chapter 6.2) supports protracted Iron Range mineralization involving multiple hydrothermal events. Pyrite occurred throughout most of the hydrothermal event(s) and is commonly present within iron-oxide grains. The Cu-mineralization at depth is consistent with chalcopyrite occurring as a late stage mineral having irregular, non-brecciated orgrains which likely grew interstitially together with pyrite. Au-mineralization occurred late in the

paragenesis within late stage quartz-veins, which are abundant at the Iron Range. Locally, where most of the Au-mineralization occurred, quartz-veining is strong forming weak stockwork-like textures.

	Time →	
	Stage I	Stage II
Mineral precipitation		
Albite	----------------------	
Quartz	----------------------	
Hematite		---------------------------
Magnetite		---------------------------
Pyrite		- - - - -
Chalcopyrite		- - -
Gold		-
REE-phases		- - - - - - -
Alteration		
Albite	----------------------	
Silica	----------------------	--- ---- ---- ---- ----
Iron-oxides		---------------------------
Chlorite		---- ---- ----
Carbonate		---- ----
Sericite		- -
Deformation		
Brecciation	-------	-----
Shearing		- -

Table 4: Mineral and alteration paragenesis

8.2 Regional Context

Figure 27 schematically illustrates timing relationships between the Iron Range iron-oxide mineralization and alteration with respect to the lithologies surrounding the Iron Range.

The oldest units at the Iron Range are the Proterozoic Purcell Basin sediments, which have been intruded by the slightly younger Proterozoic gabbroic Moyie sills. The steeply west dipping Iron Range Fault is believed to be of Proterozoic age and developed parallel to the Purcell rift (Chandler, 2000; Höy et al., 2000; Lydon, 2000). The youngest intrusive units outcropping at the Iron Range are Pennsylvanian carbonatites.

The paleomagnetic data (Chapter 6.2) from the Iron Range iron-oxide mineralization and associated alteration types are consistent with a Cretaceous event. The Bayonne Magmatic Suite, including the Mt. Skelly pluton and the magnetite bearing Leeder stock, are also of Cretaceous age (as dated and discussed in Chapter 6.1).

Cutting the iron-oxide mineralization, as well as all lithologies at the Iron Range are 1-10 mm thick quartz-veinlets that locally form a stockwork. The Moyie Sills and the Pennsylvanian carbonatite have both been sheared by the Iron Range Fault. Furthermore, sericite alteration is found along small shear fabrics within the Cu-bearing zone, which indicates that the Iron Range fault has been active post-Pennsylvanian and most likely into the Cretaceous and contemporaneous with the emplacement of the Bayonne Magmatic Suite.
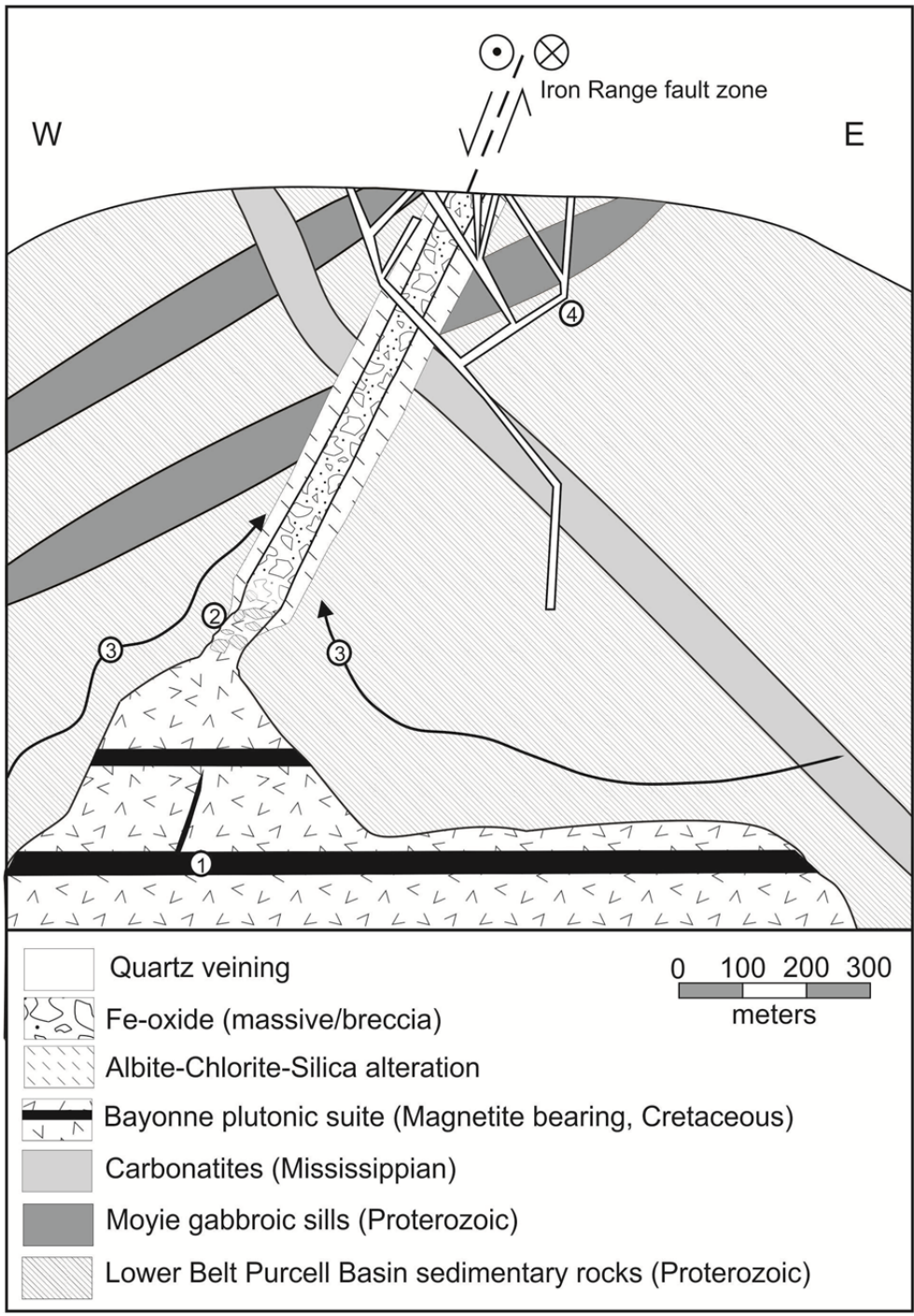
Figure 27: Schematic diagram showing the relative timing relationships between host lithologies, alteration, Iron Range iron-oxide mineralization/brecciation, intrusions, and later quartz veining. 1. Igneous magnetite layers and veins within the Bayonne Magmatic Suite intrusions, 2. Inferred correspondence between the Bayonne Magmatic Suite intrusions and the Iron Range iron-oxide mineralization/breccia derived from paleomagnetism, Ar-Ar geochronology, and geology, 3. Later quartz-gold veins of unknown age. Vertical exaggeration not to scale.

8.3 Brecciation and Iron-oxide Precipitation

The Iron Range alteration and mineralization, located along a structure like the Iron Range Fault could be explained by a hydrothermal over-pressuring scenario similar to the rupturing of over-pressured reservoirs as described in Cox (2005) which is schematically shown in Figure 28 for the Iron Range. The lack of outcrop exposure and limited cross-cutting relationships that can be observed in the trenches make it difficult to relate various observations to each other. Hence, the following hypothesis represents the preferred model based on available data.

Saline, Na-rich fluids, as observed in fluid inclusions, could have moved along the IRFZ and produce the albite alteration observed in the surrounding host-rock. The source of the fluids can be either magmatic or non-magmatic. In the case of non-magmatic fluids, it is assumed that the fluid(s) represent crustal or metamorphic fluids. Assuming a Cretaceous event (supported by the paleomagnetic dating), it is unlikely that the fluids are basinal derived as the Belt-Purcell basin is Proterozoic in age and had been lithified prior to the Cretaceous iron-oxide mineralization. Eventually the migrating fluids attained saturation with respect to albite and quartz and precipitation of these minerals created a low-permeability zone. This low-permeability zone would lead to a pressure increase below, separating a high-pressure fluid reservoir from a lower-pressure reservoir. An increase in permeability of this low-permeability zone (i.e., movement along the IRFZ) could have led to a release of fluids from the overpressured reservoir contemporaneously with brecciation.

This process is indicated by anhedral and altered grains of albite and quartz within the iron oxide breccia that can be either contemporaneous with, or cut by later veins of, euhedral iron oxides. To account for the abundance of hydrothermal or hypogene iron-oxides and lack of sulphides, fluids introduced into the system during brecciation must have been rich in Fe and poor in S. Possible Fe-sources for these fluids could be the Moyie Sills or likely magnetite bearing intrusions of the Cretaceous Bayonne Magmatic Suite, such as the

Leeder Stock.
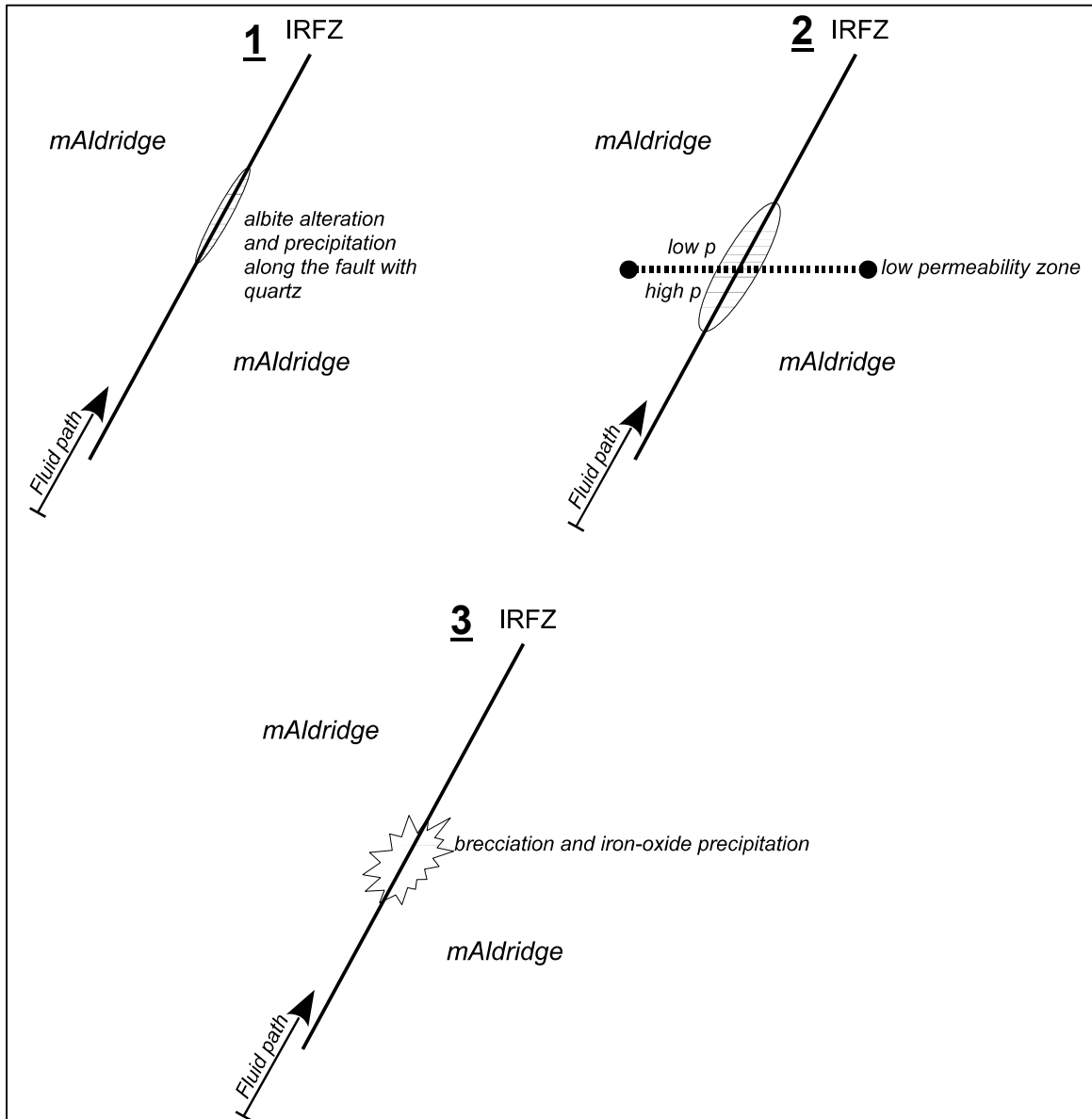
Figure 28: Schematic diagram showing possible iron-oxide precipitation and brecciation scenario.

The sudden decrease in pressure alone is not sufficient for iron-oxide

precipitation, as pressure on its own is usually not associated with and only has

indirect influence on ore formation (Robb, 2005). Most iron in the earth's crust is transported in the ferrous form (Fe^{2+}) and according to Pearson's (1963) classification of metal and ligands in terms of Lewis acids and bases, Fe_2+ is neither a hard or soft metal and belongs to the borderline divalent metals which have a strong preference for complexing with Cl^- or Br^- ligands. In the case of metal-Cl^- complexing in an ore solution, precipitation of metals (e.g., Fe) can be easily achieved by increasing pH (Wood, 1998). Given the possibility that the Fe-bearing fluids were acidic, abundant albitic alteration and presence of sodic feldspar (albite), which precipitated with quartz along the Iron Range Fault, might have been sufficient enough to increase the pH of the Fe-bearing fluid and cause precipitation as feldspar-bearing rocks are efficient at neutralizing acids (Thompson, 2002). This hypothesis is reinforced by the absence of hydrolytic alteration of albite. The brecciation of the sodic altered country rock as described above would create a highly permeable region with abundant surface area to react with the fluid, further enhancing the ability to increase the pH. In the Yerington porphyry district, the Buckskin Range hematite-magnetite-gold-copper lodes, which are similar in alteration and mineralizing fluid composition to the Iron Range iron-oxide mineralization, are believed to have formed by cooling Fe-rich fluids which reacted with wall rocks and became saturated in hematite and magnetite (Dilles et al. 2000). In the complex, multistage history of the Iron Range iron-oxide mineralization an identical mechanism might have played a role in iron-oxide precipitation.

9: DEPOSIT TYPE

9.1 Similarities with IOCG type Systems

The Iron Range deposit shares many characteristics with iron oxide-(Cu-Au) deposits worldwide, which according to Hitzman (1992), Hitzman (2000), Williams et al. (2005), Corriveau (2007) and Hunt et al. (2007) are: hydrothermal veins, breccia and replacement ore styles in specific structural sites (i.e., IRFZ); abundant magnetite and hematite with a low Ti-content; extensive alkali-rich (Na) alteration; CO_2-bearing fluids (Staples et al., 2008); and associated magmatism with no clear spatial association at the structural level of mineralization.

Also, like many IOCGs, the Iron Range mineralization is hosted in Proterozoic strata of a continental margin setting associated with extensional tectonic events (Hitzman et al, 1992), although there are many Phanerozoic examples of IOCG-type deposits especially in the Cordillera (Marschick et al., 2000; Barton et al., 2005). Additionally, the Iron Range mineralization is hosted within a failed continent margin rift setting with mineralization occupying a major fault that formed during rift development (Höy et al. 2000).

The 2008 drilling program revealed Cu- and Au-mineralization at depth and close to the surface, respectively. Cu-mineralization occurs relatively deep in the system (200 m below surface) and the lack thereof in the upper levels of the system could indicate an insufficient trap or source for Cu-mineralization. However, in many IOCG systems sodic alteration is found below the potassic

alteration zone (Barton and Johnson, 2000). Alternatively, the Cu-mineralization at depth could be unrelated to the iron-oxide system and assuming the Iron Range was an IOCG-like system, the potassic alteration zone could have been eroded. The high-grade gold-mineralization traced for 7 m at shallow depths will require further investigation. The gold composition with native gold and limited silver ($Au_{95}Ag_5$) concentration differs from most other IOCG-type mineralization, such as at the Ernest Henry IOCG where the Au content of electrum ranges between 67-92 wt% (Foster et al. 2007). Furthermore, from these preliminary data it appears that the high-grade gold zone is located 200 m above the Cu-mineralization and to date Cu- and Au-mineralization have not been observed together. Other similarities include silica, chlorite and calcite alteration and abundant hematite and magnetite.

IOCG models are complex and varied with respect to the metal and fluid sources. Hitzman et al., (1992), Hitzman (2000), and Barton and Johnson (2000) have proposed genetic models that are distinctly split between magmatic- and non-magmatic-derived fluid sources. In Barton and Johnson's (2000) non-magmatic basinal brine model, high-Cl, low-S content non-magmatic brines will preferentially develop iron oxide-rich, sulfide-poor mineral assemblages. According to their mass and energy balance and phase equilibrium calculations, a pure magmatic source for the fluid would predict high-temperature mineralization of abundant sulfides and modest magnetite contents; sulfide mineralization would be accompanied by deep K-silicate alteration with overprinting and shallower acid alteration. It remains unclear whether the

observed Cu-mineralization at depth at the Iron Range is part of sulfide-rich mineralization formed from a magmatic brine. However, the highly saline brines at the Iron Range (as indicated by fluid inclusions in Chapter 5.1) are more compatible with a non-magmatic brine model that lacked a sufficient metal source and trap.

Lastly, the chemical composition of magnetite (Figure 24) from the Iron Range is consistent with both IOCG and porphyry style hydrothermal systems. However, the bulk of the magnetite compositions and the relatively low Ti-content favours (Table 3) IOCG type mineralization.

9.2 Similarities with Porphyry Systems

The Iron Range also shares characteristics with features related to porphyry style mineralization and alteration. For the most part these features are attributed to IOCG-like systems in Chapter 9.1, which emphasizes the controversy over the IOCG model as its own deposit class.

Features such as hydrothermal veins, diatremes or breccias related to structures, abundant hematite and magnetite, and extensive alkali-rich (Na) alteration are also characteristic of porphyry systems, especially alkalic porphyry systems (Lang et al. 1998, Cooke et al. 2006). British Columbia is a known district for alkalic porphyry system like Mt. Polley, Mount Milligan, Copper Mountain - Ingerbell, Lorraine, Hogem Batholith, Iron Mask Batholith or Galore Creek (Lang et al. 1998) which are mostly restricted to Quesnellia and Stikinia. Locally, the Iron Mask Batholith as well as Copper Mountain – Ingerbell deposits

contain massive (20-100 m thick) zones of extensively sodic altered lithologies as well as massive iron-oxides. In addition, alkalic porphyries such as Mount Polley contain significant amounts of breccias with iron-oxides.

The Iron Range occurrence could also quite easily be placed within a calc-alkalic porphyry system like the Yerrington Batholith in Nevada. The Yerrington Batholith is host to several porphyry copper, skarn and iron-oxide-copper-gold lodes found in the Buckskin Range (Dilles et al. 2000) not exclusively associated with brecciation and sodic (-calcic) alteration. Dilles et al. (2000) argued that within the Yerrington Batholith non-magmatic, saline, deep sodic-calcic fluids used structural pathways and permeable zones for fluid flow, cooled and reacted with wall rock and precipitated iron-oxides. Fluids which formed the iron-oxide lodes at Yerrington are not related to the main ore forming phase of the Yerrington Batholith, and removed metals like Cu and Fe from the deeper parts of the batholith. Figure 29 is a simplified cross-sectional diagram of the Yerrington batholith depicting the hydrothermal and magmatic evolution including the formation of iron-oxide-copper-gold lodes within the system.

The comparison of the Iron Range with Buckskin Range iron-oxide lodes is probably the most compelling one, as it displays very similar textural features, mineralogy and alteration. The fact that K-silicate alteration is absent at the Iron Range (with the exception of one occurrence within a shear at depth, Chapter 3.4) is not inconsistent with the Yerrington model, as at the Buckskin Range iron-oxide lodes, the potassic altered and mineralized porphyry dykes and stocks aren't spatially or genetically associated with the iron-oxide lodes.
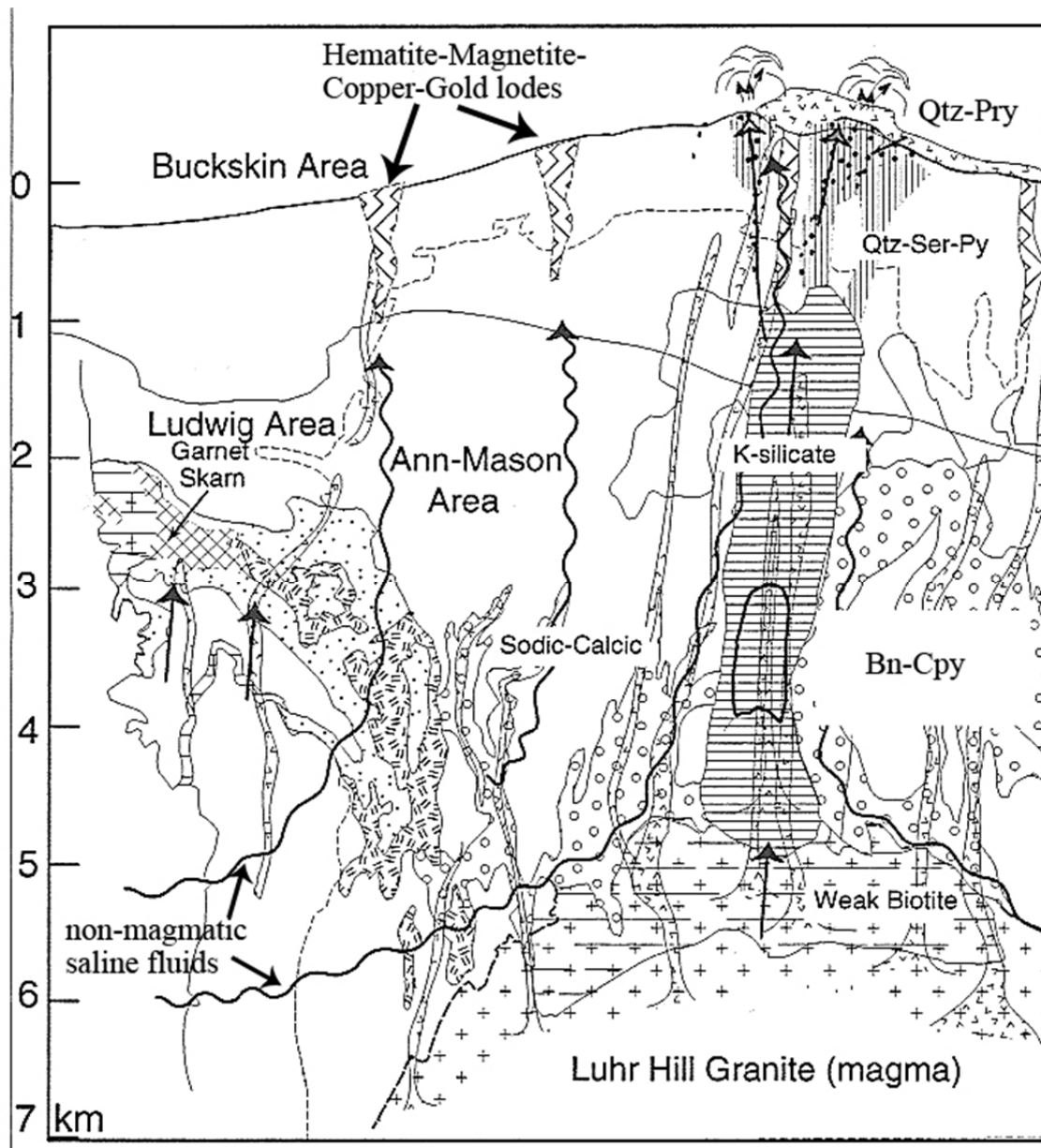
Figure 29: Simplified cross-sectional diagram of the Yerrington batholith illustrating hydrothermal alteration. Also shown are iron-oxide lodes associated with sodic alteration derived from non-magmatic brines coming into the hydrothermal system from outside the pluton (Bn=bornite, Cpy=Chalcopyrite, Pry=pyrophyllite, Py=pyrite, Qtz=quartz, Ser=sericite,) (after Dilles et al., 2000).

10: CONCLUSIONS

The Iron Range iron-oxide occurrences and associated sub economic base-precious metal mineralization are hosted in the Proterozoic Middle Aldridge Formation and are the result of a major, structurally controlled hydrothermal event. This event resulted in massive and brecciated iron-oxide occurrences along an 18 km strike length of the Iron Range fault, ranging in width from 10-150 m.

The iron-oxides are hematite with lesser magnetite which host trace amounts of gold and copper mineralization, and REE element phases. Textural evidence suggests multiple iron-oxide precipitation or recrystallization events. The dominant alteration assemblage associated with the iron-oxide occurrences is silica+/albite+/-chlorite. The relationship of the base and precious metal mineralization to the iron-oxide occurrences is not entirely clear; however, there is evidence that the base and precious metal mineralization formed in the later stages of the hydrothermal system as evidenced by micron-sized REE element phases commonly attached to iron-oxides or occurring as inclusions in chalcopyrite and pyrite suggesting a genetic link between these phases. Additionally, the gold-mineralization is hosted within a strongly quartz-veined area with weakly developed quartz stock-work found at one only location cutting iron-oxides and the host rock which suggest it is a late-stage mineralization.

There are two fluid inclusion populations, which are both very saline. One has carbonic phases while the other is carbonic absent. The fluid inclusion data together with oxygen isotope data indicate temperature conditions of 340-400°C and depths of 6-15 km depth for iron-oxide precipitation. A possible mechanism for the formation of the iron-oxide occurrences is a hydrothermal overpressuring and rupturing scenario.

Ar-Ar dating of regional felsic intrusive rocks in conjunction with paleomagnetic data from the iron-oxide occurrences supports a Cretaceous hydrothermal event that consisted of multiple pulses of hydrothermal fluids that contributed to the iron-oxide occurrences and base-precious metal mineralization. Cretaceous hydrothermal events can be linked to the voluminous Bayonne Plutonic Suite, which is found as within 10 km of the Iron Range in the form of the Mount Skelly pluton. Of note is the Leeder stock that occurs 30-35 km north east of the Iron Range containing magnetite phenocrysts, cumulate magnetite layers, and veins with spatially associated iron-oxide breccias.

The Iron Range shares characteristics with IOCG and porphyry associated mineralization with respect to textures, tectonic setting, alteration and magnetite trace element concentrations and is most compatible with iron-oxide occurrences (veins and breccias) found in the Yerrington porphyry district, e.g., the Buckskin Range.

APPENDICES

Appendix 1: Sample locations

Table 5: Locations and purpose of collected samples

Sample		Location	UTM (NAD 83)	Description	Ar-Ar dating	Geochemical analysis
MG08	1	Hellroaring Cr.	0562481/5488583	Leeder Stock	x	x
MG08	8	Goat River	0548517/5453309	Carbonatite boulder		x
MG08	9	Iron Range	0543443/5453923	Carbonatite	x	x
MG09	10	Angus Creek	0560927/5483376	Granite	x	
MG08	12	Ailsa Lake	0547707/5491403	Granite	x	
MG08	13	Perry Creek	0576982/5485973	Iron-oxide breccia		x
MG08	14	Negro Mnt.	0571106/5479554	Iron-oxide breccia		x
MG08	19	Iron Range	0543399/5453916	massive iron-oxides		x
MG08	20	Iron Range	0543490/5454048	various Moyie sill samples, 20E = altered Aldridge sediments		x
MG08	21	Iron Range	0543465/5453182	massive iron-oxides		x
MG08	22	Iron Range	0543589/5454493	Carbonatite	x	x
MG08	23	Iron Range	0543657/5454505	Aldridge sediments		x
MG08	24	Iron Range	0543528/5453099	Moyie sills		x
MG08	25	Iron Range	0543528/5453099	oxidized boulder		
MG08	28	Mt Skelly	0529863/5471913	Granodiorite	x	x
MG08	29	Iron Range	0543469/5453189	massive and brecciated iron-oxides		x
MG08	33	Iron Range	0542885/5455797	massive and brecciated iron-oxides		
MG08	34	Iron Range	0542885/5455797	massive and brecciated iron-oxides		x
MG08	35	Iron Range	0543187/5453869	Moyie sills		x
MG08	36	Iron Range	0543204/5453889	Moyie sills		x
MG08	37	Iron Range	0543186/5453939	Moyie sills		
MG08	38	Iron Range	0543177/5453898	NW cutting qtz vein with mgnt at contact to gabbro		
MG08	39	Iron Range	0543122/5453660	massive and brecciated iron-oxides		x
MG08	40	IR08010	0543399/5453704	Aldridge sediments		
MG08	41	IR08010	0543122/5453660	Moyie sills		x
MG08	42	Iron Range	0543122/5453661	Moyie sills		
MG08	45	Iron Range	0543381/5453837	massive and brecciated iron-oxides		x
MG08	46	Iron Range	0543388/5453845	massive and brecciated iron-oxides		x
MG08	47	Iron Range	0543377/5453831	massive and brecciated iron-oxides		x

Appendix 2: Iron Range Paleomagnetic Data

Table 6: Analytical data from paleomagnetic dating of the Iron Range iron-oxides for each collected sample with geographic coordinates (Dg/Ig), stratigraphic coordinates (Ds/Dg), 95% confidence interval (α95), natural romance magnetization (NRM), magnetic susceptibility (SUSC) and Koenigsberger ratio (KN)

Sample	Dg	Ig	Ds	Dg	α 95	NRM	SUSC	KN
MIG011A	114	16.1	116.9	55.9	1.3	4.39E-03	7.59E-04	0.15
MIG011B	128.8	51	212.1	78.1	1.9	1.35E-02	8.52E-04	0.4
MIG012A	78.5	10.6	65.6	42.8	1.6	4.71E-03	7.03E-04	0.17
MIG013A	123.7	66	271.3	72.5	1.5	5.00E-02	5.41E-03	0.23
MIG014A	30.9	9	22.5	13.8	0.7	7.56E-03	1.15E-03	0.17
MIG015A	84.3	59.7	336.5	72.4	1.8	9.27E-02	9.22E-03	0.25
MIG016A	255.9	-45.6	197.6	-66.9	1.4	1.04E-01	1.24E-02	0.21
MIG017B	207.4	72.9	265.7	45.1	1.5	4.20E-02	1.76E-03	0.6
MIG021A	147.7	34.7	185.3	58.7	1.3	2.79E-01	3.33E-02	0.21
MIG022A	358.6	17.9	352.4	0.7	1.7	9.33E-02	1.52E-03	1.54
MIG023A	14.3	2.1	14.3	-2	1.7	9.25E-02	2.25E-03	1.03
MIG024A	20.8	32	358.6	24.4	1.5	4.21E-02	1.07E-03	0.98
MIG025A	70.5	52.7	358.3	65.5	1.8	2.68E-01	2.20E-03	3.07
MIG026A	145.1	85	285.1	54	1.6	8.15E-02	3.56E-04	5.75
MIG031A	22.9	70	320	47	2.5	6.48E-01	4.46E-02	0.37
MIG032A	13.9	14.8	5.8	7.5	1.3	6.37E-01	4.22E-02	0.38
MIG033A	314.9	55.9	304.4	17.9	2	1.11E-01	5.23E-02	0.05
MIG034A	37.6	30.8	10.9	34	1.7	9.44E-02	5.28E-02	0.04
MIG035A	348.7	65.1	315.6	33.6	1.8	2.41E-01	2.78E-02	0.22
MIG036A	280.8	-8.9	276.3	-48.2	2.3	1.49E+01	2.07E-01	1.81
MIG037A	229.6	-42.6	186.3	-48.8	2.1	9.87E-01	8.50E-02	0.29
MIG041A	12.9	53.1	12.9	53.1	0.1	2.97E+01	1.98E-01	3.78
MIG041B	26.4	49.8	345.8	39.2	1.7	2.06E+01	1.42E-01	3.65
MIG042A	20.7	45.9	346.8	33.8	2	2.74E+00	7.18E-02	0.96
MIG043A	339	1.6	345.4	-23.6	1.9	6.21E-01	3.31E-03	4.72
MIG043B	342.6	-6.5	353.7	-28.4	1.1	9.33E-01	5.12E-03	4.58
MIG044A	275.9	59.4	282.4	20	1.4	2.14E-01	1.09E-03	4.92
MIG045A	247.3	60.3	268.1	25.5	1.6	2.21E-01	1.73E-03	3.21
MIG047A	6.4	69.5	317.1	41.7	1.5	1.28E+00	2.35E-02	1.37
MIG047B	181.1	79.2	273.2	52.3	1.9	5.09E-01	-	-
MIG051A	306.7	61.1	298.6	22	4.8	1.52E+01	1.67E+00	0.23
MIG051B	41.7	50.2	41.7	50.2	1.8	1.12E+01	1.57E+00	0.18
MIG052A	166.6	63.2	166.6	63.2	0.1	2.46E+00	3.16E-02	1.96
MIG053A	174.9	67.1	174.9	67.1	0.1	1.20E+00	6.45E-03	4.68
MIG053B	180.2	66.6	252.4	52.1	1.8	1.43E+00	6.51E-03	5.52
MIG054A	286.5	36.4	287.2	-3.5	3.8	3.24E+01	1.38E+00	0.59
MIG054B	0	0	0	0	0	6.77E+00	1.68E+00	0.1
MIG055A	173.4	62.3	244.6	54.3	0.7	1.25E+00	7.62E-03	4.12
MIG056A	133.4	67.1	133.4	67.1	0.2	1.76E+00	1.28E-02	3.46
MIG057A	164.9	56.2	232.4	57.3	0.7	1.17E+00	4.46E-03	6.59

Table 6 (continued)

Sample	Dg	Ig	Ds	Dg	α95	NRM	SUSC	KN
MIG061A	215.8	4.5	215	-6.6	1.3	3.52E-01	5.25E-02	0.17
MIG062A	204.4	22.1	217.8	14	2.3	4.89E-01	5.86E-02	0.21
MIG063A	202.7	54.9	243.5	37.5	1.6	3.24E-01	2.86E-02	0.29
MIG064A	206.1	-6	200.8	-8.5	1.2	9.87E-01	6.34E-02	0.39
MIG064B	187.5	42.8	223.8	38.5	1.7	3.80E-01	2.68E-02	0.36
MIG065A	200.8	38.1	227.2	27.7	1.2	3.49E-01	2.45E-02	0.36
MIG065B	199.5	20.4	213.1	15.8	1.1	3.41E-01	2.81E-02	0.31
MIG066A	212.6	51.5	245	30.8	1.8	1.69E+00	1.24E-01	0.34
MIG066B	201.6	47.2	235.6	33.3	3.4	2.76E-01	2.01E-02	0.35
MIG067A	207.5	72.4	264.9	44.8	1.5	1.31E-01	5.93E-03	0.56
MIG067B	213.8	68.1	261.4	40.8	1.8	1.50E-01	5.33E-03	0.71
MIG067C	221.4	63.3	259.2	35.4	1.6	1.45E-01	3.84E-03	0.95
MIG068A	186.3	63.8	249.2	49	1.9	5.61E-01	7.50E-03	1.88
MIG071A	291.2	62.8	290.6	22.8	2	4.06E-01	2.50E-03	4.09
MIG072A	278.8	46.7	282.3	7.2	1.9	3.26E+00	5.33E-03	15.36
MIG073A	346.7	87.2	293.6	48.4	1.8	2.30E-01	1.49E-03	3.88
MIG074A	346.5	-14.8	3.2	-32.6	0.9	5.09E-01	9.94E-04	12.87
MIG081A	254.2	27.1	258.4	-6.6	0.6	1.14E-02	4.09E-04	0.7
MIG081B	110.6	51.4	276	88.6	0.8	7.93E-04	2.03E-04	0.1
MIG082A	243.2	66.6	270.1	31.9	0.4	1.40E-03	4.17E-05	0.84
MIG085A	108.8	35.9	105.9	75.9	0.2	1.58E-03	2.68E-04	0.15
MIG091A	291.4	20.3	291.4	-19.7	1	1.06E-01	6.05E-03	0.44
MIG092A	300.1	20.9	300	-18.5	1.5	1.70E+00	6.25E-02	0.68
MIG093A	103	6	100	45.6	1.4	2.12E-01	1.59E-02	0.34
MIG095A	267.6	40.9	273.2	3.1	0.3	6.19E-02	5.93E-03	0.26
MIG098A	282.2	0.6	279.9	-39	0.8	1.05E-01	1.58E-03	1.67
MIG102A	87.1	71.7	87.1	71.7	1	6.86E-04	2.30E-04	0.07
MIG103A	27.5	45.4	350.9	37.2	0.3	1.42E-03	3.55E-04	0.1
MIG104B	127.7	59.3	249.1	76.3	3.3	1.27E-04	2.99E-04	0.01
MIG105A	86.4	23.2	66.8	57.4	1.7	1.95E-04	2.62E-04	0.02
MIG111A	201.2	-4.3	198.1	-4.1	0.9	7.16E-02	3.10E-03	0.58
MIG111B	209.1	13.2	215.4	4.4	0.9	1.78E-01	5.85E-03	0.76
MIG112A	315	9.2	317.9	-26.9	1.3	2.53E+00	5.00E-02	1.27
MIG113A	219.1	-5	211.6	-16	1.5	1.13E+01	8.65E-02	3.28
MIG113B	218.1	-9.3	208	-18.7	1.7	9.09E+00	8.34E-02	2.74
MIG114B	198.1	-15.7	188.3	-10.8	1.9	1.13E+01	8.88E-02	3.2
MIG115A	222.8	-22.2	202.2	-31.3	1.9	2.07E+01	1.06E-01	4.93
MIG115B	218.3	-20.9	199.7	-27.5	1.6	1.96E+01	1.17E-01	4.2
MIG116A	115.9	8.6	118.8	48.3	0.9	8.76E-01	8.48E-02	0.26

Table 6 (continued)

Sample	Dg	Ig	Ds	Dg	α95	NRM	SUSC	KN
MIG122A	251.9	20.5	253.8	-11.9	1.5	1.23E-01	5.66E-04	5.46
MIG123A	183	49.3	228.7	44.7	1.5	3.86E-02	2.35E-04	4.13
MIG124A	176.1	34.7	208.3	40.5	0.9	8.90E-02	3.66E-04	6.12
MIG126A	293.4	43.6	292.5	3.7	1.4	5.16E-02	4.28E-04	3.03
MIG127A	246	-71.5	136.9	-60.8	2.1	4.04E-02	3.99E-04	2.54
MIG131A	192.8	46.4	230.3	37.7	1	2.34E-01	5.50E-03	1.07
MIG131B	8.7	87.6	293.6	49.5	0.2	1.70E-01	4.60E-03	0.93
MIG132A	167.1	44.7	214.6	51.9	1.1	1.37E-01	4.70E-03	0.73
MIG133A	34.9	84.2	299	51.2	1.9	5.14E-01	1.38E-02	0.93
MIG141A	311.3	51.3	303.5	12.9	0.5	1.48E-03	1.47E-04	0.25
MIG142A	281.9	-40.5	256.2	-78.9	0.3	2.02E-03	1.42E-04	0.36
MIG143A	317.3	81.9	295	42.7	0.5	3.33E-03	2.45E-04	0.34
MIG143B	271.9	72.6	283.6	33.2	0.6	1.98E-02	4.29E-04	1.16
MIG144A	281.1	-15.9	274.8	-55.2	1.8	1.23E-03	1.29E-04	0.24
MIG144B	197.7	6.8	202.6	6.7	0.7	5.09E-04	1.20E-04	0.11

Appendix 3: ^{40}A/^{39}Ar analytical data

Table 7: ^{40}A/^{39}Ar analytical data for collected samples

Power[a]	Volume ^{39}Ar x10^{-11} cc	^{36}Ar/^{39}Ar	±	^{37}Ar/^{39}Ar	±	^{38}Ar/^{39}Ar	±	^{40}Ar/^{39}Ar	±	%^{40}Ar ATM	*^{40}Ar/^{39}Ar	±	f_{39}[b] (%)	Apparent Age Ma[c]	±
MG08-01 Biotite; J=.00425940Bayonne Magmatic Suite (Z9806; 0.0000−N 0.0000−E)															
Aliquot: A															
3.0	0.1004	0.0135	0.0003	0.053	0.911	-0.013	-0.011	18.051	0.031	22.1	14.061	0.100	20.0	104.93	0.73
3.5	0.0513	0.0033	0.0005	0.053	1.773	-0.011	-0.011	15.133	0.047	6.5	14.151	0.175	10.2	105.59	1.27
4.0	0.0778	0.0018	0.0004	0.053	1.173	-0.011	-0.011	14.515	0.032	3.6	13.998	0.116	15.5	104.48	0.84
4.5	0.0348	0.0020	0.0008	0.053	2.611	-0.011	-0.011	14.635	0.066	4.0	14.056	0.255	6.9	104.90	1.85
5.0	0.0540	0.0021	0.0005	0.053	1.688	-0.011	-0.011	14.496	0.047	4.3	13.875	0.167	10.8	103.58	1.21
5.5	0.0502	0.0029	0.0005	0.053	1.814	-0.011	-0.011	14.637	0.052	5.9	13.767	0.180	10.0	102.80	1.31
6.0	0.0320	0.0028	0.0008	0.053	2.840	-0.011	-0.011	14.875	0.075	5.6	14.035	0.278	6.4	104.75	2.02
6.5*	0.0230	0.0025	0.0012	0.053	3.961	0.015	0.011	14.097	0.073	5.1	13.372	0.374	4.6	99.93	2.72
15.0	0.0782	0.0019	0.0003	0.053	1.170	-0.011	-0.011	14.742	0.031	3.8	14.184	0.115	15.6	105.83	0.83
MG08-09b Phlogopite; J=.00425780Mississippian Aley Complex (Z9807; 0.0000−N 0.0000−E)															
Aliquot: A															
2.6*	0.0140	0.0285	0.0022	0.053	7.419	-0.016	-0.011	82.004	0.572	10.3	73.586	1.093	1.7	491.71	6.39
3.0*	0.0357	0.0507	0.0012	0.053	2.912	-0.020	-0.011	132.519	0.553	11.3	117.537	0.791	4.4	732.03	4.05
3.5	0.0580	0.0067	0.0005	0.053	1.800	-0.012	-0.011	129.861	0.493	1.5	127.887	0.573	7.1	784.26	2.85
4.0	0.0373	0.0034	0.0008	0.053	2.792	-0.011	-0.011	83.284	0.354	1.2	82.293	0.507	4.6	541.93	2.88
4.5	0.0962	0.0020	0.0003	0.053	1.088	-0.011	-0.011	71.699	0.260	0.8	71.106	0.297	11.8	477.14	1.75
5.0*	0.0747	0.0014	0.0004	0.053	1.399	-0.011	-0.011	51.841	0.193	0.8	51.437	0.253	9.1	357.27	1.59
5.5	0.0608	0.0009	0.0005	0.053	1.716	-0.011	-0.011	50.740	0.200	0.5	50.464	0.280	7.4	351.14	1.77
6.0	0.0869	0.0009	0.0004	0.053	1.205	-0.011	-0.011	50.751	0.190	0.5	50.482	0.235	10.6	351.25	1.49
6.5	0.0638	0.0009	0.0005	0.053	1.640	-0.011	-0.011	50.348	0.106	0.5	50.086	0.212	7.8	348.74	1.35
7.5	0.1327	0.0003	0.0002	0.053	0.704	-0.011	-0.011	51.068	0.179	0.2	50.969	0.197	16.2	354.32	1.25
15.0	0.1571	0.0004	0.0002	0.053	0.764	-0.011	-0.011	49.758	0.174	0.2	49.652	0.195	19.2	345.99	1.24

Table 7: continued

Power[a]	Volume ^{39}Ar x10^{-11} cc	$^{36}Ar/^{39}Ar$	±	$^{37}Ar/^{39}Ar$	±	$^{38}Ar/^{39}Ar$	±	$^{40}Ar/^{39}Ar$	±	%^{40}Ar ATM	*$^{40}Ar/^{39}Ar$	±	f_{39}[b] (%)	Apparent Age Ma[c]	±
MG08-10a Biotite; J=.00427990Bayonne Magmatic Suite (Z9808; 0.0000−N 0.0000−E)															
Aliquot: A															
2.6*	0.0501	0.0200	0.0006	0.053	1.852	-0.014	-0.011	19.775	0.076	29.9	13.856	0.197	4.3	103.93	1.44
3.0	0.0645	0.0099	0.0004	0.053	1.440	-0.013	-0.011	17.123	0.054	17.1	14.200	0.152	5.5	106.44	1.10
3.5	0.1455	0.0031	0.0002	0.053	0.643	-0.011	-0.011	15.184	0.027	6.1	14.260	0.068	12.5	106.87	0.49
4.0	0.1357	0.0018	0.0002	0.053	0.689	-0.011	-0.011	14.705	0.026	3.5	14.186	0.071	11.7	106.34	0.52
4.5	0.1405	0.0014	0.0002	0.053	0.666	-0.011	-0.011	14.713	0.030	2.8	14.307	0.070	12.1	107.22	0.51
5.0	0.1422	0.0012	0.0002	0.053	0.659	-0.011	-0.011	14.518	0.030	2.4	14.164	0.069	12.2	106.18	0.50
5.5	0.0930	0.0016	0.0003	0.053	1.002	-0.011	-0.011	14.637	0.039	3.2	14.168	0.101	8.0	106.21	0.74
6.0	0.0704	0.0015	0.0004	0.053	1.321	-0.011	-0.011	14.600	0.049	2.9	14.171	0.133	6.1	106.23	0.97
7.0	0.1906	0.0010	0.0001	0.053	0.494	-0.011	-0.011	14.549	0.021	2.1	14.251	0.051	16.4	106.81	0.37
15.0	0.1309	0.0012	0.0002	0.053	0.716	-0.011	-0.011	14.615	0.030	2.5	14.256	0.074	11.3	106.85	0.54
MG08-10b Muscovite; J=.00427670Bayonne Magmatic Suite (Z9809; 0.0000−N 0.0000−E)															
Aliquot: A															
2.6	0.0970	0.0184	0.0003	0.053	0.963	-0.014	-0.011	19.773	0.040	27.6	14.324	0.112	16.2	107.26	0.82
3.2	0.3596	0.0009	0.0001	0.053	0.267	-0.011	-0.011	14.725	0.014	1.9	14.446	0.030	60.1	108.15	0.22
3.6	0.0741	0.0014	0.0004	0.053	1.258	-0.011	-0.011	14.691	0.046	2.8	14.284	0.127	12.4	106.97	0.92
4.0	0.0341	0.0007	0.0008	0.053	2.726	-0.011	-0.011	14.299	0.103	1.4	14.103	0.273	5.7	105.65	1.99
4.5*	0.0093	0.0012	0.0029	0.053	9.995	0.000	-0.011	12.730	0.297	2.8	12.371	0.955	1.6	93.01	7.00
5.0*	0.0109	0.0010	0.0024	0.053	8.499	0.000	0.011	12.935	0.253	2.4	12.631	0.814	1.8	94.91	5.96
6.5*	0.0089	0.0013	0.0030	0.053	10.374	-0.001	-0.011	12.606	0.307	3.0	12.233	0.990	1.5	92.00	7.26
15.0*	0.0041	0.0027	0.0065	0.053	22.349	-0.003	-0.011	10.745	0.655	7.5	9.937	2.114	0.7	75.08	15.65

Table 7: continued

Power[a]	Volume ^{39}Ar x10^{-11} cc	$^{36}Ar/^{39}Ar$	±	$^{37}Ar/^{39}Ar$	±	$^{38}Ar/^{39}Ar$	±	$^{40}Ar/^{39}Ar$	±	%^{40}Ar ATM	*$^{40}Ar/^{39}Ar$	±	f_{39}[b] (%)	Apparent Age Ma[c]	±
MG08-12 Biotite; J=.00427120 Bayonne Magmatic Suite (Z9811; 0.0000−N 0.0000−E)															
Aliquot: A															
2.6*	0.0105	0.0639	0.0026	0.053	8.823	0.039	0.011	23.315	0.259	81.0	4.437	0.813	0.7	33.87	6.15
3.2*	0.0253	0.0296	0.0012	0.053	4.192	0.048	0.011	17.333	0.103	50.5	8.577	0.391	1.7	64.91	2.91
3.5*	0.1200	0.0136	0.0003	0.053	0.793	-0.013	-0.011	14.105	0.029	28.4	10.095	0.087	8.1	76.16	0.64
4.0*	0.1190	0.0017	0.0002	0.053	0.800	-0.011	-0.011	10.789	0.027	4.7	10.282	0.078	8.1	77.53	0.57
4.5*	0.1028	0.0010	0.0003	0.053	0.925	-0.011	-0.011	10.595	0.031	2.8	10.301	0.090	7.0	77.68	0.66
5.0	0.1983	0.0006	0.0001	0.053	0.484	-0.011	-0.011	10.554	0.017	1.6	10.386	0.048	13.5	78.31	0.35
5.5	0.1445	0.0005	0.0002	0.053	0.661	-0.011	-0.011	10.587	0.022	1.5	10.426	0.064	9.8	78.60	0.47
6.0	0.1329	0.0008	0.0002	0.053	0.718	-0.011	-0.011	10.618	0.024	2.1	10.392	0.070	9.0	78.35	0.52
6.5	0.1083	0.0005	0.0003	0.053	0.879	-0.011	-0.011	10.655	0.029	1.4	10.501	0.085	7.4	79.16	0.63
7.0	0.1716	0.0007	0.0002	0.053	0.558	-0.011	-0.011	10.587	0.021	2.0	10.373	0.055	11.6	78.21	0.41
8.0	0.1173	0.0002	0.0003	0.053	0.927	-0.011	-0.011	10.454	0.045	0.5	10.398	0.101	8.0	78.39	0.74
15.0	0.2231	0.0005	0.0001	0.053	0.432	-0.011	-0.011	10.568	0.015	1.4	10.418	0.043	15.1	78.54	0.32
MG08-22 Phlogopite; J=.00426880 Mississippian Aley Complex (Z9812; 0.0000−N 0.0000−E)															
Aliquot: A															
2.6*	0.0129	0.0343	0.0025	0.053	8.336	-0.017	-0.011	121.481	0.778	8.3	111.339	1.373	1.5	701.52	7.17
3.2*	0.0220	0.0279	0.0015	0.053	4.905	-0.016	-0.011	204.204	0.813	4.0	195.949	1.150	2.6	1096.60	4.82
3.6*	0.0347	0.0121	0.0009	0.053	3.115	-0.013	-0.011	179.056	0.490	2.0	175.470	0.702	4.1	1008.61	3.09
4.0*	0.0306	0.0108	0.0011	0.053	3.539	-0.013	-0.011	137.938	0.416	2.3	134.745	0.668	3.6	819.74	3.27
4.5	0.0720	0.0043	0.0005	0.053	1.508	-0.012	-0.011	111.788	0.172	1.1	110.527	0.272	8.4	697.27	1.43
5.5	0.0815	0.0008	0.0004	0.053	1.333	-0.011	-0.011	56.721	0.089	0.4	56.475	0.178	9.5	389.65	1.10
5.0	0.0754	0.0017	0.0005	0.053	1.620	-0.011	-0.011	74.672	0.131	0.7	74.183	0.240	8.8	496.31	1.40
6.5	0.0946	0.0005	0.0003	0.053	1.151	-0.011	-0.011	52.721	0.074	0.3	52.580	0.150	11.1	365.32	0.95
6.0	0.0585	0.0010	0.0005	0.053	1.856	-0.011	-0.011	52.394	0.112	0.5	52.108	0.239	6.9	362.34	1.50
7.0	0.1368	0.0002	0.0002	0.053	0.799	-0.011	-0.011	47.270	0.054	0.2	47.198	0.104	16.0	331.14	0.67
8.0	0.1798	0.0003	0.0002	0.053	0.611	-0.011	-0.011	44.752	0.043	0.2	44.660	0.080	21.1	314.80	0.52
15.0	0.0554	0.0004	0.0006	0.053	1.961	-0.011	-0.011	42.218	0.096	0.3	42.099	0.233	6.5	298.16	1.52

Table 7: continued

Power[a]	Volume ^{39}Ar x10^{-11} cc	$^{36}Ar/^{39}Ar$	±	$^{37}Ar/^{39}Ar$	±	$^{38}Ar/^{39}Ar$	±	$^{40}Ar/^{39}Ar$	±	%^{40}Ar ATM	*$^{40}Ar/^{39}Ar$	±	f_{39}[b] (%)	Apparent Age Ma[c]	±
MG08-28 Biotite; J=.00426570 Bayonne Magmatic Suite (Z9813; 0.0000‾N 0.0000‾E)															
Aliquot: A															
2.4*	0.0004	0.4067	0.0770	0.053	188.076	0.072	0.016	104.527	14.995	115.0	-15.659	-15.913	0.0	-124.72	131.45
3.0*	0.0198	0.0616	0.0017	0.053	5.142	-0.022	-0.011	27.558	0.203	66.0	9.364	0.536	0.5	70.66	3.96
3.5*	0.0926	0.0087	0.0003	0.053	1.108	-0.012	-0.011	14.176	0.043	18.2	11.594	0.116	2.2	87.09	0.85
3.9*	0.1588	0.0037	0.0002	0.053	0.650	-0.011	-0.011	12.865	0.026	8.6	11.764	0.068	3.8	88.33	0.50
4.6*	0.3510	0.0021	0.0001	0.053	0.299	-0.011	-0.011	12.465	0.015	4.9	11.853	0.033	8.5	88.98	0.24
5.5	0.7171	0.0006	0.0000	0.053	0.122	-0.011	-0.011	12.167	0.008	1.3	12.004	0.015	17.3	90.09	0.11
6.0	0.3923	0.0005	0.0001	0.053	0.214	-0.011	-0.011	12.095	0.012	1.1	11.959	0.024	9.5	89.76	0.18
6.5	0.2889	0.0006	0.0001	0.053	0.288	-0.011	-0.011	12.160	0.014	1.4	11.987	0.031	7.0	89.96	0.22
7.0	0.4000	0.0003	0.0001	0.053	0.211	-0.011	-0.011	12.084	0.016	0.8	11.984	0.026	9.7	89.95	0.19
8.5	0.7869	0.0003	0.0000	0.053	0.112	-0.011	-0.011	12.029	0.009	0.8	11.928	0.015	19.0	89.54	0.11
15.0	0.9319	0.0004	0.0000	0.053	0.011	0.008	0.011	12.042	0.009	0.9	11.933	0.011	22.5	89.57	0.08

Appendix 4: Standard deviation for magnetite electron microprobe analyses and electron microprobe detection limits

Table 8: Standard deviation for magnetite electron microprobe analyses

sample	σ	σ	σ	σ	σ	σ	σ	σ	σ	σ	σ	σ
MG08-53-1a	0.0093	0.0000	0.0022	0.0140	0.2551	-	0.0015	0.0082	-	0.0119	-	0.0082
MG08-53-1b	0.0033	-	0.0036	-	0.0523	-	0.0000	0.0044	-	0.0507	-	0.0044
MG09-01-1a	0.0305	-	0.0016	-	0.6132	-	-	0.0059	-	-	-	0.0059
MG09-01-2a	0.0343	-	0.0026	-	0.4999	-	-	0.0061	-	-	-	0.0061
MG09-01-2b	0.0152	-	0.0048	-	0.1770	-	0.0000	0.0009	-	-	-	0.0009
MG09-01-2c	0.0169	-	0.0013	-	0.3088	-	0.0000	0.0118	-	-	-	0.0118
MG08-01-1b	0.0065	0.0014	0.0093	-	0.3247	0.0153	0.0001	0.0125	-	-	-	0.0125
MG08-21-1a	0.0211	-	0.0034	-	0.4580	-	0.0016	0.0043	-	-	-	0.0043
MG08-21-1b	0.0501	-	0.0036	-	0.2475	-	0.0000	0.0060	-	-	0.0000	0.0060
MG08-21-1c	0.0000	-	-	-	0.0000	-	0.0000	0.0000	-	-	0.0000	-
MG08-42-1a	0.0071	0.0879	0.0058	-	0.6432	-	0.0010	0.0139	0.0000	-	0.0000	0.0139
MG08-42-1b	0.0040	0.0000	0.0000	-	0.7160	-	0.0051	0.0008	-	-	-	0.0008
MG08-42-1c	0.0221	0.0000	0.0055	-	0.2865	-	0.0018	0.0027	-	-	-	0.0027

Table 9: Elemental detection limit of electron microprobe used for magnetite analysis

element	Mg	Al	Si	Ca	Ti	V	Cr	Mn	Fe	Co	Ni	Cu	Zn
detection limit (ppm)	66	69	149	64	126	174	125	372	390	253	227	317	219

Appendix 5: Magnetite Electron Microprobe analyses

Table 10: Electron microprobe data for Iron Range magnetite

Sample	Ox% (O)	Ox% (Mg)	Ox% (Al)	Ox% (Si)	Ox% (Ca)	Ox% (Ti)	Ox% (V)	Ox% (Cr)	Ox% (Mn)	Ox% (Fe)	Ox% (Co)	Ox% (Ni)	Ox% (Cu)	Ox% (Zn)
MG08-53-1a-1	0	0.0031	0.0103	0.0504	0.006	0	0.075	0.0062	0	93.1703	0.0056	0.0078	0.0584	0
MG08-53-1a-2	0	0.0025	0.0039	0.0408	0.0012	0.0011	0.0764	0.046	0.0013	93.0903	0.0097	0.0062	0.0236	0
MG08-53-1a-3	0	0.0047	0.0125	0.0268	0.0017	0.0074	0.0933	0.0448	0	93.2844	0	0.0005	0.0015	0.0104
MG08-53-1a-4	0	0.0077	0.0109	0.029	0.0027	0.0177	0.0853	0.0197	0.0018	92.9071	0	0.0202	0.0202	0
MG08-53-1a-5	0	0.0088	0.0169	0.0234	0.0001	0.004	0.067	0	0.0027	93.3987	0.0065	0.0137	0.0203	0
MG08-53-1a-6	0	0.0115	0.0138	0.0375	0.0028	0	0.0866	0.0138	0	92.6685	0.0063	0.0058	0.0119	0
MG08-53-1a-7	0	0.0036	0.0049	0.0249	0.0021	0.0028	0.0808	0.033	0	93.2045	0.0017	0.0161	0.0316	0.0175
MG08-53-1a-8	0	0.0001	0.0107	0.0282	0.002	0.0034	0.0764	0.0286	0.0063	92.7773	0.0003	0.0033	0.033	0.0166
MG08-53-1b-1	0	0.0095	0.0136	0.0571	0.0034	0.0064	0.0716	0.0013	0	92.7155	0	0	0.1566	0.0143
MG08-53-1b-2	0	0.0001	0.0121	0.1368	0	0.0075	0.08	0.0486	0	92.8588	0	0.0095	0.0567	0.002
MG08-53-1b-3	0	0.0001	0.0085	0.0524	0.0018	0	0.0778	0.0054	0	92.7895	0.0119	0.0042	0.0849	0.005
MG09-01-1a-1	0	0.0036	0.0185	0.1538	0	0	0.1704	0	0.003	91.6864	0.0065	0.0032	0	0.0011
MG09-01-1a-2	0	0.0005	0.0163	0.1107	0	0.0049	0.162	0	0	92.5536	0	0.0167	0.0003	0.0086
MG09-01-2a-1	0	0.0001	0.0181	0.068	0	0.0037	0.1358	0	0	91.983	0	0.0063	0.0073	0
MG09-01-2a-2	0	0.005	0.0157	0.1303	0	0	0.1503	0	0	92.9331	0.0043	0.0009	0	0.0038
MG09-01-2a-3	0	0.0018	0.0161	0.0797	0	0.0016	0.1403	0	0.0015	92.1523	0.0049	0.0059	0.001	0.0138
MG09-01-2a-4	0	0.0049	0.0213	0.0504	0.0029	0.0044	0.1441	0	0	92.917	0.0015	0.0013	0	0.013
MG09-01-2b-1	0	0.0001	0.0195	0.0722	0.004	0.0049	0.1384	0	0	92.7454	0.0017	0	0.0073	0
MG09-01-2b-2	0	0.0067	0.0111	0.1025	0	0.004	0.137	0	0.0074	92.6206	0.0141	0.0056	0	0
MG09-01-2b-3	0	0.0001	0.0192	0.0894	0.0019	0	0.1367	0	0	92.3961	0.012	0.0044	0	0.0005
MG09-01-2c-1	0	0.0058	0.0214	0.1216	0.0003	0	0.1443	0	0.0029	92.2564	0	0.004	0.0017	0
MG09-01-2c-2	0	0.0118	0.0231	0.0892	0	0	0.1209	0	0.0047	92.6546	0	0.0048	0.0011	0
MG09-01-2c-3	0	0.0001	0.0206	0.1138	0.003	0	0.1298	0	0	92.8644	0.0086	0	0.0021	0

Beam Current: 40.18   Acc. Voltage: 20.02   Take Off Angle: 40   Tilt Angle: 0   Azimut Angle: 0

Table 10: continued

Sample	Ox% (O)	Ox% (Mg)	Ox% (Al)	Ox% (Si)	Ox% (Ca)	Ox% (Ti)	Ox% (V)	Ox% (Cr)	Ox% (Mn)	Ox% (Fe)	Ox% (Co)	Ox% (Ni)	Ox% (Cu)	Ox% (Zn)
MG08-1b-1-1	0	0.0031	0.1402	0.012	0.0001	0.0115	0.4942	0	0.5145	92.4598	0.0072	0.0172	0.004	0.0035
MG08-1b-1-2	0	0.0001	0.1236	0.0247	0	0.0096	0.4969	0	0.5231	92.2306	0.01	0.0034	0.0165	0.0102
MG08-1b-1-3	0	0.0042	0.1439	0.0269	0	0.0045	0.5046	0	0.5211	91.5574	0.0151	0.0057	0	0.013
MG08-1b-1-4	0	0.012	0.1241	0.0278	0	0.0055	0.4739	0	0.481	92.0308	0.0031	0.004	0	0.0001
MG08-1b-1-5	0	0.0046	0.1355	0.0175	0.0043	0.0186	0.4894	0	0.5057	91.7526	0	0.0148	0	0.0048
MG08-1b-1-6	0	0.0118	0.1235	0.0338	0	0.016	0.5095	0	0.5116	92.0807	0.0086	0.0017	0	0.0136
MG08-21-1a-1	0	0.0001	0.0035	0.0431	0	0	0.0839	0	0	91.6369	0.0026	0.0083	0	0.0031
MG08-21-1a-2	0	0.0131	0.0146	0.0526	0.0041	0	0.08	0	0	92.7339	0.0034	0.0135	0	0.0067
MG08-21-1a-3	0	0.0101	0.0078	0.0374	0.0028	0.0005	0.0925	0	0.003	92.0727	0	0.0211	0.0145	0.0045
MG08-21-1a-4	0	0.0011	0.0018	0.0723	0.0025	0	0.0826	0	0	92.8812	0.0092	0.0177	0.0198	0
MG08-21-1a-5	0	0.0025	0.0145	0.0892	0.0017	0.0029	0.0826	0	0	92.3098	0.0103	0.0118	0.0002	0
MG08-21-1a-6	0	0.0001	0.0114	0.0803	0.0036	0.0027	0.083	0	0	92.5318	0.0021	0.0042	0	0
MG08-21-1b-1	0	0.0001	0.0133	0.0889	0.0004	0	0.1065	0	0.0133	92.3002	0	0.0151	0.0088	0
MG08-21-1b-2	0	0.004	0.0039	0.1122	0.0076	0.0031	0.0973	0	0.0089	92.7951	0.0025	0.0018	0.0039	0
MG08-21-1b-3	0	0.0073	0.0079	0.0161	0.0036	0.0032	0.0952	0	0	92.5528	0	0.0158	0.0057	0.0218
MG08-21-1c-1	0	0.0079	0.0011	0.1597	0.0066	0.003	0.0843	0.0032	0	92.3736	0.0142	0.0077	0.0236	0.0112
MG08-42-1a-1	0	0.0112	0.0292	0.0312	0.0058	0.1936	0.195	0	0	91.4122	0.0078	0.0095	0	0
MG08-42-1a-2	0	0.0001	0.0165	0.037	0.0031	0.0159	0.1789	0	0.0081	93.0481	0.0092	0.0105	0.0045	0.001
MG08-42-1a-3	0	0.0001	0.0314	0.013	0.0024	0.0009	0.1661	0	0.0073	91.608	0	0.0022	0	0
MG08-42-1a-4	0	0.0001	0.0285	0.0266	0.0037	0.0091	0.1721	0	0.0057	92.813	0.0126	0.0145	0.0035	0
MG08-42-1a-5	0	0.0004	0.0273	0.0297	0.0002	0.0016	0.1738	0	0.0052	92.3668	0	0.0235	0	0
MG08-42-1a-6	0	0.0132	0.0242	0.029	0.0107	0.0044	0.2022	0	0.01	92.8794	0	0.0094	0.0044	0
MG08-42-1a-7	0	0.0013	0.0177	0.018	0	0.0085	0.1946	0	0	92.0687	0.0163	0.0167	0.0112	0.0115
MG08-42-1b-1	0	0.0072	0.0042	0.0233	0.0034	0.0065	0.2026	0	0.0075	92.8193	0.0008	0.0048	0.0044	0.018
MG08-42-1b-2	0	0.0144	0.0103	0.029	0.0009	0.0165	0.2014	0	0.0059	91.8067	0	0.0056	0	0.0051
MG08-42-1c-1	0	0.0127	0.0138	0.0303	0.0009	0.0067	0.2153	0	0.0009	92.961	0.0086	0.0066	0.0017	0.0051
MG08-42-1c-2	0	0.01	0.0233	0.0731	0	0.007	0.2206	0	0.0052	92.4416	0	0	0	0.0125
MG08-42-1c-3	0	0.0017	0.0234	0.042	0.0008	0.0234	0.218	0	0	92.9108	0.0008	0.015	0.0006	0.0007

Beam Current: 40.18 *Acc. Voltage: 20.02* *Take Off Angle: 40* *Tilt Angle: 0* *Azimut Angle: 0*

Appendix 6: Geochemical Analyses

Table 11: Geochemical analyses for collected samples

Element	SiO2	Al2O3	Fe2O3	MnO	MgO	CaO	Na2O	K2O	TiO2	P2O5	LOI	Total	Au	Ag	As	Ba	Be	Bi	Br
Unit	%	%	%	%	%	%	%	%	%	%	%	%	ppb	ppm	ppm	ppm	ppm	ppm	ppm
MG08-1	54.02	8.76	25.1	0.712	0.32	1.04	2.18	2.35	1.098	0.06	0.6	100.2	< 1	< 0.5	< 1	423	5	< 2	< 0.5
MG08-8	30.71	9.58	1.63	0.351	7.68	14.3	1.56	3.85	2.697	1.32	15.14	99.46	3	< 0.5	7	1011	5	< 2	< 0.5
MG08-9	37.26	9.1	0.87	0.22	11.06	11.95	0.28	1.73	1.845	0.78	14.66	99.35	5	< 0.5	1	1039	3	< 2	< 0.5
MG08-13	46.66	12.43	29.96	0.008	0.09	0.13	7.02	0.08	0.412	0.03	0.15	99.17	5	< 0.5	2	35	2	< 2	< 0.5
MG08-14	58.01	13.77	14.17	0.011	0.22	2.18	7.63	0.15	0.606	1.39	1.05	99.39	< 1	< 0.5	2	39	1	< 2	< 0.5
MG08-19	4.76	0.28	91.56	0.006	0.04	0.08	0.03	0.04	0.108	0.05	0.76	98.57	6	< 0.5	2	7	2	< 2	< 0.5
MG08-20E	83.47	6.07	3.39	0.021	0.19	0.12	1.68	0.84	0.267	0.05	1.77	99.43	27	< 0.5	46	248	< 1	< 2	< 0.5
MG08-21	32.78	0.73	63.27	0.003	0.01	0.04	0.18	0.06	0.235	0.01	0.32	100	4	< 0.5	3	11	2	< 2	< 0.5
MG08-22A	38.59	7.95	0.8	0.338	13.13	9.72	< 0.01	0.17	1.394	0.34	17.65	99.39	3	< 0.5	9	128	2	< 2	< 0.5
MG08-22C	29.48	6.42	1.42	0.341	11.15	14.8	1.19	0.34	1.717	0.84	23.09	98.72	< 1	< 0.5	2	182	2	< 2	< 0.5
MG08-22D	34.61	8.94	0.77	0.237	11.6	12.21	0.14	1.37	1.864	0.8	16.51	99.15	< 1	< 0.5	3	906	3	< 2	< 0.5
MG08-23	79.63	7.09	2.24	0.065	0.81	0.72	1.89	0.99	0.383	0.09	2.42	98.73	< 1	< 0.5	7	231	1	< 2	1
MG08-24A	44.14	11.15	33.6	0.006	0.05	0.19	6.39	0.05	1.837	0.09	0.48	99.32	< 1	< 0.5	1	31	2	< 2	1
MG08-24B	66.56	12.73	8.96	0.003	0.05	0.09	7.03	0.03	2.195	0.07	0.77	98.87	< 1	< 0.5	< 1	46	1	< 2	< 0.5
MG08-28	68.64	16.09	0.25	0.102	0.45	3.68	4.04	2.46	0.261	0.08	0.39	99.24	< 1	< 0.5	< 1	1006	3	< 2	< 0.5
MG08-29	64.78	6.02	21.47	0.011	0.35	0.17	2.64	0.14	0.323	0.06	1.68	98.74	< 1	< 0.5	< 1	32	1	< 2	< 0.5
MG08-34	60.61	0.6	37.1	0.005	0.02	0.04	0.29	0.04	0.15	0.02	0.19	100.9	< 1	< 0.5	1	9	1	< 2	< 0.5
MG08-35	46.52	17.66	4.74	0.146	7.11	0.78	5.04	0.52	1.046	0.08	4.42	98.78	< 1	< 0.5	< 1	84	1	< 2	1
MG08-36	44.4	18.25	4.35	0.165	8.83	0.74	4.66	0.3	1.167	0.09	5.52	100	< 1	< 0.5	1	93	1	< 2	< 0.5
MG08-39	12.37	0.48	83.92	0.004	0.03	0.04	0.23	0.01	0.274	0.08	0.04	100.4	< 1	< 0.5	2	6	3	< 2	< 0.5
MG08-41	58.95	2.24	34.13	0.006	0.05	0.04	1.26	0.08	0.276	0.03	0.18	98.54	< 1	< 0.5	1	8	2	< 2	1
MG08-45E	46.54	9.11	34.2	0.006	0.11	0.23	5.12	0.05	1.347	0.14	0.25	99.03	< 1	< 0.5	< 1	15	1	< 2	< 0.5
MG08-46	72.97	0.25	19.3	0.013	0.04	0.04	0.05	0.08	0.033	0.2	4.39	98.91	1810	6.9	86	12	1	< 2	3
MG08-47	41.42	0.17	57.82	0.002	0.02	0.02	0.09	< 0.01	0.069	< 0.01	0.1	> 101.0	< 1	< 0.5	1	9	1	< 2	1
Detection Limit	0.01	0.01	0.01	0.001	0.01	0.01	0.01	0.01	0.001	0.01		0.01	1	0.5	1	1	1	2	0.5
Analysis Method	FUS-ICP	FUS-ICP	FUS-ICP	FUS-ICP	FUS-ICP	FUS-ICP	FUS-ICP	FUS-ICP	FUS-ICP	FUS-ICP	FUS-ICP	FUS-ICP	INAA	MULT INAA / TD-ICP	INAA	FUS-ICP	FUS-ICP	TD-ICP	INAA

*(row label at left of table: **Sample:**)*

Table 11: continued

	Element	Cd	Co	Cr	Cs	Cu	Hf	Hg	Ir	Mo	Ni	Pb	Rb	S	Sb	Sc	Se	Sr	Ta	Th	U
	Unit	ppm	ppm	ppm	ppm	ppm	ppm	ppm	ppb	ppm	ppm	ppm	ppm	%	ppm	ppm	ppm	ppm	ppm	ppm	ppm
Sample:	MG08-1	< 0.5	18	89	3	29	8	< 1	< 1	3	11	14	70	0.007	0.9	4.2	< 0.5	313	1.6	11.3	8.8
	MG08-8	< 0.5	44	164	35	60	8	< 1	< 1	7	84	102	300	0.363	3.1	21.6	3	1254	8.2	19.3	5.8
	MG08-9	< 0.5	46	470	7	11	6	< 1	< 1	< 2	267	< 5	100	0.048	2.7	22.7	1	579	6.6	11.5	3.1
	MG08-13	< 0.5	4	34	< 0.2	9	3	< 1	< 1	< 2	8	< 5	< 10	0.008	2.7	11.5	< 0.5	70	< 0.3	8.7	2.9
	MG08-14	< 0.5	2	53	2	3	7	< 1	< 1	< 2	6	< 5	< 10	0.014	0.9	5.3	< 0.5	81	< 0.3	8	4.3
	MG08-19	0.9	11	29	< 0.2	< 1	< 0.2	< 1	< 1	< 2	44	< 5	< 10	0.005	2.2	17.9	< 0.5	3	< 0.3	0.7	1.2
	MG08-20E	< 0.5	8	89	2	121	6	< 1	< 1	6	20	11	40	0.013	6.5	4.8	< 0.5	62	0.7	7.8	3.6
	MG08-21	0.5	2	99	< 0.2	6	1	< 1	< 1	4	16	< 5	< 10	0.004	6.8	18	< 0.5	3	< 0.3	3.8	2
	MG08-22A	< 0.5	41	918	2	1	3	< 1	< 1	< 2	372	66	< 10	0.003	3.4	36	< 0.5	295	2.1	6.3	0.9
	MG08-22C	< 0.5	31	612	2	5	4	< 1	< 1	< 2	164	25	< 10	0.066	3.5	23.1	< 0.5	759	5.9	13.9	2.9
	MG08-22D	< 0.5	50	514	6	12	7	< 1	< 1	< 2	276	< 5	80	0.056	8.6	23.7	< 0.5	597	7	12.4	3.2
	MG08-23	< 0.5	6	75	3	11	8	< 1	< 1	3	27	15	30	0.021	9.4	6.7	< 0.5	86	< 0.3	8.8	2.4
	MG08-24A	< 0.5	2	195	< 0.2	< 1	3	< 1	< 1	< 2	7	< 5	< 10	0.004	3.6	15.3	< 0.5	30	< 0.3	3.1	2.3
	MG08-24B	< 0.5	3	295	< 0.2	1	5	< 1	< 1	< 2	8	< 5	< 10	0.004	4.2	15.1	< 0.5	36	1.2	3.6	1.3
	MG08-28	< 0.5	2	76	4	7	6	< 1	< 1	5	3	18	100	0.016	2.7	3.3	< 0.5	972	< 0.3	5.6	3.7
	MG08-29	< 0.5	3	58	2	< 1	10	< 1	< 1	2	9	< 5	< 10	0.004	2.2	8.7	< 0.5	38	< 0.3	8.2	2.3
	MG08-34	< 0.5	1	60	< 0.2	2	< 0.2	< 1	< 1	3	4	< 5	< 10	0.014	1.7	13.7	< 0.5	3	< 0.3	0.3	0.5
	MG08-35	< 0.5	29	365	< 0.2	3	2	< 1	< 1	< 2	161	< 5	< 10	0.002	1.6	43.8	< 0.5	31	< 0.3	1.2	< 0.1
	MG08-36	< 0.5	36	254	< 0.2	5	2	< 1	< 1	< 2	179	< 5	< 10	0.003	1.2	38.7	< 0.5	12	< 0.3	1.3	< 0.1
	MG08-39	0.6	1	51	< 0.2	1	< 0.2	< 1	< 1	< 2	9	< 5	20	0.001	3	25.5	< 0.5	3	< 0.3	0.5	1.4
	MG08-41	< 0.5	3	90	< 0.2	1	< 0.2	< 1	< 1	4	7	< 5	< 10	0.069	1.7	11.9	4	6	< 0.3	0.6	1
	MG08-45E	< 0.5	2	171	< 0.2	2	3	< 1	< 1	< 2	9	< 5	< 10	0.002	1.3	18.1	< 0.5	30	1.2	2.4	1.2
	MG08-46	< 0.5	158	108	< 0.2	> 10000	< 0.2	< 1	< 1	6	192	126	< 10	0.828	5.1	4.6	123	4	< 0.3	0.3	1.3
	MG08-47	0.5	1	74	< 0.2	13	< 0.2	< 1	< 1	< 2	5	< 5	< 10	0.003	2.3	10.1	< 0.5	< 2	< 0.3	0.5	0.9
	Detection Limit	0.5	0.1	0.5	0.2	1	0.2	1	1	2	1	5	10	0.001	0.1	0.01	0.5	2	0.3	0.1	0.1
	Analysis Method	TD-ICP	INAA	INAA	INAA	TD-ICP	INAA	INAA	INAA	TD-ICP	TD-ICP	TD-ICP	INAA	TD-ICP	INAA	INAA	INAA	FUS-ICP	INAA	INAA	INAA

Table 11: continued

	Element	V	W	Y	Zn	Zr	La	Ce	Nd	Sm	Eu	Tb	Yb	Lu	Mass	C-Total	Total S	FeO
	Unit	ppm	ppm	ppm	ppm	ppm	ppm	ppm	ppm	ppm	ppm	ppm	ppm	ppm	g	%	%	%
Sample:	MG08-1	940	< 1	10	318	264	11.9	27	11	2.6	0.9	< 0.1	1.5	0.27	1.59	0.04	< 0.01	3.57
	MG08-8	264	10	35	112	304	154	253	124	14	5.2	2	2.5	0.37	1.44	3.99	0.53	9.57
	MG08-9	186	9	21	115	133	110	181	80	8.7	3.2	1	1.6	0.27	1.33	3.29	0.05	8.63
	MG08-13	240	22	15	43	136	29.6	54	18	4.7	0.9	< 0.1	1.8	0.33	1.85	0.1	0.01	1.98
	MG08-14	194	< 1	58	6	105	13.7	28	16	6.4	1.8	2	4.6	0.69	1.61	0.17	0.02	0.18
	MG08-19	606	15	4	10	11	1	3	< 1	0.5	< 0.05	< 0.1	0.5	0.08	2.93	0.1	< 0.01	0.78
	MG08-20E	22	< 1	19	20	165	23	46	17	3.4	0.9	0.8	2.1	0.37	1.45	0.06	< 0.01	1.39
	MG08-21	572	66	4	14	83	1.1	4	< 1	0.5	0.1	< 0.1	0.7	0.16	2.44	0.05	< 0.01	1.86
	MG08-22A	193	< 1	10	272	91	44.4	78	34	4.8	1.5	< 0.1	0.8	0.13	1.4	3.73	< 0.01	7.79
	MG08-22C	168	8	16	103	117	119	174	90	9.2	3.1	0.9	1.3	0.21	1.44	5.88	0.14	7.12
	MG08-22D	189	9	20	121	133	122	201	95	9.7	3.4	1.4	1.7	0.26	1.18	3.57	0.05	9.08
	MG08-23	33	2	24	96	241	32.9	54	18	4.8	1.2	0.9	2.7	0.42	1.49	0.3	0.02	2.16
	MG08-24A	297	14	29	4	127	5.1	9	6	3.4	0.8	0.9	2.2	0.4	1.85	0.05	< 0.01	1.19
	MG08-24B	144	9	71	3	152	19.2	38	25	12.4	2.3	2.4	4.5	0.67	1.73	0.04	< 0.01	0.33
	MG08-28	24	< 1	22	52	219	24.2	38	10	3.8	1.1	< 0.1	2.5	0.45	1.43	0.04	0.01	2.51
	MG08-29	238	29	8	12	302	9.9	18	9	2.3	0.5	< 0.1	1.4	0.25	1.72	0.05	0.01	0.99
	MG08-34	393	51	2	2	8	0.7	2	< 1	0.3	< 0.05	< 0.1	0.2	< 0.01	1.96	0.03	0.02	1.7
	MG08-35	243	< 1	7	88	71	68.6	94	42	6.7	0.9	< 0.1	1.2	0.22	1.14	0.03	< 0.01	9.65
	MG08-36	244	< 1	6	113	63	11.7	19	6	2	0.3	< 0.1	1.3	0.19	1.48	0.05	< 0.01	10.4
	MG08-39	849	121	3	5	5	6.4	13	7	2.4	0.5	0.2	< 0.05	0.06	2.46	0.03	< 0.01	2.65
	MG08-41	515	32	< 1	3	17	1.7	4	< 1	0.7	0.1	< 0.1	0.3	0.04	1.78	0.03	0.08	1.16
	MG08-45E	320	57	9	2	75	8.8	16	7	2.9	0.5	< 0.1	1.2	0.17	1.73	0.03	< 0.01	1.74
	MG08-46	190	< 1	3	6	27	1.3	2	< 1	0.7	0.7	< 0.1	0.5	0.08	1.77	0.18	0.91	1.39
	MG08-47	489	48	< 1	3	23	0.3	< 1	< 1	0.1	< 0.05	< 0.1	0.1	< 0.01	2.16	0.02	0.01	1.22
	Detection Limit	5	1	1	1	2	0.05	1	1	0.01	0.05	0.1	0.05	0.01		0.01	0.01	0.01
	Analysis Method	FUS-ICP	INAA	FUS-ICP	MULT INAA / TD-ICP	FUS-ICP	INAA	INAA	INAA	INAA	INAA	INAA	INAA	INAA	INAA	IR	IR	TITR

REFERENCES

Anderson, H. E., and Goodfellow, W. D., 2000, Geochemistry and isotope chemistry of the Moyie sills: Implications for the early tectonic setting of the Mesoproterozoic Purcell Basin, in Lydon, J.W., Höy, T., Slack, J.F., and Knapp, M., ed., The Geological Environment of the Sullivan Deposit, British Columbia: Geological Association of Canada, Mineral Deposits Division, Special Publication, no. 1, p. 1302-321.

Archibald, D.A., Krogh, T.E., Armstrong, R.L. and Farrar, E., 1984, Geochronology and Tectonic Implications of Magmatism and Metamorphism, Southern Kootenay Arc and Neighbouring Regions, Southeastern British Columbia. Part II: mid-Cretaceous to Eocene; Canadian Journal of Earth Sciences, v. 21, p. 567-583.

Barton, M.D., and Johnson, D.A., 2000, Alternative brine sources for Fe oxide (-Cu-Au) systems: Implications for hydrothermal alteration and metals, in Porter, T. M., ed., Hydrothermal iron oxide copper-gold and related deposits: A global perspective: Adelaide, Australian Mineral Foundation, v. 2, p. 43-60.

Barton, M.D., Johnson, D.A., and Zuercher, L., 2000, Phanerozoic iron-oxide (-REE-Cu-Au-U) systems in south-western North America and their origins: EGRU Contribution, v.58, p. 5-11.

Beaudoin, G., and Dupuis, C., 2009, Iron-oxide trace element fingerprinting of mineral deposit types, in Corrivueau, L., and Mumin, H., eds., Exploring for Iron Oxide Copper-Gold Deposits: Canada and Global Analogues, Mineral Deposits Division, Geological Association of Canada and Geological Survey of Canada. Short Course Volume 20, p. 111-126.

Brown, D.A., and Stinson, P., 1995, Geologic mapping of the Yahk map area, southeastern British Columbia (82F/1): British Columbia Geological Fieldwork 1994, British Columbia Ministry of Energy and Mines, Paper 1995-1, p. 111-125.

Cathelineau, M., and Nieva, D., 1985, A chlorite solid solution geothermometer – The Los Azufres (Mexico) geothermal system: Contributions to Mineral Petrology, vol .91, p. 235-244.

Chandler, F. W., 2000, The Belt-Purcell Basin as a low-latitude passive rift: Implications for the geological environment of Sullivan type deposits, in Lydon, J.W., Höy, T., Slack, J.F., and Knapp, M., ed., The Geological Environment of the Sullivan Deposit, British Columbia: Geological Association of Canada, Mineral Deposits Division, Special Publication, no. 1, p. 82-112.

Clayton, R.N., and Mayeda, T.K., 1963, The use of bromine pentafluoride in the extraction of oxygen from oxides and silicates for isotopic analysis: Geochimica et Cosmochimica Acta, v. 27, p, 43-52.

Clement, B. M., 2004, Dependence of the duration of geomagnetic polarity reversals on site latitude: Nature, v. 428, p. 637-639.

Cole, D.R., Horita, J., Eniamin, V., Polyakov, V.B., Valley, J.W., Spicuzza, M.J., and Coffey, D.W., 2004, An experimental and theoretical determination of oxygen isotope fractionation in the system magnetite-H2O from 300 to 800 °C: Geochimica et Cosmochimica Acta, v. 68, p.3569-3585.

Cooke, D., Tosdal, D., Chamberlain, C., Deyell, Bath, A., Jackson, M., Jago, P., Pass, H., Micko, J., and Henriques F., 2006, Shallow- and Deep-Level Alkalic Mineral Deposits: Developing an Integrated Exploration Model: Year 1-Porphyry Module, Update to Project Supporters: MDRU-UBC.

Corriveau, L., 2007, Iron oxide copper-gold deposits: A Canadian Perspective, in Goodfellow, W.D., ed., Mineral Deposits of Canada: A Synthesis of Major Deposit-Types, District Metallogeny, the Evolution of Geological Provinces, and Exploration Methods: Geological Association of Canada, Mineral Deposits Division, Special Publication No. 5, p. 307-328.

Cox, S.F., 2005, Coupling between deformation, fluid pressures, and fluid flow in ore-producing hydrothermal systems at depth in the crust: Economic Geology, 100th Anniversary Volume, p. 39-75.

Deer, W. A., Howie, R. A., and Zussman, J., 1997, Rock-forming Minerals, Vol. 5B: Non-silicates, sulphates, carbonates, phosphates, halides: Geological Society, London.

Dilles, J.H., Einaudi, M.T., Profett, J., and Barton, M.D., 2000, Overview of the Yerrington Porphyry Copper District: Magmatic to Nonmagmatic Sources of Hydrothermal Fluids, Their Flow Paths, Alteration Effects on Rocks, and Cu-Mo-Fe-Au Ores; in Thompson, T.B., ed., Part I. Contrasting Styles of Intrusion-Associated Hydrothermal Systems, Society of Economic Geologists: Guidebook Series v. 32, p. 55-66.

Groves, D.I., and Vielreicher, N.M., 2001, The Phalabowra (Palabora) carbonatite-hosted magnetite-copper sulfide deposit, South Africa: An end-member of the iron oxide-copper-gold-rare earth element deposit group?: Mineralium Deposita, v. 36, p. 189-194.

Helsel, D., 2005, Nondetects and Data Analysis: Wiley, New York. 268 p.

Hitzman, M.W., Oreskes, N., and Einaudi, M.T., 1992, Geological characteristics and tectonic setting of Proterozoic iron oxide (Cu-U-Au-REE) deposits: Precambrian Research, v. 58, p. 241-287.

Hitzman, M.W., 2000, Iron oxide-Cu-Au deposits. What, where, when, and why, in Porter, T. M., ed., Hydrothermal iron oxide copper-gold and related deposits a global perspective: Adelaide, Australian Mineral Foundation, p. 9-26.

Höy, T., 1989, The age, chemistry, and tectonic setting of the Middle Proterozoic Moyie Sills, Purcell Supergroup, southeastern British Columbia: Canadian Journal of Earth Sciences, v. 26, p. 2305-2317.

Höy, T., 1993, Geology of the Purcell Supergroup in the Fernie west-half map Area, Southeastern British Columbia: British Columbia Ministry of Energy, Mines and Petroleum Resources, v. 84.

Höy, T., Anderson, D., Turner, R. J. W., and Leitch, C. H. B., 2000, Tectonic, magmatic, and metallogenic history of the early synrift phase of the Purcell Basin, southeastern British Columbia, in Lydon, J.W., Höy, T., Slack, J.F., and Knapp, M., ed., The geological environment of the Sullivan Deposit, British Columbia: Geological Association of Canada, Mineral Deposits Division, Special Publication, no. 1, p. 132-160.

Höy, T., Jackaman, W., Terry, D., and Grant, B., 2003, St. Mary Map-Sheet, Purcell Supergroup, Southeastern British Columbia: British Columbia Geological Fieldwork 2003, British Columbia Ministry of Energy and Mines, Paper 2004-1, p. 191-194.

Hunt, J.A., Baker, T., and Thorkelson, D.J., 2007, A Review of Iron Oxide Copper-Gold Deposits, with Focus on the Wernecke Breccias, Yukon, Canada, as an Example of a Non-Magmatic End Member and Implications for IOCG Genesis and Classification: Exploration and Mining Geology, v. 16, p. 209-232.

Irving, E. and Archibald, D., 1991, Bathozonal tilt corrections to paleomagnetic data from mid Cretaceous plutonic rocks - examples from the Omineca Belt, British Columbia: Journal of Geophysical Research-Solid Earth and Planets, v. 95, p. 4579-4585.

Land, J.R., Thompson, J.F.H., and Stanley, C.R., 1998, Alkalic Cu-Au-Ag Porphyry Deposits in the Canadian Cordilerra: Tectonic Setting, Magmatic Affiliation and Hydrothermal Characteristics; in Metallogeny of Volcanic Arcs: BC Geological Survey, Short Course Notes, Open File 1995-5, Section B.

Legun, A., 2000, Sub-basin recognition in the Purcell Anticlinorium: British Columbia Geological Fieldwork 1996, British Columbia Ministry of Energy, Mines and Petroleum Resources, Paper 1997-1, p. 187-198.

Logan, J. M., and Mann, R., 2000, Geology and mineralization of the Mount Skelly pluton, Kootenay Lake, southeastern British Columbia: British Columbia Ministry of Energy, Mines and Petroleum Resources, Open File 2000-08.

Logan, J. M., 2002, Intrusion-Related Gold Mineral Occurrences of the Bayonne Magmatic Belt; in Geological Fieldwork 2001: BC Ministry of Energy and Mines, Paper 2002-1, p. 237-246.

Lowe, C., Brown, D.A., Best, M.E., and Shives, R.B.K., 2000, High resolution geophysical survey of the Purcell basin and Sullivan Deposit: Implication for bedrock geology and mineral exploration, in Lydon, J.W., Höy, T., Slack, J.F., and Knapp, M., ed., The geological environment of the Sullivan Deposit, British Columbia: Geological Association of Canada, Mineral Deposits Division, Special Publication, no. 1, p.335-369.

Lydon, J.W., 2000, A synopsis of the current understanding of the geological environment of the Sullivan deposit, in Lydon, J.W., Höy, T., Slack, J.F., and Knapp, M., ed., The geological environment of the Sullivan Deposit, British Columbia: Geological Association of Canada, Mineral Deposits Division, Special Publication, no. 1, p.12-31.

Lydon, J.W., 2007, Geology and metallogeny of the Belt-Purcell Basin, in Goodfellow, W.D., ed., Mineral Deposits of Canada: A Synthesis of Major Deposit-Types, District Metallogeny, the Evolution of Geological Provinces, and Exploration Methods: Geological Association of Canada, Mineral Deposits Division, Special Publication No. 5, p. 581-607.

Massey, N.W.D., MacIntyre, D.G., Desjardins, P.J. and Cooney, R.T., 2005: Digital Geology Map of British Columbia: Whole Province, B.C. Ministry of Energy and Mines: Geofile 2005-1, scale 1:250,000.

Marshall, L.J., and Downie, C.C., 2002, Geological report for the Iron Range project, Deli 1-8, FeO 1-30, HC 1-10, IOx 1-12, Ir 1-36, Luke 1-8, and Tck 1-8 properties: Eagle Plains Resources Ltd., Internal Report, 79 p.

Marschik, R., Leveille, R.A., and Martin, W., 2000, La Candelaria and the Punta del Cobre district, Chile: Early Cretaceous iron-oxide Cu-Au (-Zn-Ag) mineralization, in Porter, T.M., ed., Hydrothermal iron oxide copper-gold and related deposits: A global perspective: PGC Publishing, Adelaide, v. 1, p. 163-175.

McMechan, M. E. 1981. The Middle Proterozoic Purcell Supergroup in the southwestern Rocky and southeastern Purcell Mountains, British Columbia, and the initiation of the Cordilleran miogeocline, southern Canada and adjacent United States: Bulletin of Canadian Petroleum Geology, v. 29, p. 583 -621.

McMechan, M.E., and Price, R.A. 1982, Superimposed low-grade metamorphism in the Mount Fisher area, southeastern British Columbia - implications for the East Kootenay orogeny; Canadian Journal of Earth Sciences, v.19, p. 476-489.

Mumin, A.H., Somarin, A.K., Jones, B., Corriveau, L., Ootes, L. and Camier, J., 2008, The IOCG-Porphyry-Epithermal Continuum of Deposits types in the Great Bear Magmatic Zone, Northwest Territories, Canada. in Corrivueau, L., and Mumin, H., eds., Exploring for Iron Oxide Copper-Gold Deposits: Canada and Global Analogues, Mineral Deposits Division, Geological Association of Canada and Geological Survey of Canada. Short Course Volume 20, p. 57-75.

NRCAN, 2003, Magnetic Anomaly Map of North America, Geoscience Data Repository, http://gdr.nrcan.gc.ca/aeromag/index_e.php.

O'Neil, J.R., and Taylor, H.P. Jr., 1967, The oxygen isotope and cation exchange chemistry of feldspars: American Mineralogist, v. 52, p. 1414-1437.

Oreskes, N., and Einaudi, M.T., 1990, Origin of Rare Earth Element-Enriched Hematite Breccias at the Olympic Dam Cu-U-Au-Ag Deposit, Roxby Downs, South Australia: Economic Geology, v. 85, p. 1-28.

Pope, A. J. 1990. The geology and mineral deposits of the Toby Horsethief Creek map area, northern Purcell Mountains, southeast British Columbia: British Columbia Ministry of Energy, Mines and Petroleum Resources, Open File 1990-26.

Pouchou, J.L., and Pichoir, F., 1985, PAP f (r Z) procedure for improved quantitative microanalysis: Microbeam Analysis, p. 104-106.

Price, R. A., and J. W. Sears., 2000, A preliminary palinspastic map of the Mesoproterozoic Belt-Purcell Supergroup, Canada and USA; Implications for the tectonic setting and structural evolution of the Purcell Anticlinorium and the Sullivan deposit, in Lydon, J.W., Höy, T., Slack, J.F., and Knapp, M.E., eds., The geological environment of the Sullivan Deposit, British Columbia: Geological Association of Canada, Mineral Deposits Division, Special Publication, no. 1, p. 161-181.

Ryley, J.K., 2009, 2009 Field exploration and diamond drilling report – Volume 1, Report on the Iron Range property, Eagle Plains Resources Ltd. Internal report.

Schandl, E.S., and Davis, D.W., 2000, Geochronology of the Sullivan deposit: U-Pb and Pb-Pb ages of zircons and titanites, Chapter 8 in Lydon, J.W., Höy, T., Slack, J.F., and Knapp, M., eds., The Geological Environment of the Sullivan Pb-Zn-Ag Deposit, British Columbia: Geological Association of Canada, Mineral Deposits Division, Special Publication No. 1, p. 127-135.

Schmidt, P.W., and Clark, D.A., 1994, Palaeomagnetism and magnetic anisotropy of Proterozoic banded-iron formations and iron ores of the Hamersley basin, Western Australia: Precambrian Research, v. 69, p. 133–155.

Sears, J. W., and Price, R. A. 1978. The Siberian connection: a case for Precambrian separation of the North American and Siberian cratons: Geology, v. 6, p. 267-270.

Sheppard, S.M.F., 1986, Characterization and isotopic variations in natural waters, in Valley, J.W., Taylor, H.P. Jr., and O'Neil, J.R., ed., Stable isotopes in high temperature geological processes: Reviews in Mineralogy v. 16, p. 165-183.

Sillitoe, R.H., 1997, Characteristics and controls of the largest porphyry copper-gold and epithermal gold deposits in the circum-Pacific region: Australian Journal of Earth Sciences, v. 44, p. 373-388.

Staples, R., Marshall, D., Fecova, K., Downie, C. C., Thorkelson, D. J. and Loughrey, L,, 2008, Structurally controlled iron oxide mineralization in the Iron Range and Mount Thompson region, B.C., Geological Survey of Canada: Current Research, no. 2008-15, 12p.

Stinson, P., and Brown, D.A., 1995, Iron Range deposits, Southeastern British Columbia (82F/1): British Columbia Geological Fieldwork 1994, British Columbia Ministry of Energy and Mines, Paper 1995-1, p. 127-134.

Thompson, T.B., 2002, Part I. Contrasting Styles of Intrusion-Associated Hydrothermal Systems, Society of Economic Geologists: Guidebook Series v. 32.

Walker, R.T., 1998, Assessment report for the Mikala / Shah Claims: British Columbia Geological Survey, Assessment Report 25 657, 37 p.

Wanhainen, C., Broman, C., and Martinsson, O., 2003, The Aitik Cu-Au-Ag deposit in northern Sweden: A product of high salinity fluids: Mineralium Deposita, v. 38, p. 715-726.

Wedepohl, K.H., 1978, Handbook of geochemistry: Berlin, Springer-Verlag, 442 p.

Wise, M.A, Cerny, P., and Falster, A.U, 1998, Scandium substitution in columbite-group minerals and ixiolite: The Canadian Mineralogist, v. 36, p. 673-680.

Williams, P.J., Barton, M.D., Johnson, D.A., Fontboté, L., de Haller, A., Mark, G., Oliver, N.H.S, and Marschik, R., 2005, Iron oxide copper-gold deposits: Geology, space-time distribution, and possible modes of origin: Economic Geology, 100th anniversary volume, p. 371-405.

Zheng, Y.-F. and Simon, K., 1991, Oxygen isotope fractionation in hematite and magnetite: A theoretical calculation and application to geothermometry of metamorphic iron-formation: European Journal of Mineralogy, v. 3, p. 877-886.

Zheng, Y.F., 1993, Calculation of oxygen isotope fractionation in hydroxyl-bearing silicates: Earth and Planetary Science Letters, v. 120, p. 247-263.